Large Scale Nano- and Micro-Structuring of Polymer Film by Roll to Roll Hot Embossing

Zur Erlangung des akademischen Grades eines
DOKTORS DER INGENIEURWISSENSCHAFTEN (Dr.-Ing.)

M.Sc. Patrick Weiser

von der KIT-Fakultät für Maschinenbau des
Karlsruher Instituts für Technologie (KIT)
genehmigte
DISSERTATION

Hauptreferent: apl. Prof. Dr. Hendrik Hölscher
Korreferent: Prof. Dr. Martin Dienwiebel
Datum der mündlichen Prüfung: 05.12.2024

Karlsruher Institut für Technologie
Institut für Mikrostrukturtechnik
H.-v.-Helmholtz Platz 1
76344 Eggenstein-Leopoldshafen

Eidesstattliche Versicherung gemäß § 13 Absatz 2 Satz 2 Ziffer 3 der Promotionsordnung des Karlsruher Instituts für Technologie (KIT) für die KIT-Fakultät für Maschinenbau:

1. Bei der eingereichten Dissertation zu dem Thema "Large Scale Nano- and Micro-Structuring of Polymer Film by Roll to Roll Hot Embossing" handelt es sich um meine eigenständig erbrachte Leistung.

2. Ich habe nur die angegebenen Quellen und Hilfsmittel benutzt und mich keiner unzulässigen Hilfe Dritter bedient. Insbesondere habe ich wörtlich oder sinngemäß aus anderen Werken übernommene Inhalte als solche kenntlich gemacht.

3. Die Arbeit oder Teile davon habe ich bislang nicht an einer Hochschule des In- oder Auslands als Bestandteil einer Prüfungs- oder Qualifikationsleistung vorgelegt.

4. Die Richtigkeit der vorstehenden Erklärungen bestätige ich.

5. Die Bedeutung der eidesstattlichen Versicherung und die strafrechtlichen Folgen einer unrichtigen oder unvollständigen eidesstattlichen Versicherung sind mir bekannt.

Ich versichere an Eides statt, dass ich nach bestem Wissen die reine Wahrheit erklärt und nichts verschwiegen habe.

Karlsruhe, 05.12.2024 ....

Patrick Weiser

Abstract

Man made climate change is one of the most important challenges that humanity is facing at the moment. One part of the solution to this pressing issue are photovoltaics. While solar power has become relatively cheap in recent years, the problem of efficiency loss by the gradual deposition of dirt, so-called soiling, remains. This problem can be mitigated using various techniques, most of which require water - a scarce resource in the arid climates of the worlds deserts, where large scale photovoltaics work most efficiently. Therefore a simple but effective method of cleaning, that does not require water would be ideal. To find such a method, a look in nature might prove very helpful. Through the course of evolution nature had to overcome great challenges and invent ingenious solutions to many complex problems. Notably the surfaces of biological species are an area of great interest, as these surfaces are the interface between the living organism and its environment. Therefore it must fulfill a wide range of functions, many of which take place at the micro- and nanoscale. Replicating the biological microstructures is by itself not a trivial task. The large-scale production of microstructured, biomimetic surfaces, e.g., for the use on solar panels, is still a large challenge, as many of the technologies used to fabricate microstructures are limited to the size of commercially available wafers. The key question of this thesis is therefore: can microstructured biomimetic surfaces be produced large scales? Special focus is given to the structuring of polymer film, which is used in all areas of everyday products from simple packaging over medical applications to aerospace applications. The large-scale structuring of polymer film with biomimetic structures appears particularly promising, as the enormous variety of polymers and their properties could enable the use of biomimetic surfaces in many diverse areas and applications. The polymer films are processed using a continuous roll-to-roll (R2R) hot embossing process, which enables the microstructuring of large areas at high throughput. At the beginning of the thesis, a process for the large-scale production of so-called nanofur is presented. Its surface imitates the hairy surface of the floating fern *Salvinia molesta* and is characterized by extreme hydrophobicity and oleophilicity, which leads to self-cleaning properties comparable to that of the Lotus plant. The advantages of nanofur include that it can be produced without complex molds. This approach enables the study of the fundamental feasibility of biomimetic surfaces produced by R2R hot embossing. In the next step, the process is further developed in order to produce arbitrary surface structures. This involves combining film extrusion with R2R hot embossing. Finally this process is used to produce biomimetic surfaces, which are inspired by the skin of sandfish (*Scincus scincus*). This surface is designed to enable dry

i

self-cleaning of solar panels. After examining and optimizing the geometry of the sandfish structures corresponding molds are produced and the sandfish structures are fabricated using R2R hot embossing. Lastly they are subjected to a field test on solar panels in order to prove their usefulness.

Kurzfassung

Der menschengemachte Klimawandel ist die wohl größte Herausforderung der die Menschheit derzeit gegenüber steht. Ein Teil der Lösung dieses Problems werden Photovoltaikanlagen sein. Zwar wurden die Anlagen in den letzten Jahren immer günstiger; das Problem des sog. Soiling - die allmähliche Ablagerung von Staub und der damit einhergehende Effizienzverlust - besteht nach wie vor. Es existieren verschiedene Reinigungstechniken, von denen die meisten allerdings Wasser benötigen. Wasser, welches in den Wüstengebieten, wo Solarpanele sinnvollerweise aufgestellt werden, eine knappe Ressource ist. Eine Methode der Solarpanel-Reinigung, welche kein Wasser verwendet, wäre daher ideal. Um eine solche Lösung zu finden, lohnt unter Umständen der Blick in die Natur. Im Laufe der Evolution musste die Natur zahlreiche große Herausforderungen meistern und intelligente Lösungen für komplexe Probleme finden. Interessant sind insbesondere die Oberflächen von biologischen Proben, da die Oberfläche als Grenze zwischen dem Organismus und seiner Umwelt zahlreiche Funktionen übernehmen muss. Viele dieser Funktionen spielen sich auf der Mikro- und Nanoebene ab. Die künstliche Replikation von biologischen Oberflächen alleine ist eine Herausforderung. Die großflächige Herstellung von mikrostrukturierten, bionischen Oberflächen eine noch größere Herausforderung, da viele der Techniken, die zur Herstellung der Mikrostrukturen verwendet werden, auf die Größe von handelsüblichen Wafern beschränkt sind. Die Leitfrage dieser Arbeit lautet daher: Können mikrostrukturierte, bionische Oberflächen auf großer Fläche hergestellt werden? Besonderer Fokus liegt dabei auf der Strukturierung von Polymerfolien, welche sich großer Beliebtheit in allen Bereichen des Alltags, von einfachen Verpackungen über Medizinprodukte bis hin zur Raumfahrt erfreuen. Die großflächige Strukturierung derartiger Folien mit bionischen Strukturen erscheint besonders vielversprechend, da die enorme Vielfalt von Polymeren und deren Eigeschaften einen Einsatz bionischer Oberflächen in zahlreichen Bereichen und Anwendungen ermöglichen könnte. Die Verarbeitung der Polymerfolien findet mittels einem kontinuierlichen Rolle zu Rolle (R2R) Heißpräge-Verfahren statt, welches die Mikrostrukturierung großer Flächen bei hohem Durchsatz ermöglicht. Zu Beginn der Thesis wird ein Prozess zur großflächigen Herstellung von sogenanntem Nanopelz vorgestellt. Seine Oberfläche imitiert die haarige Oberfläche des Schwimmfarns *Salvinia molesta* und zeichnet sich durch extreme Hydrophobie sowie Oleophilie aus. Dies führt zu selbstreinigenden Eigenschaften, ähnlich der bekannten Lotus-Pflanze. Zu den Vorteilen des Nanopelz zählt, dass er ohne komplexe Formeinsätze hergestellt werden kann. Dies ermöglicht die grundsätzliche Machbarkeit von bionischen, durch R2R-Heißprägen hergestellten Oberflächen, zu demonstrieren. Im

nächsten Schritt wird der Prozess weiterentwickelt, um beliebige Oberflächen-Strukturen auf diese Weise herstellen zu können. Dabei wird Folienextrusion mit R2R-Heißprägen kombiniert. Dieser neue Prozess wird dann genutzt, um bionische Oberflächen, welche vom Sandfisch (*Scincus scincus*) inspiriert wurden, herzustellen. Diese Oberfläche soll eine trockene Selbstreingug von Solarpanelen ermöglichen. Nachdem die Geometrie der Sandfisch-Oberfläche untersucht und optimiert sowie eine entsprechende Form hergestellt wurde, werden Sandfisch-Oberflächen mittels R2R-Heißprägen hergestellt und einem Feldversuch auf Solarpanelen unterzogen.

Contents

List of Figures

List of Tables

List of Abbreviations

ABS Acrylonitrile butadiene styrene. 56

AFM Atomic force microscopy. 18, 19, 72, 76, 87, 88, 99, 100

COC Cyclic olefin copolymer. 12, 13, 29, 31, 57, 58

CSM Confocal scanning microscopy. 19, 57, 71

IMT Karlsruher Institute of Technology - Institute of Microstructure Technology. 14, 28, 81, 103, 107

LDPE Low density polyethylene. 17

P2P Plate to plate. 4, 5, 14, 15, 26, 29, 45, 46

PC Polycarbonate. 27–29, 33, 35, 57

PDMS Polydimethylsiloxan. 10, 13, 54–57, 79

PE Polyethylene. 27, 33, 35

PEEK Polyether ether ketone. 53

PLA Polylactic acid. 27, 33, 35

PMMA Polymethylmethacrylate. 12, 53–58, 101, 102, 104

PP Polypropylene. 10, 12, 27–31, 33–36, 41, 57

PTFE Polytetrafluoroethylene. 67, 69

R2P Roller to plate. 5, 46

R2R Roll to roll. i, iii, 5, 15, 28, 29, 32, 36, 37, 45–47

SEM Scanning electron microscopy. 26, 31

SPI Serial Peripheral Interface. 101

VSI Vertical scanning interferometry. 19, 20

Chapter 1

Introduction

Man made climate change is probably one of the most important challenges that humanity is facing at the moment [1]. The emissions that cause this climate change in the first place are typically divided into the following sectors: energy, transport, buildings, industry, agriculture and forestry as well as waste management [1]. The emissions of the energy sector make up a large part of the total global greenhouse gasses emitted [2, 3]. It is furthermore the most important of these sectors as many of the emissions caused by the other sectors can be eliminated if enough cheap, green energy could be produced. Solar power is together with wind and hydro power one of the three large contributors to global renewable energy production [4]. Furthermore the installed solar power is predicted to double by as early as 2027 [4]. Since the mid 2010s the cost of solar power is competitive with fossil fuels and further reductions in costs by 40 to 50 % are predicted [1, 5]. All of this makes solar power one of the promising technologies for future clean energy production.

However, contamination of photovoltaic panels by dust and dirt, so-called soiling, is a huge issue in the operation of large solar farms [6]. Photovoltaics are, for obvious reasons, particularly well suited for regions with high solar radiation, and preferably only few cloudy and rainy days throughout the year. Naturally regions like this, e.g. the Atacama desert, are very arid and therefore lots of dust can accumulate on the panels. Given that the accumulated average yearly rainfall in the Atacama desert ranges from near zero to just about 160 mm/a, depending on the exact location, and given a predicted reduction in rainfall due to climate change [7, 8], natural rain is not enough to keep the photovoltaic panels clean. Since soiling can cause losses of up to 80 % of the total solar power [9], the panels have to be cleaned frequently. Manual as well as (semi-) automated cleaning solutions do exist, however, these have some disadvantages or are somewhat cumbersome and costly, as outlined in the next section.

1.1 State of the Art

This part of the introduction gives a brief overview of the state of the art in the relevant fields of research of this work. These include cleaning of solar panels, biomimetics, hot embossing and the special case of large scale structuring using biomimetic surfaces.

1.1.1 Cleaning of Photovoltaic Panels

Manual cleaning is the most obvious answer to soiling of solar panels, but it requires trained personnel and is therefore costly. Additionally, cleaning must be carried out regularly in order to have an effect at all, further driving up costs [10, 11]. Rain can clean solar panels and nearly restore their original power output [12], but some regions of the world do not encounter enough and frequent rain to rely on just that as a cleaning method. The logical next step are water spraying systems which are a convenient solution but also require a lot of water [10, 12, 13] which is considered a scarce resource in these regions [7, 8]. There is a number of (semi-) automated cleaning robots, some attached to vehicles, some running on tracks along the solar panels, that use a combination of brushes and water in order to clean the panels. While efficient when moving along a row of solar panels, traversing from one row to the next in a fully automated way is challenging. Since most robotic cleaning solutions require a tether providing power and water, they usually still require frequent human interaction [10, 13]. A promising idea is the use of electric fields to clean solar panels. Transparent electrodes are placed in a thin, non conductive polymer film that is laminated on top of the solar panel. An AC signal is applied to the electrodes and the resulting electrical field will move particles off the surface [10, 14, 15]. While very elegant, this solution seems to be still in the research state and the fine electrodes that are required would drive costs of the solar panels up. Furthermore the voltages applied to the panels are on the order of multiple kV which might pose an additional hazard. Therefore none of these aforementioned solutions seems to be ideal.

1.1.2 Biomimetics

When looking for solutions for the soiling problems of solar panels it might make sense to take a look in nature. Through the course of evolution, animals and plants constantly faced vast challenges and devised ingenious solutions to a great variety of problems. Humans have therefore often sought inspiration in nature for solutions to technical challenges. Well known examples for this field of study called biomimetics are Velcro fasteners, that were inspired by burrs attaching to a dogs fur [16, 17, 18] or so-called "Gecko tapes" - a type of scotch tape that uses structure instead of glue to create adhesion. Other examples include the Shinkansen train, the front of which was modeled after the beak of the Kingfisher bird (*Alcedinidae*) [19], the ACO algorithm that is often used to tackle the "traveling salesman problem" which was modeled after the behaviour of ant colonies [20] as well as drag reducing surfaces used on airplanes that were inspired by shark skin [21, 22]. One could even argue that the airplane itself is - to some extent - a biomimetic invention mimicking the flight of birds. One of the most famous examples of biomimetics is probably the Lotus effect. The Lotus plant (*Nelumbo nucifera*) uses a combination of surface structure and epicuticular wax to create extreme hydrophobicity of its leafs [23]. Water on the plants surface forms almost spherical droplets that roll off the surface easily without leaving a trace. Since the interface area between the water droplet and a dirt particle on the leaf is much higher than the contact area between the dirt particle and the plants surface,

adhesion forces between water and dirt particles are larger than the adhesion force between the dirt particle and the leaf. Hence dirt particles adhere to the water droplet and are being carried off the leaf as the droplet rolls over them. This self cleaning effect has long fascinated researchers and has been mimicked with various techniques and therefore found its way into several commercial applications, e.g., in paints for houses with self-cleaning facades, textiles that repel unwanted dirt or hydrophobic coatings for glass surfaces such as windows and windshields [23, 24, 25, 26].

The so-called "nanofur", developed at KIT, is a biomimetic surface that uses an effect similar to the Lotus effect. It is inspired by the *Salvinia molesta* water plant, that has its leaves covered in lots of tiny hairs, that firstly make the surface superhydrophobic. Secondly, the hairs enable the plant to retain a layer of air when pushed underwater [27], which makes this kind of surface interesting for drag reduction in, for example, ships [28]. It was furthermore discovered that this surface is not only hydrophobic but also oleophilic. It can therefore be used to separate oil from water [29]. Details on the function and the preparation of nanofur will be discussed in Chapter 3 of this work.

While it seems beneficial for most plants to have dry leafs, as water on the surface, for example, impedes the uptake of CO_2, not all plant surfaces are hydrophobic. For example pitcher plants (*Nepenthes*) have specialized leafs that are used to trap insects. The surface of these leafs is superhydrophilic with contact angles well below 10°. Even the moisture from fog or condensation results in a thin water film on the surface of the leaf, making it extremely slippery to insects, which hence fall into the pitcher-like leaf where thy are digested [30]. Based on this principle, so-called slippery lubricant infused porous surfaces (SLIPS) have been developed using various fabrication approaches. These kinds of surfaces can be used, e.g., as marine anti-fouling or as anti-icing solutions [31, 32, 33]. Also SLIPS can be used as self-cleaning surfaces, especially if the contaminants are high viscosity, low surface energy fluids [33]. The smooth surface structure on the leafs of *Anubias barteri* lead to contact angles approaching zero. Therefore even small quantities of water spread over the whole surface of the leaf, dissolving contaminants and carrying them off. The minuscule contact angle of the water can also lead to the water working like a knife scarping larger dirt particles off the surface [34]. While most work regarding artificial self-cleaning surfaces has focused on hydrophobic surfaces, some researchers have also mimicked superhydrophilic surfaces in order to develop self-cleaning coatings for solar panels [35]. This has also been combined with TiO_2 coatings that can decompose organic contaminants by photocatalytic oxidation [36]. In summary both, superhydrophobic and superhydrophilic surfaces, can have self-cleaning properties; the selection for one or the other approach has to be done in regards to several parameters such as the application envisioned or the nature of the contaminants.

These are only a few examples of biomimetics, a myriad of other interesting applications of biomimetics have been reported. These include examples of superhydrophobicity and hydropilicity, self-cleaning, drag reduction, lift generation, adhesion, thermal insulation, anti-reflection or structural coloration and many more [37, 38, 39, 40]. A key difference between samples found in nature and "engineered" solutions is the use of basic building

materials in nature. Man uses combinations of many different materials and top-down manufacturing to achieve a given function, whereas nature typically uses the same basic materials to achieve wildly different functions. Hair, nails and claws, horns, hooves, reptilian scales and wool all fulfill wildly different functions, yet they are all composed of keratin. Chitin is the main material for the exoskeletons of many insects and spiders, but is also the material that makes up the honeybees hair or the eyes of some arthropods [41, 42]. Nature uses these basic materials as well as routine, bottom up fabrication techniques to provide function by capitalizing on hierarchical structures [40, 41]. The structures found in nature are therefore often very complex and difficult to manufacture artificially. They are often characterized by high aspect ratios and a hierarchical organization that can span multiple magnitudes of scale. The rise of micro- and nanotechnology since the 1990s has driven forward the use of principles and techniques found in nature, yet there is an seemingly endless, still untapped potential for future biomimetic applications and solutions for our modern day challenges [40, 43].

A possible biomimetic solution for the cleaning of solar panels is inspired by the sandfish (*Scincus scincus*), a small lizard living in the deserts of northern Africa from the Sahara to the Arabic peninsula [44]. It has become famous for its ability to move through and underneath the sand covering most of its habitat very quickly. Its scales are covered in nano-steps. Previous studies revealed that these structures cause an anisotropic friction coefficient [45, 46]. It was further shown that by exciting a surface like this with a small vibration, dirt particles on the surface can be moved in the distinct direction of the lower friction coefficient. This effect can be used to clean solar panels by moving dirt off the edges of the solar panels. This solution would provide some benefits. Firstly, this solution does not use any water and is therefore particularly suited to arid regions of the world. Secondly, it can be fully automated and does not require any human interaction. Thirdly, the cleaning can happen multiple times per day, preventing the buildup of larger quantities of dust that would be hard to clean. While the biological sample has been investigated and the transport of particles by this mechanism was demonstrated in previous studies [47, 46, 45], no attempts are known of producing artificial surfaces that have the properties of sandfish scales. Only little is known about the influence of the geometry of the structures and the vibration parameters on the effectiveness of particle transport.

1.1.3 Roller Hot Embossing

Placing sandfish-inspired nanostructures on the enormous area that a solar farm uses is not a trivial task, given that most tools used in micro and nanofabrication are very costly and, more crucially, optimized for wafer size substrates. Most lab equipment works with 150 mm wafers while industrial equipment can typically process wafers of 350 - 400 mm in diameter [48], which is not even close to the many square kilometers needed to cover entire solar farms. This is where micro-replication techniques such as hot embossing can be used. In traditional plate to plate (P2P) hot embossing a metal mold, e.g., made from nickel, has to be fabricated once, using all of the different tools of microstructure fabrication. This mold can then be used many times to imprint micro- and even nanostructures in

thermoplastic polymers, greatly reducing the cost of an individual part. While this solves the cost problem for individual, small parts, the technology is still only able to structure a relatively small area and is still a batch wise process with relatively long cycle times. Therefore many attempts to transform this traditional plate-to-plate (P2P) hot embossing to a continuous roll-to-roll (R2R) process have been undertaken in recent years [49]. A roll-to-roll process would eliminate the size problem entirely and furthermore increase the cost effectiveness of hot embossing. This would facilitate the use of biomimetic, microstructured surfaces in areas where large quantities of material would need to be structured such as solar power as well as many other areas (packaging, construction, etc.).

Roller to plate (R2P) embossing uses a structured and heated roller that is moved over a stationary temperature controlled counter-plate. The roller is pressed into the polymer, melts it on contact and imprints its structure into the polymer film. While certainly able to structure larger areas than classic P2P hot embossing and arguably quite cost efficient [50], this technique has some drawbacks. It is still a batch wise process which limits productivity. Furthermore, just as in traditional P2P embossing producing very thin film can be challenging and might require a sacrificial layer. Lastly the heating, melting and flowing of the polymer all has to occur in the short time that the - idealized - contact line of the roller is actually touching a given position of the film. An improvement in terms of productivity are continuous roll to roll (R2R) processes. In general, two counter-rotating rollers that feed polymer film or sheets between them are used. One or both rollers are structured and heated well above the melting temperature of the polymer. On contact the polymer film (partly) melts and the microstructures on the surface of the rollers are imprinted into the film. This process has the same drawback as R2P embossing as all the melting and flowing of the polymer has to occur in a very small time window as the contact between mold (roller) and polymer film is essentially a line. This makes processes like this very sensitive to variations of the roller speed [51]. Furthermore, induced mechanical stress as well as incomplete filling of the mold cavities can occur [52]. During demolding, the newly imprinted microstructures are still hot and therefore soft which can reduce the quality of the imprints or even destroy the structures. Thermal reflow of the polymer, due to the absence of a cooling step in R2R embossing, can further reduce structure height. Several approaches addressing this absence of active cooling in R2R embossing have been developed, most of them use some kind of long conveying mold that is guided along the polymer film as it is passed through the machine. Due to the long contact time it is possible to cool the initially hot mold down while it is in contact with the polymer film, resulting in much lower demolding temperatures. Unfortunately, these approaches require very long molds, in the order of meters. Fabricating these very long molds with the most intricate structures, must be considered challenging. Another method of R2R hot embossing are so-called hybrid R2R embossing processes, where an extrusion line is placed in front of the structuring rollers, which will cool the molten polymer instead of heating it [49]. While this solves some of the problems of R2R embossing, only little work has been done using this approach so far. In general film extrusion, even with flat, unstructured film, is a delicate process that requires precise control of process parameters

and is sensitive to parameter variations [51]. Roller UV-imprinting is another approach for fabricating large scale microstructured surfaces, however, due to the very nature of the process, it is restricted to UV-curable resists. These are, when compared to traditional thermoplastics, more costly by a factor of 30 to over 100 (prices as of 06/2024).

1.1.4 Large Scale Structuring of Biomimetic Surfaces

The special case of combining large scale (R2R) structuring with biomimetic surfaces has been attempted by few other groups, using different techniques. For example a process for fabricating so-called biomimetic SLIPS (slippery lubricant infused porous surfaces) on a large area via a UV-roller imprinting process has been reported [53]. Another UV-based approach was used to replicate shark skin as drag reducing measure. Here, a transparent, belt-like mold was obtained directly from shark skin and used to structure a UV-curing paint directly on large free-form surfaces such as a ship's hull [54]. As mentioned above, the restriction to UV-curable materials means that UV imprint is impractical for some applications. Direct laser interference patterning (DLIP) has been used to fabricate shark skin structures for anti-icing, Lotus-effect surfaces or moth eye structures, even directly in metals and on a relatively large area [55, 56]. That makes DLIP an interesting tool in mold fabrication for roller imprinting. However, the minimum feature size that can be manufactured in this way is about 500 nm [55], which is too large for some biomimetic structures. When done in metals the surface roughness can be high [57]. Furthermore for structuring the surfaces of thousands of square meters of solar panels directly, this technique seems quite costly. Another roller based process has been used to produce structurally coloured cellulose nanocrystal films for decorative purposes [58] on a large scale. Here the structure was not produced by the roller itself, but rather the roller was used to apply a solution of cellulose nanocrystals onto a carrier film and the structures formed by self assembly of the cellulose nanocrystals while the solvent was evaporating. None of this research attempted to use roller hot embossing to produce large scale biomimetic surfaces.

1.2 Aims of this Work

The aim of this work was to develop a process for structuring large quantities of polymer film with biomimetic structures in a continuous roll-to-roll hot embossing process. This process will then be used to imprint artificial, sandfish-inspired surfaces in order to study their potential in mitigating soiling of photovoltaic panels. One of the challenges with roll-to-roll hot embossing is the production of a sufficiently large mold [59]. The so-called nanofur, which was introduced briefly in the previous section, can be produced by a modified hot embossing process called hot pulling with just a sandblasted steel plate serving as a mold [60]. Mold fabrication can therefore be skipped for producing nanofur, which makes it a good starting point in the development of the R2R process. The batch-wise process used to produce nanofur was transformed into a roll-to-roll process for thick polymer sheets and then further optimized by the use of a coextruded support layer to produce

thin polymer film covered in nanofur. This process, however, is limited to the production of nanofur. Other microstructures can unfortunately not be manufactured in this way.

After demonstrating that roll-to-roll hot embossing is feasible for nanofur, the roll-to-roll process was further adapted in order to enable imprinting of arbitrary microstructures. To do so, classic film extrusion was combined with roller hot embossing in a single step, creating a productive and accurate replication technique that enables the structuring of many square meters of polymer film in a short amount of time. This is different to the approaches that other groups have pursued, which mostly aimed to structure already extruded sheets or films rather than structuring the polymer right after extrusion [49]. The approach of my study provides some benefits that will be further outlined in Chapter 4. Since a machine for this process did not readily exist, the available machinery had to be excessively modified and solutions to problems such as mold attachment, cooling, or increased embossing forces had to be devised. A set of test structures was manufactured and imprinted to optimize process parameters and learn about the influence of various parameter combinations on structure quality. After developing this direct roller imprinting process, it was used to imprint the biomimetic structures inspired by the sandfish.

As outlined in the previous section, this sandfish inspired surface can help mitigating soiling problems of solar panels by providing an anisotropic friction coefficient. While the basic effect of sandfish inspired microstructures was shown in previous studies, it was not well understood, which of the geometric parameters of the microstructures exactly influence the motion of the dust particles on the surface. Furthermore, the parameters of the vibration had not been varied in earlier studies [46, 45, 47]. In order to analyze the behaviour of different-sized sand particles on a set of artificial sandfish-inspired surfaces a custom, piezo driven vibration stage and a camera-based particle tracking system were developed. Since no commercial solutions that fit the needs of these experiments existed, the whole setup and software had to be developed from the ground up. This system enabled precise analysis of the movement of particles on the surface precisely and calculate the speed, direction, residual particles as well as a number of additional parameters. Thus it enabled the quantitative measurement and comparison of the influence of geometry and vibration parameters on particle motion.

After the influence of geometry and vibration of dust particles on sandfish-inspired surfaces was understood, such surfaces were prepared using the R2R imprinting process. To be able to imprint the structures, a mold had to be fabricated first. This was done by stitching individual pieces to form a sufficiently large mold. This stitching was done by producing many identical polymer replicas of a small piece of the artificial sandfish structure by hot embossing and UV-imprint. The individual pieces were cut and milled to the same height. In a manual process described in detail in Chapter 4, the pieces were stitched and the small gaps in between the parts were filled with a polymeric solution. Afterwards an electroplating step was produced in order to obtain a durable metal mold, which was used for roller hot embossing. While this new method of stitching is surely not the most precise option for stitching individual parts to form a larger mold, it uses minimal tools that are available in some form to almost every researcher and achieves remarkably

good results, considering the simplicity of the process.

With the mold prepared in this way, large area sandfish-inspired surfaces were produced by roller imprinting. The resulting structured polymer film was then laminated onto solar panels. The panels were placed outdoors for two months on a small test rig, that logged the solar power as well as additional environmental parameters such as temperature, humidity and illumination. The microelectronics and sensors used for this "sensor box" are comparatively cheap, so that boxes like this can be reproduced anywhere in the world in order to analyze the effectiveness of sandfish inspired solar coatings in different climates all over the world. Since the climate in southern Germany, where these experiments were conducted, is not comparable to the climate in the deserts, another box was placed in a lab simulating extremely dry and dusty conditions to verify whether sandfish coatings can provide any benefit in climates like this.

1.3 Structure of this Thesis

This thesis is organized as follows: firstly a short review of the methods and techniques used can be found in Chapter 2. Then I will present my own work, which was kindly supported by bachelor and master students and colleagues, in the following chapters. Chapter 3 covers the development of the nanofur production process as well as the fabrication process for an exemplary product made from nanofur polymer film. Chapter 4 encompasses the development of the roll-to-roll structuring process for producing geometrically defined microstructures. This includes mold preparation and fixturing as well as the necessary modifications to machinery and the actual process optimization. Chapter 5 focuses on the sandfish inspired surfaces, including the development of tools for the analysis of particle motion, the results of the according experiments as well as the results from the field tests of the coatings for solar panels. Finally, I will conclude my studies in Chapter 6 and provide a short outlook for future research. Each chapter provides a more detailed introduction into the respective topic as well as a section outlining the fundamentals of the respective chapter.

All in all, this study answers the following three research questions in Chapters 3, 4, and 5.

1. Is roll-to-roll hot embossing useful for large scale production of biomimetic surfaces?

2. Can a combined extrusion and embossing roll-to-roll process yield precise microstructures and improve upon existing roller embossing processes?

3. Can this process be used to imprint large scale sandfish inspired surfaces and, if so, do these surfaces provide real world benefits to the solar industry?

Chapter 2

Methods and Materials

This chapter gives an overview over the fundamental methods and materials utilized in this work. First a selection of the most important polymers and the methods used to process them is introduced, then the measurement tools and machines employed to inspect the fabricated samples are presented.

2.1 Materials and Processes

This section describes a selection of the most important materials (polymers) used in this study and their respective properties. Furthermore, the fundamentals of the processes used to handle, treat and process those materials are presented. Lastly, the process of electroforming, which was used to fabricate molds, is introduced briefly.

2.1.1 Fundamentals of the Utilized Polymers

Polymers are one of the four fundamental material classes defined in material science [61]. While a great variety of different natural (e.g. DNA, natural rubber) and synthetic polymers (e.g. PP, PE, PC) exist, the work presented in this thesis will focus on the synthetic, technical polymers widely known as plastics. Hundreds of different technical polymers are known, all with specific properties and characteristics [61, 62]. This variety makes polymers extremely versatile and contributed to their widespread use. Other advantageous properties are their relatively low weight, high toughness, durability and low cost as well as a large selection of processes that can be used to shape polymers [62]. These characteristics make polymers the ideal material for an endless amount of different applications ranging from single use packaging over construction and medical applications to commodity goods, household items or even high tech products such as computers or solar panels. This variety of applications, combined with their numerous advantageous properties and extremely widespread use, led us to choose polymers as a base material for large scale micro-structuring.

Polymers in general consist of long backbone chains of covalently linked atoms, often carbon, but other elements such as N, O, or Si can also be part of this chain. Attached to

this backbone chain are side groups or chains of which a single hydrogen atom would be the most simple form. Alcohol (-OH) or methyl groups (-CH$_3$) are other widespread possibilities [63, 64]. This versatile basic structure explains the enormous number of types of polymers; all of which feature unique properties. Polymers are usually divided in three groups; thermosetting, elastomeric and thermoplastic based on the link structure in between individual polymer chains. Thermosetting polymers feature dense cross links between polymer chains leading to excellent mechanical properties. Heating of thermosetting polymers will ultimately lead to degradation instead of softening and flowing of the polymer. Parts made from these types of polymer are fixed in shape when they are produced, usually by polymerization of monomers, and cannot be heated in order to change their shape later on. They are usually used at temperatures below their glass transition temperature (T$_G$, see next paragraph). Elastomers in contrast are typically used well above their T$_G$. They can be stretched by a great amount and return to their original shape once the force stretching them subsides. They feature cross links between the polymer chains but far fewer than the hard thermosetting polymers. This loose network of cross links gives the elastomers their great flexibility, while at the same time preventing the molecular chains from sliding past each other irreversibly. Elastomers are frequently included in the group of thermosetting polymers as their shape is also set when producing the polymer and cannot be changed by heating later on. In contrast, thermoplastic polymers consist of long polymer chains that are not cross linked and will therefore, when heated sufficiently, soften and eventually "melt", *i.e.*, begin to flow under mechanical stress. Thermoplastics are usually produced in the form of granules and can then be used in a variety of different processes such as injection molding, thermoforming, extrusion, or hot embossing to shape them into a final product [64]. In this thesis all polymers processed are therefore thermoplastics, with the exception of PDMS, which was used for making soft molds.

Thermoplastics can be further divided into amorphous and semicrystalline types. In amorphous polymers the polymer chains are fully disordered, whereas semicrystalline polymers feature regions where multiple polymer chains lay in parallel to each other, forming crystal-like structures. The amount of crystallized parts can be adjusted for many polymer types. For polypropylene, for example, (PP) the crystallinity is usually between 30 % to over 60 % for some types [65]. This variation in crystallinity leads to different physical properties: semicrystalline polymers, for example, often have a whiteish appearance while amorphous polymers can be completely transparent. Another example is the temperature dependency of the shear modulus. At low temperatures the polymers are in the glass state where the polymers are relatively brittle, show energy-elastic behaviour and have a high shear modulus. In the so-called glass transition range the polymers transition from glass like behaviour to rubber-elastic behaviour. The shear modulus of an amorphous polymer drops significantly whereas the semicrystalline polymer only shows a weak glass transition, *i.e.*, the shear modulus does not change as much as it does in a amorphous polymer. This can be explained by a softening of the amorphous parts, while the crystalline parts are not affected [66]. Although this process continues over a temperature range, manufacturers often quote a glass transition temperature (T$_G$) for their products. However, since mul-

tiple methods to determine and define the glass transition temperature exist, these values should rather be taken as an indication in which temperature range the glass transition occurs [67].
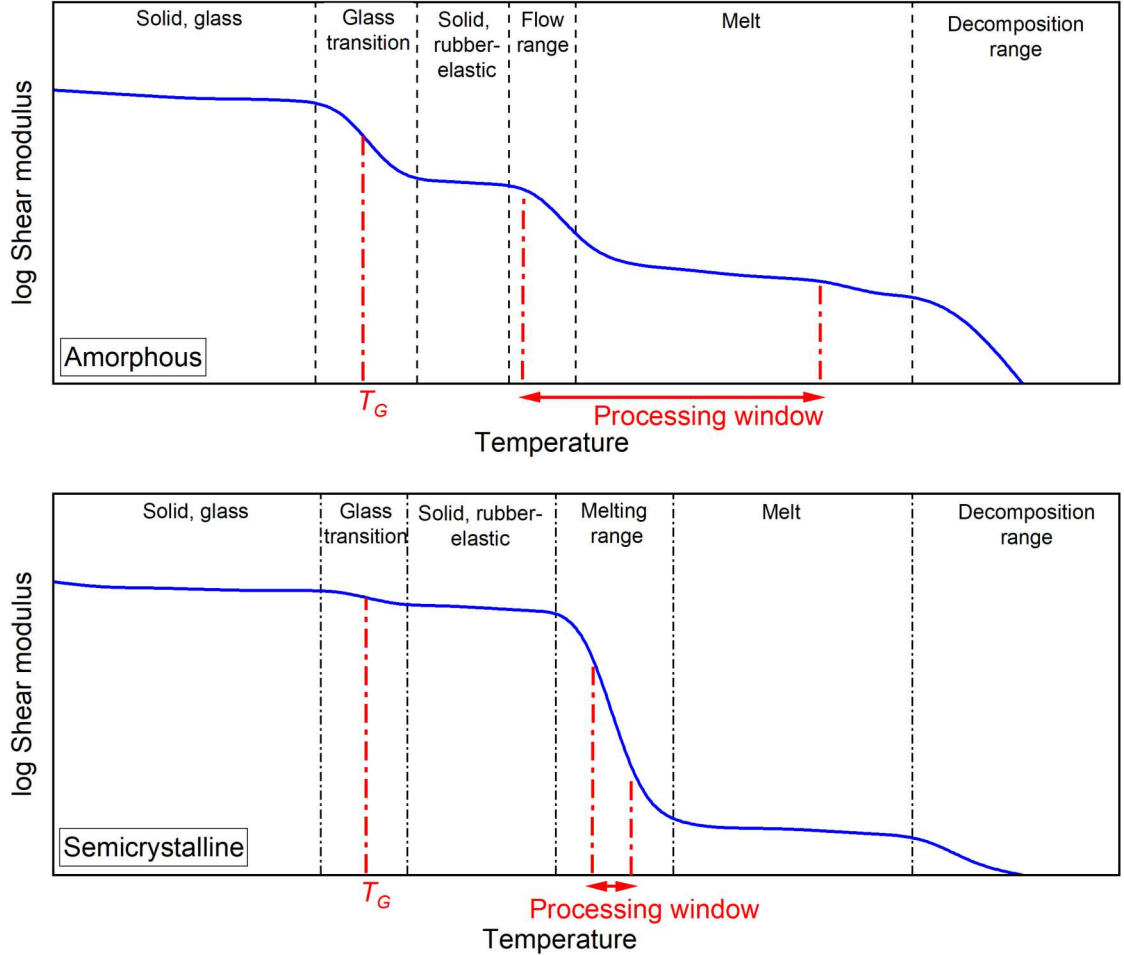
Figure 2.1: Schematic plots showing the shear modulus for amorphous and semicrystalline polymers against temperature. The typical processing window is much wider for amorphous thermoplastics. Image reproduced on the basis of Fig. 3.22 and 3.23 in Ref. [66].

When heated further, the amorphous polymer can begin to flow upon reaching a certain temperature and melt. This thermal behaviour is characterized by a continuous decrease of the shear modulus over a large temperature range. In a strictly scientific sense, amorphous polymers actually cannot melt; the correct term is plasticizing. However, for the sake of convenience, melting is used throughout this thesis, as this is what happens in an engineering sense. Semicrystalline polymers on the other hand show almost no change in shear modulus up to a certain temperature, where a significant drop of the shear modulus occurs. The following molten state is often characterized by a relatively low viscosity [66, 68].

In summary, it can be concluded that amorphous polymers cannot be characterized by a single melting temperature, but rather show a melting range, whereas semicrystalline

polymers can melt within a temperature window of only a few degrees. This behaviour might cause issues when attempting to reach a defined melt viscosity for semicrystalline polymers, as a small change in temperature results in a large change of viscosity. In the following the properties and typical applications of the polymers used in this thesis are summarized.

Cyclic olefin copolymer (COC) is an amorphous polymer with typical applications in packaging, healthcare and optics [69]. COC features excellent optical properties with high transparency in the UV-, visible as well as in the far infrared spectrum. Other features include a high glass transition temperature (> 200°C), high Youngs modulus, low moisture absorption, and good chemical resistance [70]. These properties make it a good polymeric alternative for glass. Unfortunately, COC is not particularly resistant to long term UV exposure [69]. Processing, however, especially by film extrusion,is aided by the high melt flow index of COC. Furthermore low shrinkage and good dimensional stability make COC ideal for micro replication. The type used throughout this thesis was TOPAS COC 8007s-04 (Polyplastics).

Polymethylmethacrylate (PMMA) is an amorphous polymer also known as acrylic glass or by its brand name "Plexiglas". Its high tensile strength, low density and high transparency of 92 % makes it an ideal replacement for glass windows. PMMA is naturally UV stable, which makes it suitable for outdoor or solar applications [71, 72]. Furthermore PMMA is exceptionally well suited to CO_2-lasercutting with smooth and burr free edges of cuts [73]. Two types of semifinished PMMA products are available: cast sheets of PMMA, where a mixture of methyl methacrylate, initiators and additives is polymerized in between smooth glass plates, and extruded (thermoplastic) sheets of PMMA that are produced from granules. In particular, the production of thin film by means of extrusion is challenging. On the other hand, PMMA has favorable processing properties for thermoforming and hot embossing [71]. Unfortunately PMMA can absorb up to 2 % of water, necessitating drying before processing to avoid defects in the final product [74]. UV curing PMMA resins are commercially available, enabling the use of PMMA in UV imprinting or lithography processes. The types used in this thesis were the granule material Diakon CGL 356 (Lucite) and the UV-curing resin Harzspezialisten SK1390 (S u. K Hock GmbH).

Polypropylene (PP) is, after PE and PVC, the third most widely produced technical polymer. It is semicrystalline with a crystallinity of usually around 30 - 60 % [65]. Its hallmark feature is its excellent chemical resistance to almost all organic solvents, bases and many acids. Its glass transition temperature is -20°C, which gives PP a good fatigue resistance. It can furthermore be machined easily and features excellent processability by injection moulding and extrusion. A disadvantage of PP is its higher mold shrinkage, when compared to COC or PMMA. Since it is considered a cheap commodity plastic, typical applications range from household goods (bowls, bottle caps) over automotive applications (fluid reservoirs, bumpers) to packaging (blisters, chemistry bottles) or furniture (stackable

chairs) [65, 75]. In this thesis polypropylene was used to produce so-called nanofur. It was chosen for its wide processing window and its ability to be co-extruded onto COC film. The two polymers adhere strongly but will not mix and can therefore be separated later [76]. The type chosen for these experiments was HP 500N (LyondellBasell).

Polydimethylsiloxan (PDMS)   is an elastomer with a variety of applications. Contrary to many other widely used polymers its backbone chain is not made from carbon but from alternating silicon and oxygen atoms. In its unlinked state it behaves like a viscous liquid and is often used for lubrication. In this state it can flow into tiniest cavities and therefore fill tiny surface structures. This makes it a perfect choice for mold fabrication in micro- and nanotechnology [77]. Its cured, crosslinked form, behaves like a solid rubber and can, due to the low T_G of -125°C, be stretched and compressed in any direction [78]. Its properties can easily be tuned over a wide range. Its shear modulus, for example, can be set anywhere from 100 kPa to 3 MPa [79]. In this thesis PDMS was used to fabricate molds as well as as a flexible rubber element. Furthermore some trials in hot embossing were conducted, where a layer of PDMS served as a separating layer. The type used was Elastosil M4601 (Wacker Chemie AG).

2.1.2   Hot Embossing

Hot embossing is, besides micro injection molding and thermoforming, an established replication technique in micro-systems technology that enables relatively cheap production of microstructured polymer surfaces [66, 80]. A mold, usually made from durable metals, is placed opposite a substrate plate, which is usually sandblasted to increase adhesion during demolding. A polymeric sheet or film is placed between the mold and substrate plate. The hot embossing machine is closed causing both the substrate plate and the mold to contact the polymer sheet. The mold and the substrate plate are heated to the molding temperature of the polymer. This temperature corresponds to the viscosity necessary to build up the required pressure, which implies that amorphous polymers typically provide a relative large processing window, whereas semicrystalline polymers require more precise temperature control, because their viscosity changes significantly in a small temperature gap. In order to achieve the most precise results it is necessary to conduct this process in vacuum; relatively coarse structures might also be replicated under ambient conditions. Once the moulding temperature is reached, tool and substrate move closer to each other at constant speed until the preset maximum embossing force is reached. Now the position of tool and substrate is force controlled. The polymer is cooled, still under constant pressure, until the temperature drops significantly below the melting point of the polymer. Afterwards the part is demolded by slowly opening the machine. Due to the rough surface of the substrate plate, the increased adhesion of the polymer keeps it attached to the substrate enabling even and vertical demolding [66, 52, 51]. If a flat backside of the replicate part is a requirement, then sacrificial layers between the part and the substrate plate might be employed [76].

The hot embossing machine (see Fig. 2.2) is responsible for a precise motion between

the mold and substrate as well as providing the high forces necessary for hot embossing. A massive and rigid frame is a prerequisite to provide the necessary stiffness. The motion system is usually driven by a spindle drive or hydraulics. The machines used at the IMT are derived from tensile testing machines. The heating and cooling system consists of two halves, one mounted on each traverse of the machine. The machines used in this thesis feature a single heating and cooling system for the mold and the substrate and a large combined cooling system. For some of the machines the heating systems are enclosed in a vacuum chamber. The molds themselves are usually made from durable metal alloys such as nickel and fixed to the machine by screws and clamping mechanisms [66, 51, 81]. Mold fabrication can be done by a variety of processes from mechanical machining to lithography and electroforming.
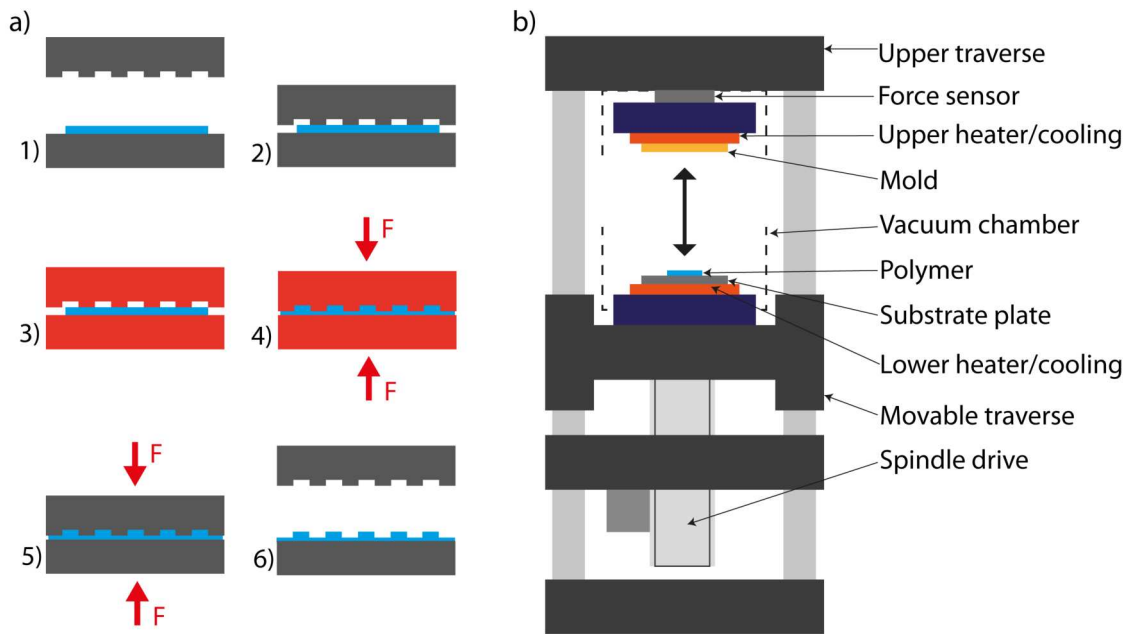
Figure 2.2: a) Basic steps of the hot embossing process. The polymer is heated to the appropriate moulding temperature, then embossed and cooled back down while still under pressure. **b)** Schematic of a hot embossing machine.

In general, hot embossing is considered a very cost effective and flexible process, especially when compared to injection molding. Tooling time is minimal and performing material changes is as simple as placing another kind of polymer in the machine. The short flow paths and slow molding velocities guarantee low residual stress parts [66]. Several variations of this process exist, e.g., the so-called hot pulling process described in Chapter 3. The traditional plate-to-plate (P2P) hot embossing process, however, also entails some drawbacks such as its relatively long cycle times and limitation in structurable area. More details on this topic can be found in Chapter 4.

2.1.3 Roller Embossing

In order to overcome some of the limitations of the P2P hot embossing process, several roller embossing processes (R2R) have been developed [49, 51]. These approaches can be characterized by their continuous nature and use of rollers as mold and substrate. In general, R2R processes provide a much higher throughput of material and show more potential for up-scaling than traditional P2P hot embossing [49]. A detailed introduction into and an overview over these processes is given in Chapter 4.

2.1.4 Extrusion

Extrusion is a continuous process used to produce products with a fixed cross section profile. While used to process a variety of materials, from food items to metals, the term "extrusion" will refer to the extrusion of thermoplastic polymers in this thesis. The extrusion process consists of three basic steps: melting of the polymer, shaping and lastly cooling and solidifying the polymer [82, 83].

Extruders are used to melt the solid polymers, that are usually provided in the form of granules, and to provide polymer melt at appropriate temperature and pressure. While other configurations exist, only single screw extruders were used in this thesis. Figure 2.3a) depicts a typical single screw extruder. It consists of a screw housed in a heated barrel. The screw is driven by a variable speed electric motor, usually through a gearbox to increase torque. At the back end of the barrel a feed inlet leading to a hopper filled with polymer granules is attached. This inlet zone is water cooled to prevent polymer granules from sticking to one another. At the outlet side of the barrel a breaker plate as well as filtering screens are placed leading to an adaptor where various dies can be connected to the extruder. The most important component of an extruder is its screw. While many geometries for extruder screws exist [84], usually the screw can be divided in three sections. The feeding section near the inlet with a constant, deep channel, where the polymer granules are grabbed and transported further into the barrel, a compression section with a decreasing channel depth, where most of the melting and compression of the melt is achieved and a metering section at the end with a shallow but constant channel depth. While the screw can be divided into these sections, its functions occur mostly simultaneously over the whole screw length. The screw grabs the polymer and, through friction forces, will rotate the polymer with it. If there would be no barrel, the polymer mass would just rotate with the screw and would not advance along it. The stationary barrel gives a breaking force to the polymer, causing it to slip slightly on the screw surface. This causes the output rate of an extruder [83, 85, 84]. Commercial screws are highly polished to increase slipping and hardened or coated to avoid wear, while the barrels are grooved in order to increase breaking force and therefore the output rate. The polymer granules are grabbed by the screw and stay loose for the first few revolutions until they eventually become compacted into a solid bed. This "plug" moves along the screw axis rubbing against the hot barrel surface, which melts the polymer resulting in a thin melt film on the barrel. This melt film is intensely sheared by the rotating solid bed and intense

heat is created inside the melt film. Most of the energy required to melt the polymer comes from this mechanical shearing and not from the heating of the barrel. The size of the solid bed decreases along the screw, while the pressure increases greatly in the compression section of the screw. The melt pressure at the tip of the screw can easily exceed 20 MPa necessitating an appropriately designed bearing assembly of the screw on one end and die adaptor on the other.
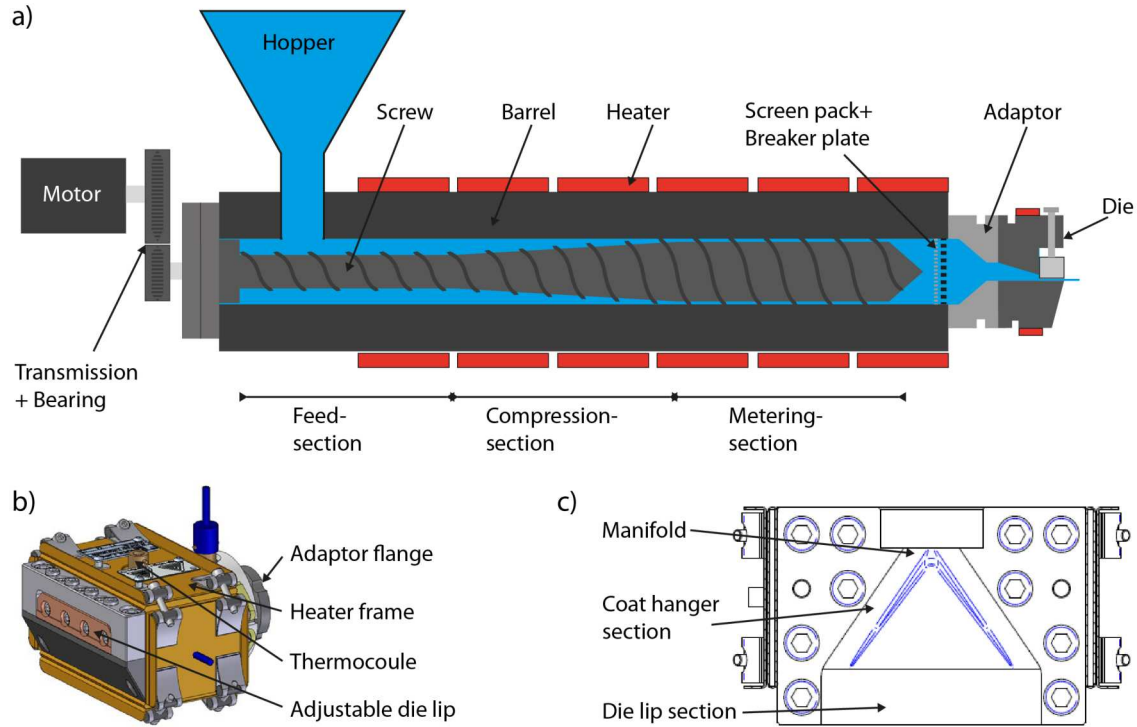
Figure 2.3: a) Schematic of a typical extruder. **b)** The cast film die used in this thesis. **c)** Cut through the cast film die. The coat hanger design is clearly visible. Images b) and c) reproduced from the Collin manual of the cast film die (Collin BSD 120).

Typical commercial extrusion products include polymeric film, sheets, tubing, filament, or profiles. In all cases the polymer is pumped through the adaptor in a rod-like shape by the extruder and it is the task of the die to transform the polymer into the desired shape. While an endless variety of two dimensional profiles for different applications is produced, this thesis focuses on film extrusion, where the die shapes the polymer rod into a thin polymer film. The die design used most often in film extrusion is a coat hanger design, depicted in Fig. 2.3c). It consists of a manifold, coat hanger section, an optional choker bar and a die lip. This die lip is adjustable in order to set the gap, that the polymer is extruded through. Since melt flow through the die is dependant on a multitude of parameters, the die lip can be adjusted on several points along the die width, in order to achieve uniform melt flow and therefore film thickness. The gap size is usually set significantly higher than the target film thickness. The surface of the die lips is highly polished and needs to be kept clean, as any imperfections here will be visible in the extruded film [83].

In profile extrusion the extruded profile is usually cooled by air or water in order to solidify the polymer. In film extrusion this cooling is achieved by cooling rollers (chill rollers) that flatten and smoothen the film finish. Film extrusion is special as, contrary to most other extrusion processes, film thickness is set by a variation of the take up speed, which is kept constant for most other processes. The polymer is stretched, or rather drawn, in the air gap between the die and roller. This gap should be kept very small in order to reduce "neck-in", which refers to the decrease in the polymer films width as it is stretched. This neck-in phenomenon also causes so-called edge bead - a thickening of the edges of the polymer [86, 87]. Furthermore the polymer film should meet the chill roll in a level, straight line to avoid warping and wrinkles in the film [88]. This last step of the film extrusion process - smoothing the film between two rollers - will be adapted to use it to imprint micro- and nanostructures in the polymer film. This development will be outlined in Chapter 4.

The machine available for this thesis is a Collin E20E (Collin Lab and Pilot Solutions GmbH) single screw extruder with a barrel diameter of 25 mm and length of 625 mm. The manufacturer states its maximum throughput at 11 kg/h of low density polyethylene (LDPE). Similar throughput can be expected with the polymers used in this thesis. Attached to this extruder is a heated Collin cast film die BSD 120, with adjustable die lip (0.2-2 mm) and a maximum film width of 120 mm. The film was smoothened by a Collin chill roll CR 72/72/72-200 T, that was significantly modified as described in this thesis in order to enable the fabrication of microstructured polymer film.

2.1.5 Electroplating / -forming

Electroplating is a process that uses electrochemistry to coat substrates with metallic layers [89, 90]. The part to be coated acts as cathode. It must therefore be conductive itself or have a conductive surface layer, which is often applied by physical / chemical vapour deposition. The liquid electrolyte is a solution of a salt of the metal that is to be coated; it thus contains cations of the metal. The anode is a block of that metal or an inert, conductive metal, in the case of an insoluble anode. A voltage from an external power source is applied to the electrodes, which causes current to flow. Cations are reduced at the cathode (the part to be coated) and therefore form a metal layer on the part. In the case of a soluble anode the opposite reaction occurs at the anode, which replenishes the cations in the electrolyte [89, 90]. In this thesis electroplating was used to produce molds for (roller-) hot embossing. A master structure made with various microstructuring technologies is used as a substrate and, after depositing a considerably thick layer of nickel, can be removed either mechanically or etched away chemically. This way delicate and very intricate master structures can be transferred from e.g. brittle silicon wafers to durable nickel molds [80, 91].

2.2 Measurement Techniques and Analysis Tools

This section describes the basics of the measurement techniques used in this thesis. Standard techniques, such as optical microscopy, that are available and known to almost every scientific researcher, are omitted.

2.2.1 Atomic Force Microscopy

Atomic force microscopy is a high resolution type of "tactile" scanning probe microscopy. The achievable resolution is many times better than the Abbe limit that restricts the resolution of optical microscopes. Figure 2.4 shows the basic working principle of an AFM [92]. Basically an AFM scans a small cantilever over the surface of the sample. Its sharp tip (usual tip radii are in the order of a few nm) contacts the surface bending the cantilever. This bending is recorded by a laser pointed onto the cantilever and a photo diode that measures the reflection of the laser light. The bending alters the location of the reflected light on the four quadrant photo-diode. The height of the cantilever is then adapted by piezo elements until the laser spot is again centered on the photo diode. This height adjustment is then recorded as a measurement signal [92, 93]. Usually the cantilever is scanned over each line twice, sampling each line in the "Trace" and "Retrace" direction. This motion is usually aligned with the longitudinal axis of the cantilever. If the cantilever is moved over the sample in the orthogonal direction, friction forces will twist the cantilever around its longitudinal axis causing the laser spot to move left or right on the photo diode. This way the friction properties of the surface can be measured [94].
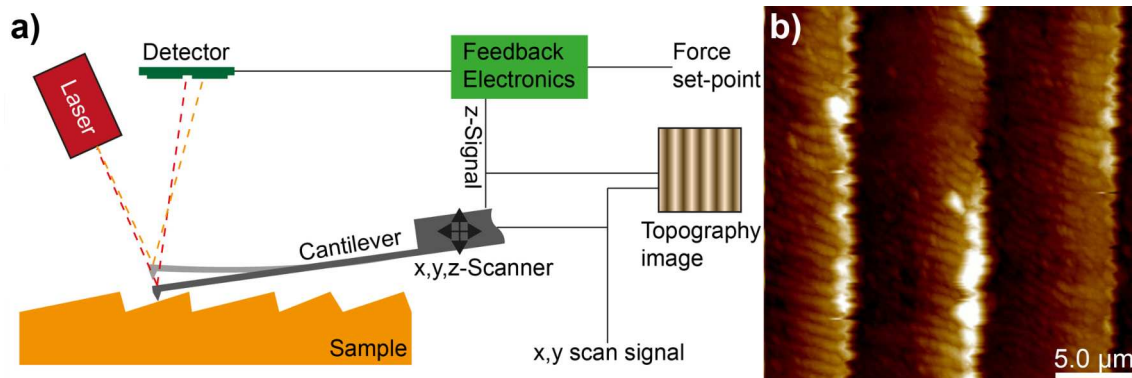
Figure 2.4: a) Working principle of an atomic force microscope. A cantilever is scanned across the surface. The cantilever is bent by surface features which is measured by the laser spot on the photo-diode. The feedback electronics adjust the height of the cantilever until the original signal is restored. This adjustment is recorded as measurement signal. **b)** AFM image of an optical grating fabricated by direct laser lithography. Scan size is 25 x 25 μm, structure height 1.5 μm.

All measurements shown in this thesis, that did not involve the measurement of friction, were conducted in a different measurement mode, the so-called "Tapping mode". Here the cantilever is rather driven to oscillate up and down at its resonance frequency. If the

cantilever approaches the surface, interactions between the surface and the tip, such as Van-der-Waals forces cause the amplitude of the oscillation to change. This amplitude change can then be fed into the controller, which subsequently adjusts the height of the cantilever over the sample [93, 95]. This contact-free measuring mode avoids some of the drawbacks of contact mode AFM such as tip wear or distortion of the measurements by thin layers of moisture on the sample. The AFM used for the measurements shown in this thesis is a Bruker Dimension Icon (Bruker Inc.). Data analysis was carried out using the Bruker NanoScope as well as the MountainsLab Multi Instrument analysis software (Digital Surf).

2.2.2 Confocal Scanning Microscopy

Confocal scanning microscopy (CSM) is a special kind of optical microscopy that enhances the resolution of traditional light microscopes and allows height measurements with nanometer accuracy [96, 97]. Figure 2.5 shows the confocal principle. As opposed to wide field microscopy a small pinhole is placed in front of the light source, leading to only a small area of the sample being lit in the first place. After the reflected light has travelled through the optical path of the microscope, another pinhole is placed in front of the detector. This ensures that only light reflected from the focal plane reaches the detector [98, 97]. Taking several measurements at different heights allows a reconstruction of the three dimensional surface from the individual slices taken. While the confocal principle gives the microscope excellent resolution in the vertical axis, the small area illuminated by the microscope makes it necessary to scan the light spot over the surface of the sample, making the measurement relatively slow [97]. Nevertheless a Mahrsurf Cm select confocal microscope was used for this dissertation, mostly for the measurement of polymer surfaces structured by roll-to-roll imprinting. Data analysis was conducted with the MountainsLab Multi Instrument analysis software, too.

2.2.3 Vertical Scanning Interferometry

Vertical scanning interferometry (VSI) is a measurement technique that uses the interferance of superimposed light waves. A broad band white light source with a coherence length in the μm range sends light onto a beam splitter that separates the beam in a reference and a measurement beam. The reference beam is reflected by a mirror, while the measurement beam is directed onto the sample. The reflected light is superimposed at the beam splitter and sent to the detector. If the optical path length and the length of the measurement arm are the same for a point on the sample surface, constructive interference occurs for all wavelengths and the intensity is at a maximum. By scanning the sample vertically, the height at which each pixels' maximum intensity occurs can be recorded, representing the three dimensional topography of the sample surface [99, 100]. Alternatively so-called phase shifting measurement modes are available. Here the reference mirror is shifted a precise fraction of the wavelength while the intensity is recorded for all pixels [101]. While more precise than traditional vertical scanning interferometry, phase shifting interferometry is
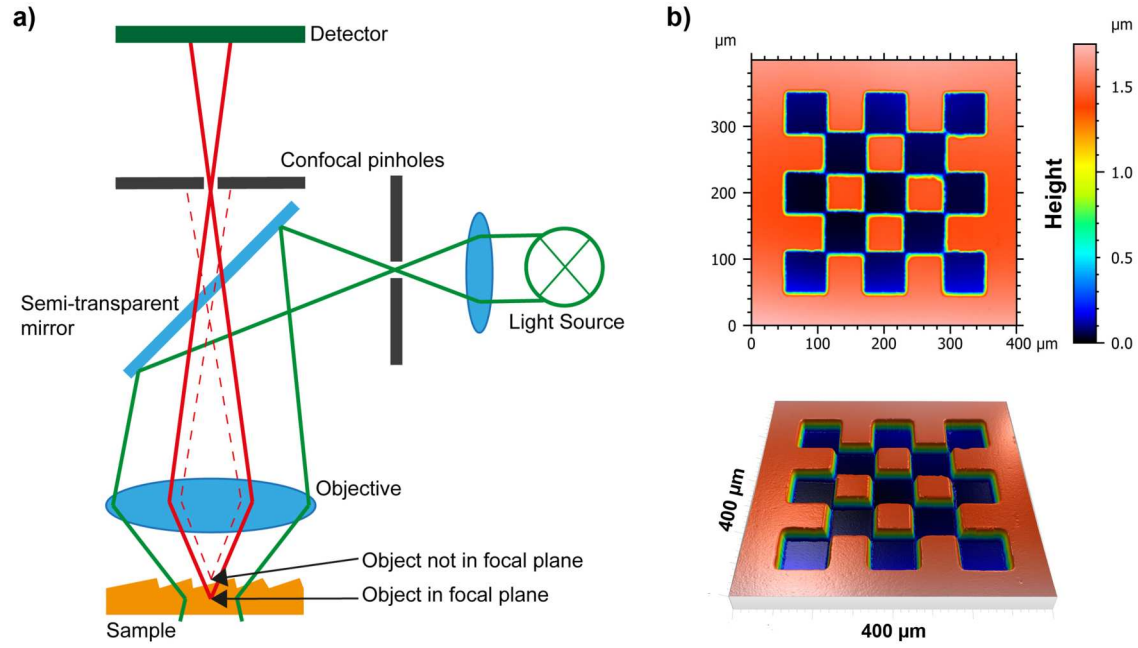
Figure 2.5: a) Working principle of confocal scanning microscopy. The pinholes after the light source and before the detector ensure only light from the focus plane reaches the detector. **b)** A polymer imprint of a checkerboard pattern, pictured by CSM.

usually the slower measurement technique. Both measurement modes were used in this work, the machine used was a Bruker ContourX-200 (Bruker Inc.). The data analysis was conducted using the Bruker Vision64 software.
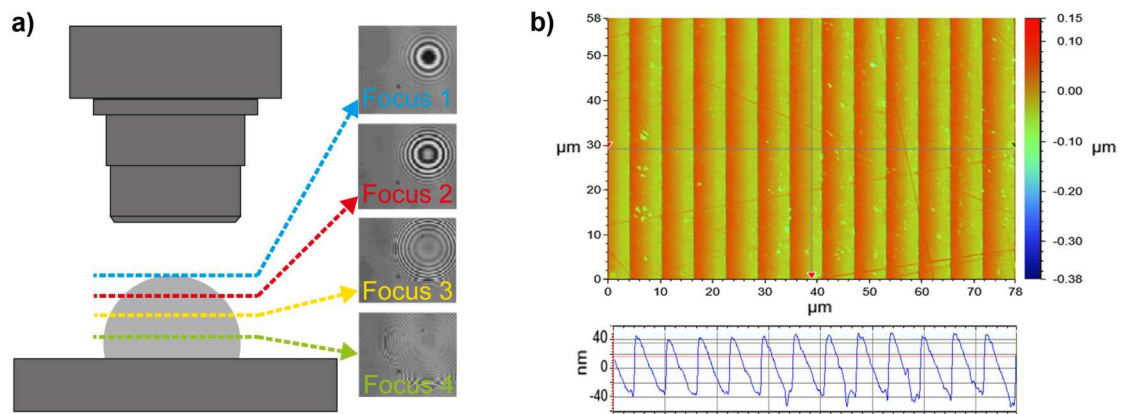
Figure 2.6: a) Working principle of vertical scanning interferometry. Image reproduced from [100]. **b)** VSI image and an extracted profile along the x direction of an optical grating. This would enable the measurement of, e.g., periodicity and height of the grating.

20

2.2.4 Contact Angle Measurement

The contact angle between a solid and a liquid commonly refers to the angle between the solid's surface and the surface tangent of the liquid-vapour interface in close proximity to the solid's surface. Usually the angle that is "inside" the liquid is referred to as contact angle. It is a measure for the wettability of a material. Very low contact angles show that a material is hydrophilic, for contact angles above 90° it is hydrophobic and contact angles above 150° are observed for superhydrophobic cases [102]. In this thesis, if not specified otherwise, the static (apparent) contact angle was measured. Other options commonly used are advancing and receding contact angles, that are measured while the drop is increasing or decreasing in volume, as well as the sliding angle of the droplet.
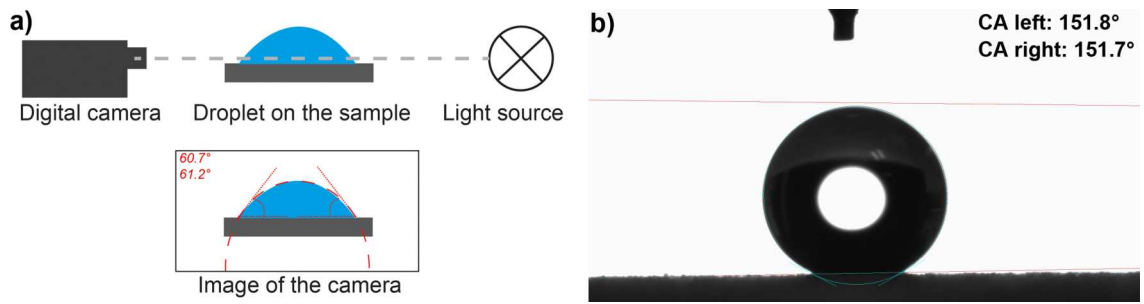
Figure 2.7: a) Working principle of sessile drop contact angle measurement. **b)** Image of a drop of water on top of hydrophobic nanofur as produced in Chapter 3.

Surface roughness or microstructures greatly influence contact angles [103] and can massively increase the contact angle of a liquid on top of a structured surface. More detailed information on this effect and its applications can be found in the introduction to Chapter 3. Several methods of measurement for contact angles exist [104]. The method applied in this thesis is the static sessile drop technique. Figure 2.7 shows the schematic of the sessile drop method as well as the camera image of a drop on hydrophobic nanofur. The sample is placed in a contact angle goniometer, between an adjustable light source emitting parallel light, and a digital camera. A hydrophobic needle is used to place a liquid droplet of a known volume on the sample. The sample itself, as well as the droplet, appear as a dark silhouette against the well lit background. Thus the shape of the drop can easily be recognized by appropriate software, an elliptical fit can be applied and the contact angle on both sides of the drop can be calculated. Since contact angle measurements usually have a relatively large uncertainty, in the best cases +-2°, multiple measurements were taken and averaged to ensure the validity of the measurement [105]. Furthermore it has to be noted that on superhydrophobc materials the droplet can often not be placed anywhere on the sample or rolls from the position with the very highest contact angle to a position where the contact angle is lower, which impedes precise measurements. The measurement device used in this thesis is an Dataphysics OCA20 (DataPhysics Instruments GmbH) contact angle measurement tool. The data analysis was conducted using the corresponding software of Dataphysics.

Chapter 3

Large-Scale Production of Biomimetic Nanofur

This chapter gives a first example of a large microtructured surface produced in the scope of this thesis - the so-called nanofur. Its surface is covered with many tiny, hair-like structures that equip the surface with superhydrophobic properties [106]. This biomimetic surface was chosen because it has been shown in past studies [106, 107, 108, 109, 110, 29], that nanofur can be produced with hot embossing machines with a simple sandblasted plate serving as a mold. In this way the challenging step of producing the rather large molds needed for roll-to-roll applications can be skipped and the feasibility of roll-to-roll imprinting for biomimetic surfaces can be tested using a comparably simple to manufacture sandblasted roller for structuring. This chapter gives a motivation for this kind of surface and its possible applications, an overview over similar techniques as well as the traditional method of producing nanofur in a batch-wise hot embossing process is presented. Lastly, the new approach for large scale production of nanofur is introduced and the influence of the process parameters on quality are discussed. Finally, an exemplary product made from nanofur, the so-called "nanopads" are introduced.

Parts of this chapter were already published - in a more condensed form - in the Beilstein Journal of Technology: *P. Weiser, R. Kietz, M. Schneider, M. Worgull, H. Hölscher. 'Roll-to-roll fabrication of superhydrophobic pads covered with nanofur for the efficient clean-up of oil spills'. In Beilstein J. Nanotechnol., 13, 1228–1239 (2022).* [111].

3.1   Nanofur and Traditional Fabrication Thereof

This section gives an overview on superhydrophobic surfaces and their preparation. Furthermore it explains the working principle of the nanofur surface and outline its fabrication methods. Lastly, a roller process enabling the production of large scale, thin polymeric nanofur will be introduced.

3.1.1 Superhydrophobic Surfaces

Self-cleaning surfaces utilizing the famous lotus effect have gained significant importance during the last twenty-five years [23]. Prominent examples include wall colors that let dust and soil drop off when it rains [112], hydrophobic coatings for glass surfaces (e.g. cameras at toll stations or windshields for better visibility [113]), anti-graffiti paints [114], as well as textiles that repel unwanted dirt [115, 25]. The lotus effect is commonly achieved by hierarchical nano- and micro-structuring of surfaces made from low surface energy materials leading to very high contact angles (larger than 150°). This strategy is inspired by the lotus leaf [23] but can be found on several other natural surfaces, too [27]. Since these superhydrophobic surfaces have so many possible applications a lot of research has been conducted into finding methods to mimic the functionality of the lotus plant. Some of the discovered methods will be presented in the next section.

3.1.2 Techniques for the Production of Superhydrophobic Surfaces

A multitude of techniques exist to prepare self-cleaning surfaces. Direct laser writing and electron beam lithography have successfully been employed to create superhydrophobic surfaces but due to low writing speeds these approaches are not viable for surface areas larger than some mm^2 [116, 117]. Various (soft) lithography techniques have been employed to create superhydrophobic surfaces; however these generally rely on copying surface information from a master (e.g. a lotus leaf) [116, 118] and are therefore often limited in size. Superhydrophobic surfaces can also be prepared using various dry/wet etching techniques including electrochemical HF etching, stain etching, metal assisted etching and reactive ion etching [115, 116]. So-called "nanograss" or "black silicon" is a surface modification of silicon where the surface is covered with many tiny high aspect ratio needle like structures - these needles equip the surface with superhydrophobic properties. It can either be prepared using a RIE process [119] or a laser assisted etching process described by Mazur et. al. [120] - requiring expensive silicon wafers as substrate as well as a femtosecond laser source [121, 122]. All these mentioned processes require potentially hazardous chemicals, chambers creating a suitable process environment or extensive and costly operations to form superhydrophobic surfaces and are therefore not particularly well suited for upscaling.

A rather cost effective, and therefore widely used, method for obtaining superhydrophobic surfaces is the use of silica based films, which can be applied by dipping the object in gel or via aerosol spray [123]. While providing excellent superhyrophobicity and an easy application even on very large surfaces – these films are not mechanically durable. Other options for chemically treated superhydrophobic surfaces, such as the use of fluorinated silanes, fluoropolymer coatings and carbon nanotubes exist, but are either rather costly to apply and/or potentially harmful to the environment. Almost all of the above mentioned examples are also limited to small areas, costly or have a limited potential for upscaling.

3.1.3 Basic Working Principle of Nanofur

A different approach to creating superhydrophobic surfaces is the so-called nanofur. Nanofur is a polymeric surface covered with a dense fur of very thin and long hair-like structures [108], which is shown in Figure 3.1a). This arrangement causes a significant increase of the contact angle ($>$150°) of water droplets placed on the surface, *i.e.*, the surface becomes superhydrophobic. The traditional wetting model first defined by Thomas Young and his coworkers in 1805 can be used to describe the wetting phenomenon of nanofur. The following formula describes the contact angle θ on a flat surface in relation to surface energy:

$$cos(\theta) \ = \frac{\gamma_{SG} - \gamma_{SL}}{\gamma_{LG}} \tag{3.1}$$

where γ is the surface tension of the respective interface and the letters S, L and G denote the phases solid, liquid and gaseous [124]. This contact angle can, according to Wenzel, be increased by microstructuring the surface. The new contact angle θ_W is then

$$cos(\theta_W) = r * cos(\theta) \tag{3.2}$$

where r is the ratio of the actual area to the projected area [103]. In this so-called "Wenzel-state", schematically shown in Fig. 3.1b), the drops fill in the spaces between the microstructures and seem to be "pinned" in place on the surface despite the high contact angle. This is sometimes referred to as "rose petal effect". Cassie and Baxter found that the contact angle changes to

$$\theta_{CB} = \varphi * (cos(\theta + 1) - 1 \tag{3.3}$$

if the drops rest on the apexes of the microstructures with φ being the fraction of the total area that is in contact with the solid [125]. In this Cassie Baxter state the droplets on the surface are usually more mobile and can roll around on the surface; often without leaving a noticeable trace. For a Cassie Baxter state to exist two criteria have to be met. Firstly the contact forces between the liquid and the microstructures must be of appropriate direction and sufficient magnitude to overcome the forces exerted by the unsupported droplet weight between the structures. Secondly the microstructures themselves need to be tall enough to prevent the bridges of liquid between them from touching the base of the microstructures [126].

The hair-like structure of the nanofur meets these criteria perfectly, since the diameter of the individual hair tips is as low as 200 nm and the height can be several micrometers; giving the structures an aspect ratio of typically over 10. It must be noted that by varying processing parameters, the nanofur can be prepared with fewer and shorter hair, leading to the drops being in the Wenzel state and thereby pinned in place if it was desired so, but for most applications a nanofur surface that keeps droplets in the Cassie Baxter state seems to be more desirable, as having mobile droplets with a high contact angle on a surface essentially equips the surface with self-cleaning properties equivalent to the lotus effect [127].

Additionally, the high increase of surface area increases the spreading of non-polar liquids such as hyrdocarbon oils. Therefore nanofur can be used to separate oil and water

efficiently [29, 106, 108]. The advantage, that this polymeric nanofur has over many of the methods presented in the previous section, is its simplicity and the relatively low cost of manufacturing, which will be further elaborated on in the following sections.
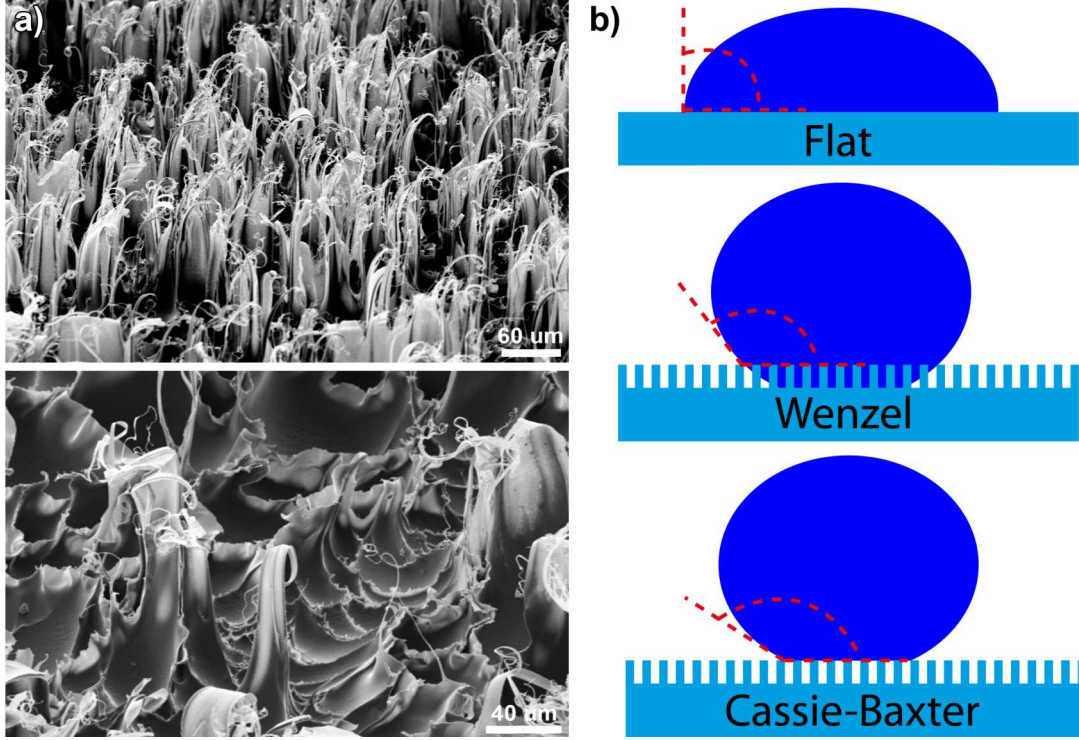
Figure 3.1: a) SEM images of P2P nanofur. The individual hairs are clearly visible. **b)** Wenzel and Cassie-Baxter state of a liquid drop on a rough / structured surface. Depending on aspect ratio, distance between high points and surface tension of the liquid, a droplet is in one of these states. Nanofur aims to keep drops in the Cassie-Baxter state in order to enable movement of the drops.

3.1.4 Plate-to-Plate Nanofur

Polymeric nanofur surfaces can be produced with minimal, very simple and cost effective tools and molds [106], as will be outlined in this section. This P2P approach using plate-to-plate (P2P) hot embossing machines was how nanofur was originally discovered and where much of the research took place.

This approach utilizes sandblasted steel plates as molds. The substrate plate serves as an attachment and is sandblasted with a coarse blast material (cast iron particles 0.8-1.2 mm) to increase mechanical adhesion, as is common in P2P hot embossing. The exact grit size is non-relevant. The upper plate is sandblasted as well and serves as the actual mold. For this mold plate, the grit of the blasting material plays an important role for the properties of the nanofur [66]. Usually a grit size of 50-70 μm was used. The influence of grit size will be further illustrated in Section 3.2. A schematic of the process is displayed

Figure 3.2: Production of plate-to-plate nanofur. **a)** Embossing step - The polymer is attached to the lower plate via hot embossing. To prevent attachment to the upper plate a polyimide film is placed between the polymer and the upper plate. **b)** Hot-pulling step - The heated upper plate is briefly brought into contact with the polymer - the surface of the polymer melts and fine hairs are pulled out of the surface.

in Fig. 3.2. The process starts with a hot embossing step where a sheet of thermoplastic polymer is attached to the lower plate via classic hot embossing. To prevent contact between the mold and the polymer a polyimide sheet is placed in between the upper mold plat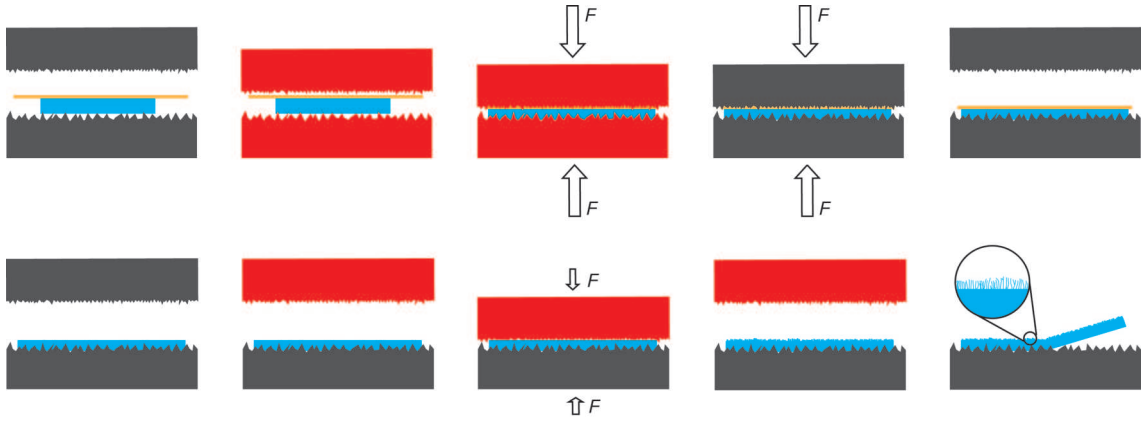e and the polymer. After the hot embossing step the polymer sample is attached to the substrate plate, which is important for the structuring step. The polyimide film is removed and the mold - but not the substrate plate - is heated above the melting point of the polymer. This is done - in contrast to traditional hot embossing - with the mold not being in contact with the polymer. The hot mold is then briefly (for about 1-2 seconds) brought into contact with the polymer sheet, melting the surface slightly. It is then slowly retracted from the surface. Since the viscous polymer melt adheres to the mold, tiny hair-like structures are pulled from the surface. The density and length of the hairs can be adjusted by varying the grit size when sandblasting the mold and the retraction speed of the mold in the hot pulling step. The temperature of the mold in the hot pulling step depends on the material processed but should generally be kept just above the melting range of the respective polymer, in a way that enables the polymer to flow, but keeps the viscosity of the melt as low as possible. Amorphous polymers seem to work better than those with highly crystalline structures. This can be explained as the viscosity of semicrystalline polymers changes abruptly in their narrow melting range - in some cases a deviation of only a few K can cause a significant change in viscosity [66]. This implies that the temperature selected for the process needs to be matched exactly and repeatedly for every run of the process, which can be challenging to achieve.

In terms of material selection several thermoplastic polymers such as polypropylene (PP), polyethylene (PE), polycarbonate (PC) as well as biopolymers such as polylactic acid (PLA) have successfully been processed into nanofur [108, 109, 110]. Not all polymers are suitable, e.g. some experiments showed that, while some types of PLA are working

very well, others do not work at all. For new materials it is often a case of trial and error and empirical work to find wether a material is suitable and, if so, what parameter settings to use in order to obtain a high quality product.

While plate-to-plate hot pulling is effective for the production of nanofur on a lab scale, it is a serial process and can only produce areas of some square centimeters at a time. This severely limits throughput and possible applications, which mostly rely on larger areas.

3.2 Roll to Roll Nanofur

In the preceding section, the traditional method for the fabrication of nanofur was presented. As stated above, the surface area per process run is limited to some cm² (in case of the machinery used at IMT, circles of ≈ 4 cm in diameter) since hot embossing is a serial process [66]. In the view of commercial applications, however, a continuous process is desirable. As demonstrated in the following sections, the continuous fabrication of superhydrophobic nanofur is possible in a roll-to-roll (R2R) process. For that we combined classical film extrusion with roll-to-roll structuring. The overall process relies only on machinery frequently used in industry, thereby enabling the cost-effective upscaling of nanofur fabrication for commercial applications [49, 112, 128, 129, 130].

3.2.1 The R2R Process for the Production of Nanofur

Figure 3.3 outlines the two main process steps. First, a thin polymer film is extruded on a sacrificial layer (Fig. 3.3a)). In a second step, the nanofur is hot-pulled from this extruded film in a R2R machine with a sandblasted roller. Subsequently, the nanofur film can be peeled of the sacrificial layer (Fig. 3.3b)). This sacrificial film is needed to provide the suitable process stability during the hot-pulling step. For comparable thick and mechanically stable polymer films (> 1 mm) it is also possible to omit this support layer. In the following, however, we focus on thin nanofur films fabricated with a sacrificial layer because thin films covered with nanofur seem to be more versatile in regards to possible applications.

Polypropylene (PP) was selected as base material for the hot pulling of nanofur for three reasons. First, even its flat surface features a comparable high contact angle (= 95° - 100° depending on exact polymer type [131, 132, 133]) which helps to achieve a high contact angle also for the structured surface. Second, we know from previous studies and literature that it has a comparable wide process window [65, 75], especially for the hot-pulling of nanofur [107]. Third, polypropylene is well-suited to be laminated on films of cyclic olefin copolymer (COC), which is important for the structuring step of the R2R process. Some experiments were also conducted with PC (Covestro Makrolon 2045 LED). For simplicity and time management reasons, these studies were carried out using 1 mm thick sheets - the process for producing thin nanofur, which is introduced below would work just the same with PC.

In the first step, we extruded a 250 µm thick COC film (TOPAS COC 8007s) from an extruder (Collin E20E - E30E) (Fig. 3.4a)) with cast film die. Since COC is non
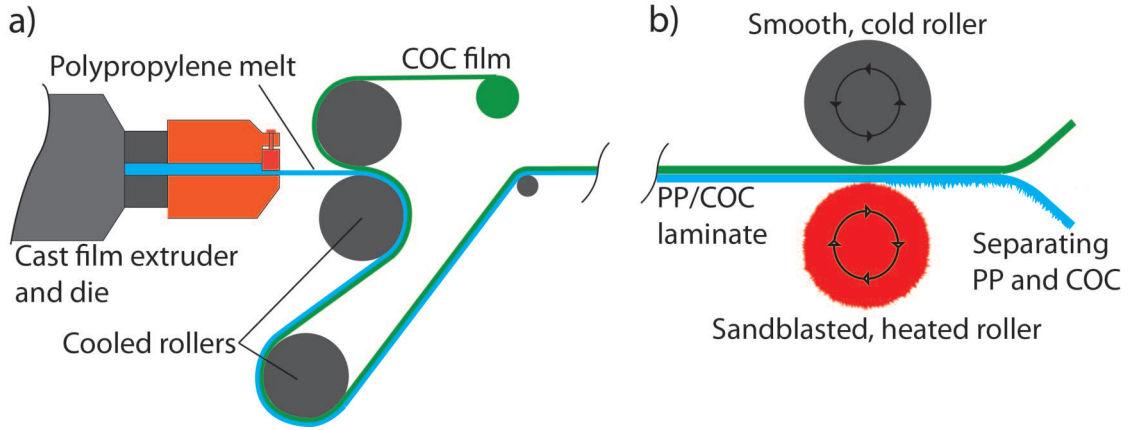
Figure 3.3: Schematic showing the roll-to-roll fabrication of a thin nanofur film by the example of the polymers PP and COC. **a)** Coextrusion of the PP on the COC support layer. The PP is extruded through a cast film die and laminated onto a previous extruded COC film in the calender. The PP and COC films stick strongly together but do not mix. **b)** Hot-pulling of nanofur from the PP film with a sandblasted roller. The COC film serves as a support layer keeping the PP from melting completely and thus enables transport through the calender. The gap size is set slightly below the nominal film thickness (≈ 100 μm) so that the films experience minimal embossing forces. Temperature of the sandblasted roller is set slightly (10 - 20 °C) above the melting temperature of the polymer. Finally, the structured PP and the sacrificial support layer of COC can easily be separated in a peeling motion. The content of this figure was previously published in [111].

hygroscopic, drying of the granulate is not necessary. The polymer melt was extruded at a temperature of 260 °C at 60 bars. Behind the extruder, there is a chill roll with smooth, temperature-controlled rollers (Collin CR 72/72/72-200 T) smoothing out and rolling up the film at about 1.3 m/min.

After the preparation of this COC film, which will serve as sacrificial support layer, the polypropylene is processed into a 150 µm thick film using the same extruder (Fig.3.4a). During this process, sketched in Fig. 3.3a), the film is laminated onto the COC film resulting in a PP/COC laminate. These polymers, when coextruded and therefore laminated together, adhere strongly to each other, but will not mix or form an inseparable material compound. Instead the polymers stick to each other reasonably well for further processing, but can be separated cleanly in a peeling motion if desired. The same is true for a PC/COC laminate [76]. This material combination is therefore equally suited for the production of thin R2R nanofur. For the structuring of the PP, schematically shown in Fig. 3.3b) the roller serving as mold was prepared in two steps. First, it was sandblasted with cast iron particles with a diameter of 0.8 - 1.2 mm and afterwards with white corundum with a particle size of 53 - 75 µm. This procedure results in a surface topography of craters and edges with finer spikes on top, just like the sandblasted plates used for traditional P2P nanofur. This sandblasted roller is mounted in a two-roller calender (Comerio Ecole, custom
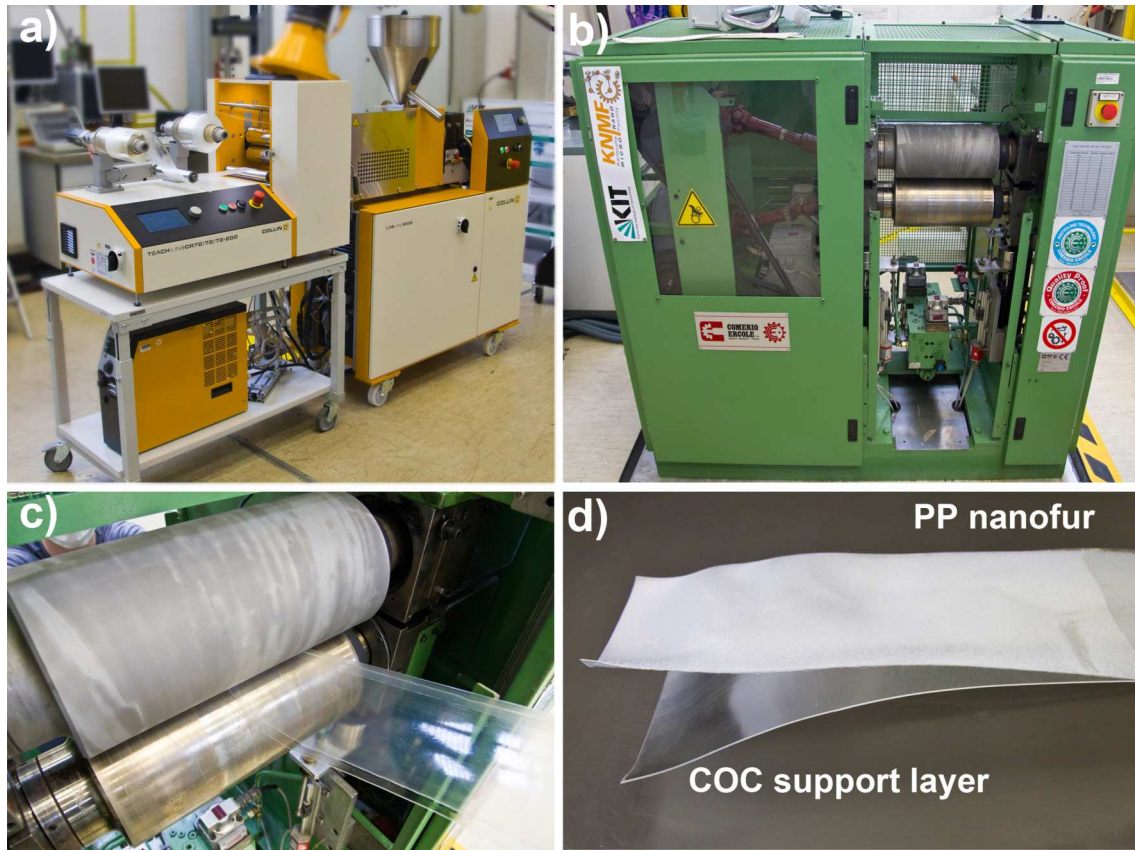
Figure 3.4: Photos showing essential fabrication steps of thin nanofur. **a)** Extrusion line with rolling unit to co-extrude the thin PP film onto the COC support film. The right roll is the coiled COC film. The left one is the completed PP/COC laminate. **b)** Photo of the lab calender utilized to structure the PP film. **c)** Close-up of the rollers of the lab calender. In this machine the upper sandblasted roller is heated and gets in contact with the PP side of the laminate. In this way, the nanofur hairs are pulled out of the PP film. The lower roller is smooth and not heated, but presses the film sandwich against the upper sandblasted roller. **d)** Finally, the PP and COC are separated through peeling. The content of this figure was previously published in [111].

build, Fig. 3.4b) and heated (Fig. 3.4c). We observed that best quality nanofur in terms of high contact angles is obtained if the temperature is set slightly above the specified melting point of the respective PP type (170 °C in our case). Using this temperature the viscosity of the polymer melt was sufficient to enable a hot-pulling process while at the same time not being too high, preventing the hair from collapsing while the polymer is cooling. The second roller of the calender was unheated and therefore at room temperature and had a polished surface. The gap between the rollers was adjusted to be slightly thinner (a few 10 µm) than the nominal material thickness. In this way, the laminated films experiences only minimal embossing forces during their pass through the calender and the rough sand-blasted surface of the heated roller pulls tiny polymer hair out of the melted surface of the

PP film. During this structuring step, the COC layer serves as a support layer enabling the processing of thin nanofur films. This support layer may be omitted, if the material thickness of the PP is sufficient (> 1 mm). If the PP film is to be thinner than this, the hot structuring roller will melt through the entire cross section polymer film, that will in turn, due to the many micro-cavities of the sandblasted roller surface, stick to it. Processing of this film, in the sense of pulling the material through the machine, is in this case not possible anymore and the roller has to be disassembled for cleaning and resurfacing. Since the melting temperature of COC is much higher than that of PP it can serve as a support layer for thin PP films. In our case the production of the PP/COC laminate and the structuring was done in two separate steps. However, in an up-scaled commercial process the structuring might follow the lamination process directly in combined machinery. After structuring, the PP film can be separated from the COC either by hand or – in the case of later envisioned commercial applications – by two winding rollers which separate the two foils with a peeling motion (Fig. 3.4d). The backside of the film is flat and smooth. The nanofur on the structured side of the film is imaged by scanning electron microscopy (SEM, Zeiss Evo 10) and shown in Fig. 3.5a). It features the typical crater-like topography of nanofur with hair on the crater edges [108].
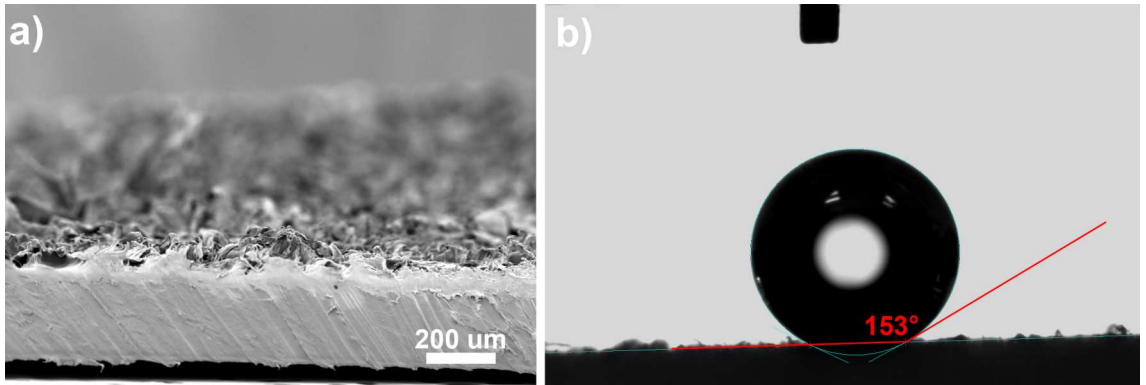
Figure 3.5: a) SEM picture of a side cut of a PP nanofur film (view angle 84°). **b)** A water droplet of 1 µL on top of the PP nanofur. The contact angle at this spot was 153°. The content of this figure was previously published in [111].

3.2.2 Influence of Process Parameters on the Quality of the Nanofur

Contact angles of water on top of the nanofur produced in the described way, scatter around the super-hydrophobicity limit of 150° (see Fig. 3.5b). Contact angles were measured with an commercial contact angle measurement machine (Dataphysics OCA 20) with distilled water utilizing the sessile drop method with a droplet volume of 1 μL. Due to the afore-mentioned hydrophobic nature of the sample surface, drops tend to roll to areas with lower contact angles when performing measurements leading to slightly lowered average contact angles. The relatively high measurement uncertainty of contact angle measurement, especially on hydrophobic surfaces, can further distort the measured values [105]. The quality

of the nanofur in terms of its hydrophobicity and oil absorption quantity depends on several parameters including hair length, their density, and their overall uniformity over the whole film area [107]. These topographical features depend strongly on the actual fabrication parameters, the influence of which is outlined in this section.

Roller gap size   The most important factor in the fabrication of high quality R2R nanofur is the gap size between the upper and lower roller. Ideally it is set a couple of 10 µm below the nominal material thickness – the contact angle is highest if the roller just touches the surface without applying high embossing forces. In our case it was set to 350 µm (nominal thick of the PP/COC laminate was 400 µm). Since the polymer laminate has small variations in thickness, a trade-off must be made between setting the gap at the optimal thickness for maximum contact angle and setting it below the nominal thickness to compensate for thickness variations in the processed film and structure the film more uniformly. If the gap size is set just at or slightly above nominal thickness only the thickest parts of the film are structured – if the gap is too small no hairs are pulled out of the polymer film – the resulting structures look as if they had been flattened. Figure 3.6 shows a nanofur film produced with a correctly set roller gap size and a film produced with a too narrow gap size. Figure 3.7 plots the contact angle against gap size. The best contact angle is achieved when the gap is set just below the nominal material thickness, i.e., the roller just touches the surface without excerting any significant embossing forces.
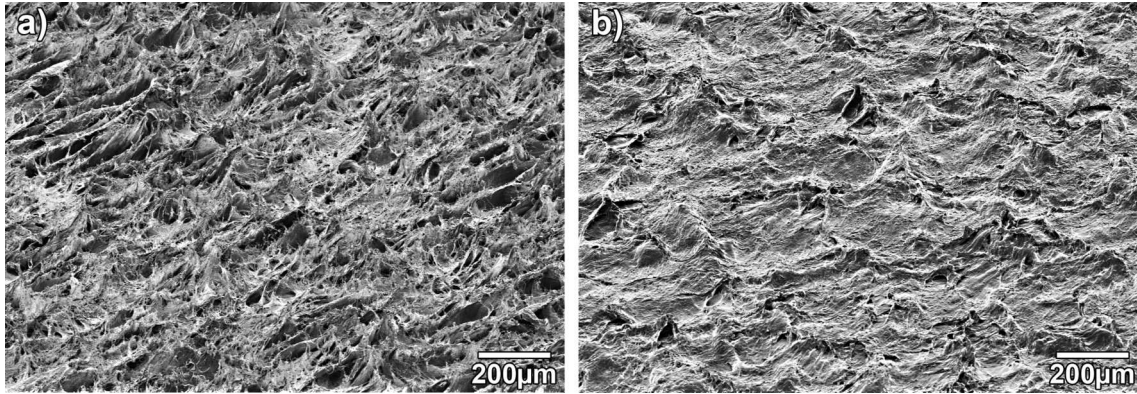
Figure 3.6: a) Nanofur produced with a gap size set 50 µm below nominal material thickness. Many long hairs are pulled out of the material. **b)** Low quality nanofur produced with a gap size set 500 µm below nominal material thickness. No hairs are pulled out of the material, the structures look as if they had been flattened. We conclude that a gap size just below the nominal thickness results in good quality nanofur while still structuring the film uniformly, compensating minor thickness variations in the film. The content of this figure was previously published in [111].

Roller temperature   The temperature of the roller is another important factor in producing high quality nanofur. Fig. 3.8 plots the contact angle of the nanofur against roller
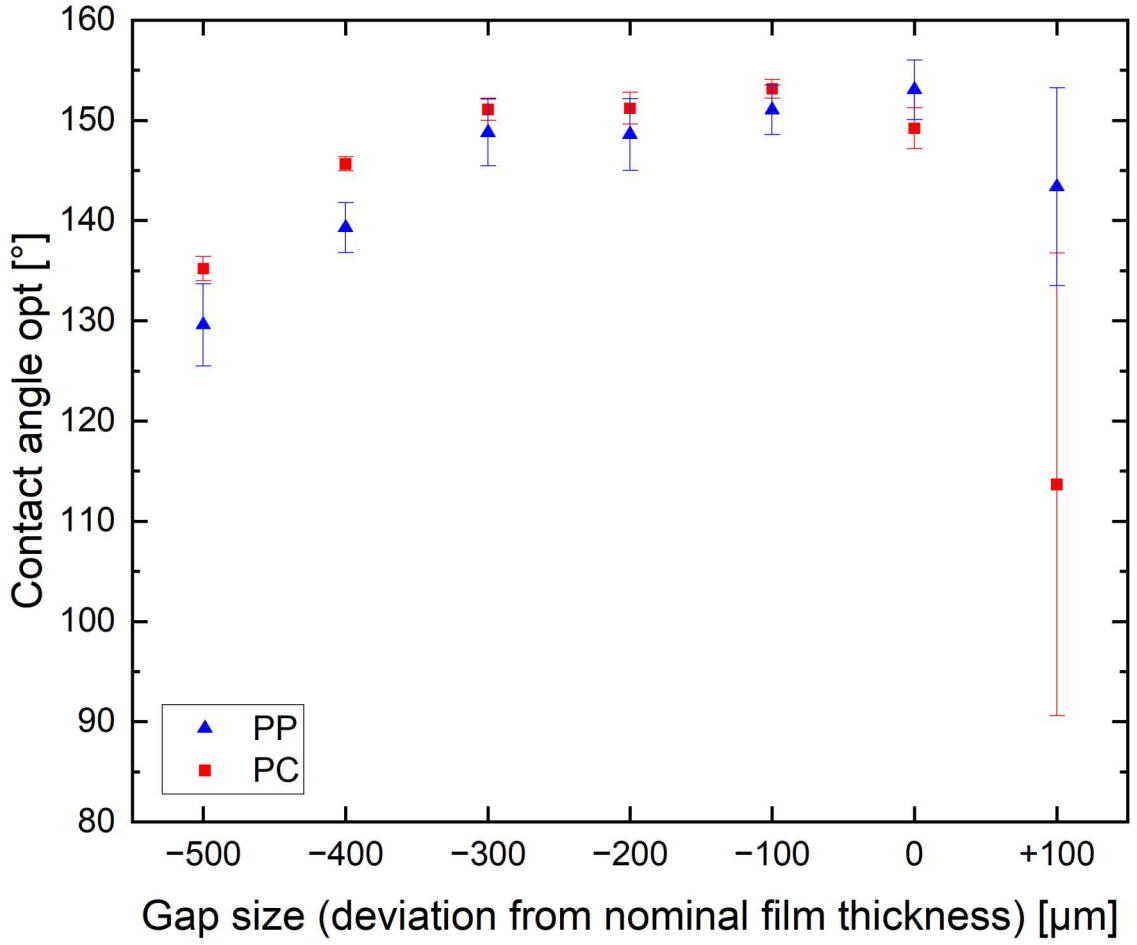
Figure 3.7: Influence of roller gap size on contact angle. For both PC and PP the gap size should be set just below the nominal thickness of the material. If the gap is set lower, the film is structured more uniformly, but contact angles decrease. If the gap is set too large, only some high-spots of the film are structured, resulting in the large error (see +100 μm.

temperature for PP and PC. As is the case in traditional hot pulling, the roller temperature should be set at around the melting point of the polymer, or, in the case of an amorphous polymer, in the lower part of the melting range. At this point a large increase in contact angle is measured, which makes sense since a roller, that is too cold, can obviously not structure the surface. If the roller temperature is set too high above the melting point the contact angle decreases for all tested materials (as well for PE and PLA). This might be a result of the change of viscosity of the polymer melt with temperature. If the roller temperature is set at the melting point, it melts the surface of the polymer, but the melt is still very viscous, enabling the hairs that are pulled out of the surface to keep standing upright while cooling. If the roller temperature is set higher, the viscosity of the polymer melt decreases leading to the hairs collapsing before they are sufficiently cooled off. The higher melt temperature also increases the time needed to cool below the melting point, leading to a further collapse of the hair structures, thereby decreasing the contact angle

of the nanofur. Semicrystalline polymers in particular can be more challenging, as their viscosity changes substantially around the melting point; in some cases in the range of only a few degrees. A notable exception from this rule is PP, which shows an exceptionally large processing window (see Fig. 3.8). In general the roller temperature is also dependant on the conveying speed - if the conveying speed is set considerably higher to increase throughput, the roller temperature might also need to increase to transfer the same amount of energy to the material, thereby melting the same quantity of material. Since the equipment used for these tests was not optimized for speed, this was not further tested.
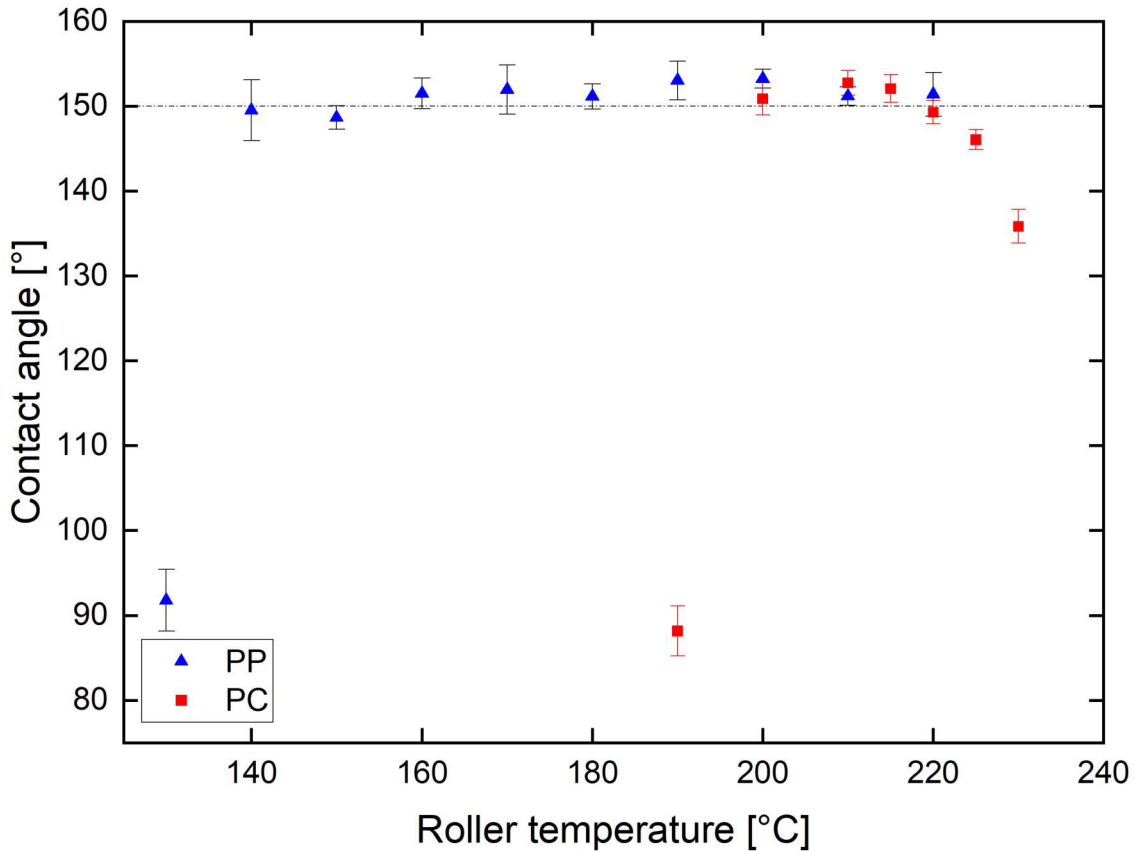
Figure 3.8: Contact angle of water droplets (1 μL) on nanofur produced at different roller temperatures. The dotted line marks the limit for superhydrophobicity. PP has a very wide processing window ranging from 140 °C to at least 220 °C. The processing window for PC on the other hand is quite narrow (200 to 215 °C).

Hair length / -density The hair length can be controlled via the conveying speed of the calender, while keeping the roller temperature constant. Slower conveying speed leads to longer hair. To a certain extent this can be beneficial because generally high aspect ratio hair led to high contact angles. However, if the hair becomes too long and thin, it bends under the weight of the water droplets. It was observed that this effect considerably slows the speed at which water droplets roll around the surface, even if the surface is still

superhydrophobic. Furthermore, the hair apex of especially long hairs might penetrate water drops, pinning them in place despite the high contact angle. If the conveying speed is set too high on the other hand, the pulled hair becomes too short and water droplets might touch the surface between the hair. In this so-called Wenzel-state, the droplets are pinned in place [108]. This is sometimes referred to as rosepetal effect [134].

The hair density of the nanofur is indirectly controlled via the sandblasting of the structured roller. The optimal roughness of the roller also depends in the actual polymer type. For PP, PE and PC the best results are obtained by sandblasting the roller at first with 0.8 - 1.2 mm cast iron particles and subsequently with white corundum with a particle size of 53 - 75 µm. For polylactide acid (PLA) smaller corundum particles with a size of 8 - 10 µm had to be used for the second sandblasting step to get sufficient hair density.

Polymer residue   Special consideration must be given to the polymer residue sticking to the structuring roller (Fig. 3.4c). If the residue polymer stays on the hot roller for too long – especially with oxygen present at ambient conditions - it might decompose and inhibit the subsequent structuring process. We observed that this effect leads to reduced quality of the nanofur, *i.e.*, reduced contact angles. It is therefore important to keep the process running in a continuous fashion as old residues are replaced by newer polymer material. Actually, the contact angle is highest when the roller is newly sandblasted and therefore not covered with any polymer residue. Once the heated and sandblasted roller is covered with residues of polymer the quality of the nanofur reduces slightly.

In order to quantify this effect, the contact angles along a 50 m long film of PP nanofur produced as described above (see Fig. 3.9) were measured. The contact angle is about 154° at first but dropped by four degrees after the first turn of the rollers before it becomes nearly constant with values slightly below 150° for the remainder of the strip. While technically slightly under the limit for superhydrophobicity, these contact angles are still sufficient for almost all typical applications, since the droplets easily roll off the surface even at minimal tilt of the sample. Furthermore the rather large measurement uncertainty of contact angle measurements - especially in the hydrophobic regime - has to be taken into account [105].
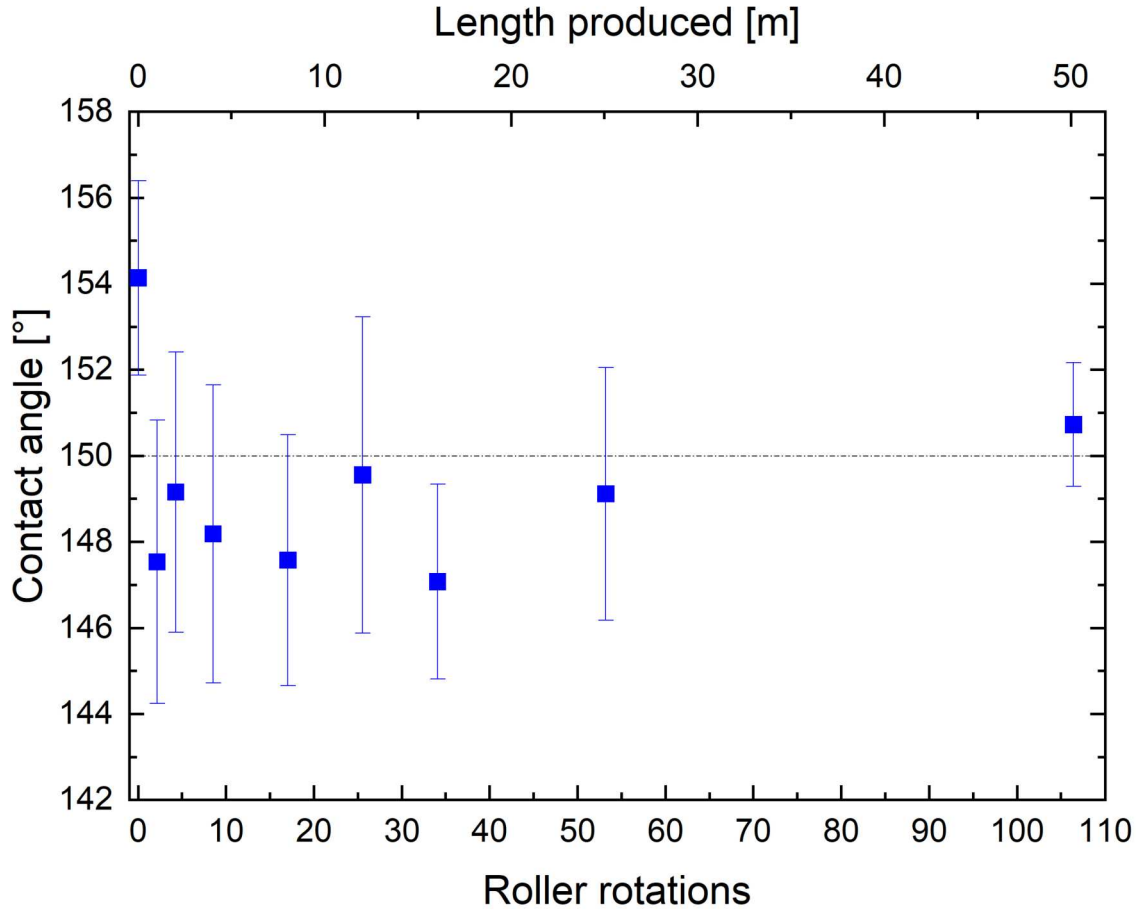
Figure 3.9: Contact angles measured along a long film of nanofur produced in the described R2R process. The same spot on the roller is used many times to pull nanofur (one rotation of the roller is $\approx$ 0.5 m). A drop of about four degrees is observed when the newly sandblasted roller is first covered in fresh residues – as long as the production process is not interrupted from there on no further decrease in contact angle occurs for many meters of produced nanofur. The content of this figure was previously published in [111].

3.2.3   Comparison of R2R Nanofur to P2P Nanofur

As stated above, the contact angle of R2R nanofur tends to be around 150°, which is nearly the same as for P2P nanofur. However the surface of a polymer processed by roll-to-roll is not only significantly larger but also more uniformly structured than the small area that can be structured by P2P hot pulling. So, there are less, if any, "bad" parts on the surface that have a contact angle or hair density so low that droplets stick to the surface.

Since the absorption of non polar liquids is one of the advantageous features of nanofur, its oil absorption capacity was measured, too. Pieces of the R2R-fabricated nanofur PP film were submerged for 20 s in two different kinds of oils that had been used in previous studies as well [110]. The excess oil was let drip off for 30 s, and the absorbed oil mass was determinded by weighting [29]. Two oils with different viscosity were used for this analysis.

The hydraulic oil TOTAL Azolla ZS 32 had a viscosity and density of 32 mm^2/s, 875 kg/m^3 and the gear oil TOTAL Carter EP 320 of 320 mm^2/s and 910 kg/m^3, respectively. As expected from a previous study [29] the absorption capacity increases with viscosity as the absorbed film thickness increases with this parameter. The PP nanofur absorbed 185 g/m^2 of Azolla 32 and 561 g/m^2 of Carter EP320. Due to these observations, it can be concluded that the overall water repellency and oil absorption capacity of the R2R-fabricated nanofur film is in the same range as for nanofur fabricated with the traditional hot-pulling process in a hot embossing machine [110].

Figure 3.10: Series of images demonstrating the oil absorption of polymeric nanofur. The drop of colored oil (Azolla ZS 32) is selectively absorbed from a bowl of water, thereby cleaning the water. The piece of nanofur was submerged for about 10 s.

To test the capability of oil/water separation of the nanofur a drop of oil was placed in a bowl of water. The floating drop of oil can then selectively be absorbed by the nanofur and therefore be separated from the water. Figure 3.10 shows a series of images of this process. The whole sequence of pictures took around 10 s. Once contaminated with oil the contact angle of the nanofur with water decreases below 90° because the contact angle is now mainly defined by the oil/water interface and not by the nanofur structure anymore. This characteristic feature of the nanofur to separate oil from water was used in the next section to develop an exemplary product - the so-called nanopads, that can aid in clean-up of small oil spills.

While the nanofur produced in this process does not differ significantly in function, i.e, contact angle and oil absorption capacity from nanofur produced by classical hot embossing, the overall structural appearance of the microstructures is different (see Fig 6). While the hot embossed nanofur consists of tiny hairs standing relatively straight in regard to the surface, R2R nanofur tends to form larger ridges that culminate in hair like tips. Also, since the rollers rotate, these ridges tend to be slightly slanted against the direction in which the polymer travelled through the calender, which is shown in Fig. 3.11

3.3 An Exemplary Nanofur Product - Nanopads

As stated above, it is a remarkable property of nanofur that it is superhydrophobic and oleophilic at the same time. Nonpolar liquids are immediately absorbed by the polymeric surface while polar liquids are repelled [108]. Consequently, mixtures of oil (nonpolar)
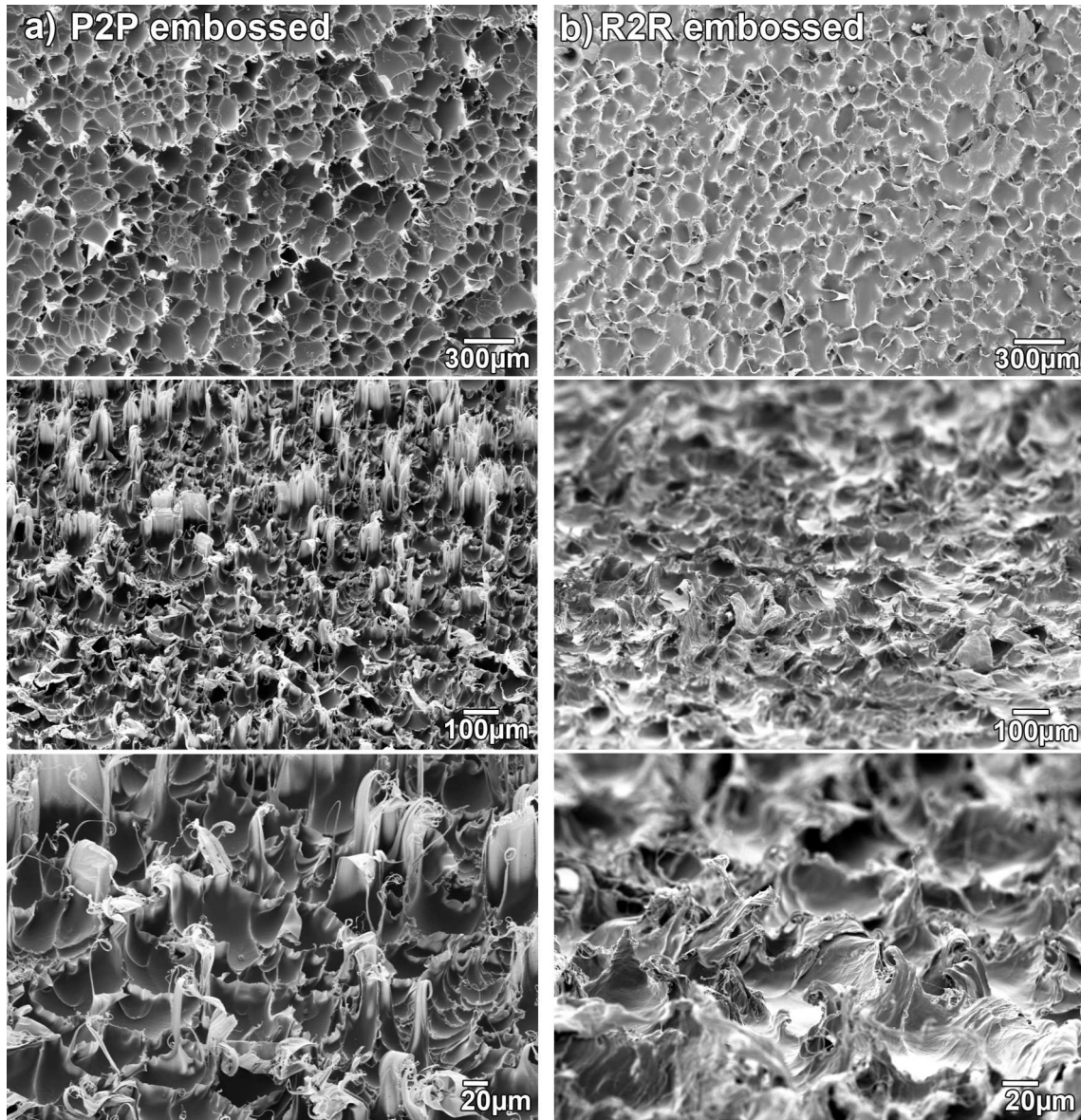
Figure 3.11: Comparison between nanofur produced by **a)** classical hot embossing and **b)** R2R fabrication. The topmost pictures are top views, the others were taken at tilt angle of 60°. Even if morphological differences are obvious – the two samples do not differ in function, *i.e.*, contact angle. The hairs of the hot embossed nanofur are standing separately and point upwards with a high aspect ratio. For nanofur produced in a roll-to-roll process, the structures consist of ridges that culminate in hair like structures. These ridges can be slightly slanted against the against the direction in which the polymer traveled through the calender. The content of this figure was previously published in [111].

and water (polar) are easily separated. A promising application of nanofur is therefore the cleaning of oil spills [29, 110]. This behavior can be also utilized for the fabrication of membranes which filter oil out of water (or vice-versa) [106]. For that, the nanofur is

perforated with small holes, so that oil passes through the polymeric film while the water – due to its high contact angle with the surface - cannot penetrate the holes. As shown in the following, we used this property for the development of an exemplary product for the clean-up of oil-spills made out of nanofur – so-called nanopads.
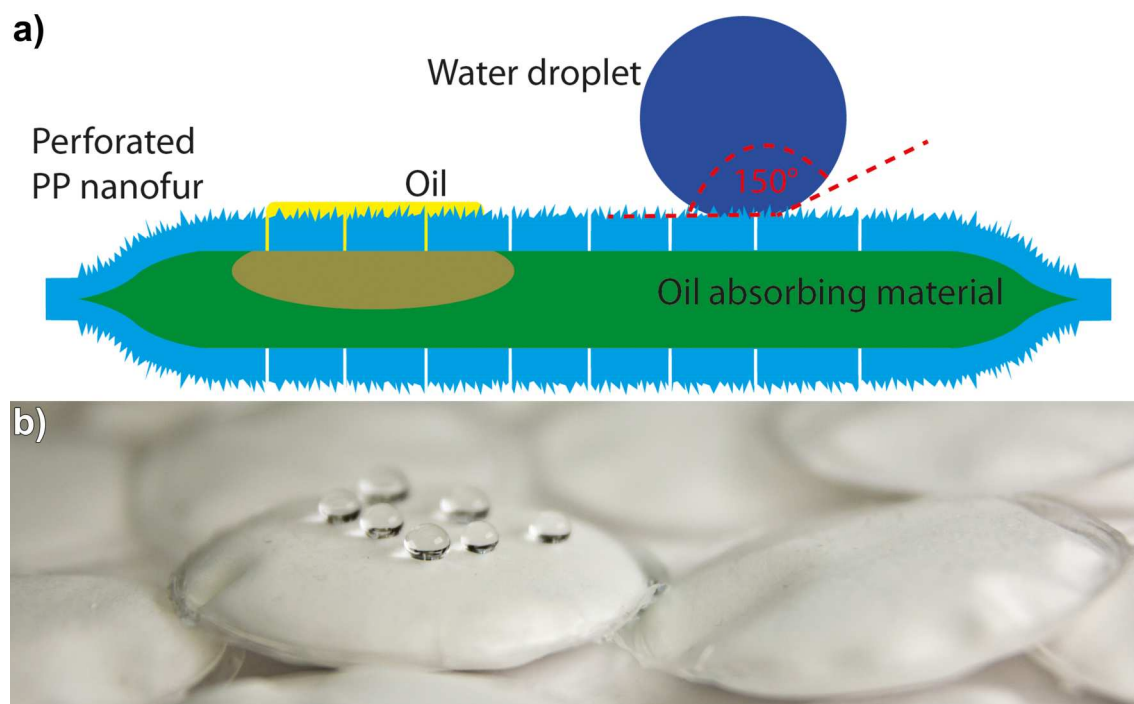
Figure 3.12: a) Schematic side view of the nanopads indicating their functionality. Two perforated polypropylene films, which are covered with nanofur on their respective outside, enclose an oil absorbing material. The two foils are heat-sealed at the edge. If the nanopads are dipped in an oil spill, the oil is adsorbed by the nanofur, penetrates into the small holes, and is finally absorbed by the enclosed oil absorbing material. The small holes are mechanically punched into the nanofur film and have diameters of about 100 µm. **b)** Photo of several nanopads with a diameter of 48 mm produced as described in the text. Due to their nanofur cover, the pads are strongly water repellent as demonstrated by the water droplets positioned on the nanopad in the middle of the photo.

Standard practice for cleaning up oil spills is scooping the oil film together using barriers, skimming the oil slick and using separators to clean the remaining water. This method is limited to suitable conditions and - even under best circumstances - only recovers about 35 % of the spilled oil [135, 136, 137]. While somewhat effective for large-scale oil spills, this is unpractical for smaller spills, e.g., after car accidents or small tank leaks. Burning the oil is a method often used as well, but requires a certain thickness of the oil film and low water content in the oil. Furthermore secondary pollution is a problem with burning [137]. Chemical dispersion can be a last ditch effort to protect sensitive areas from an oil spill but does not separate the oil from the water; many dispersants can also be toxic to

the environment [136]. Commonly used sorbents used in the emergency response to oil spills absorb not only oil but also large quantities of water [29, 137]. The schematic design of pads made from nanofur which absorb oil but no water is shown in Fig. 3.12a). The nanopads embed an oil absorbing material, such as cotton, in a perforated polypropylene film covered with nanofur. The nanofur easily separates the oil from the water, the oil passes through the micrometer-sized holes, so that finally, the absorbent material traps the oil.
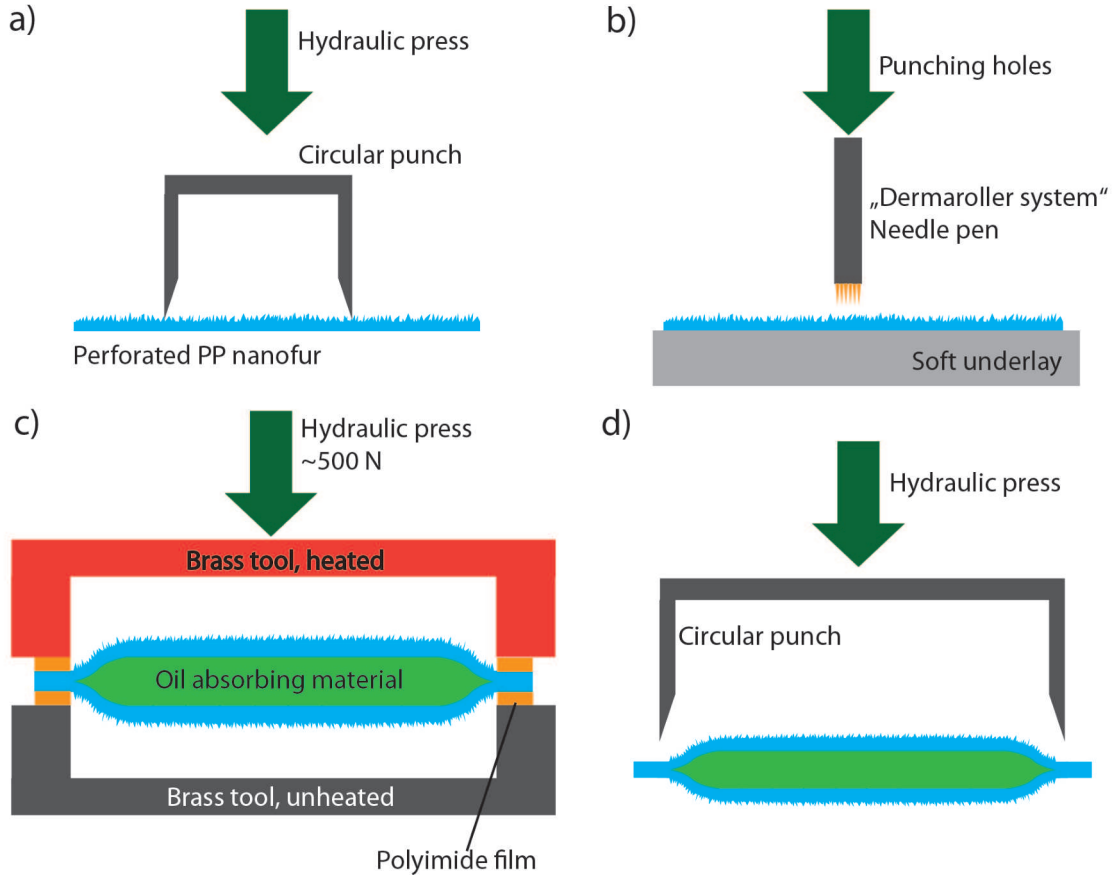
Figure 3.13: Schematic of the nanopad fabrication steps. **a)** Circular cut-outs are produced using a circular punch. **b)** The pieces are perforated by punching holes with a needle pen. A soft underlay guarantees the needles penetrating the film completely. **c)** Two cut-outs are filled with oil absorbing material, placed in between polyimide masks, and heat welded. **d)** The uneven edge is cut off with a circular punch. The content of this figure was previously published in [111].

Figure 3.12b) shows a photo of several manufactured nanopads. The fabrication steps are sketched in Fig. 3.13 while Fig. 3.14 shows photos of these intermediate fabrication steps. The nanopad fabrication starts with the cutting of circles with a diameter of 60 mm out of the structured PP film (Fig. 3.13a). A round punch is utilized for this cutting step. Afterwards, the nanofur film is perforated. This perforation can be conducted with various types of needles [106]. However, in order to speed up this process step, a Derma pen (DRS Dermaroller System) with 42 needles with a diameter of 100 μm each (Fig. 3.13b, 3.14a) was used. After punching 15-times, every circular nanofur film had about 600 holes.

Afterwards two films were loosely connected with adhesive tape. This step simplifies filling the pad with a predetermined amount of oil absorbing material (see Fig 3.14b). For the nanopads analyzed in the following we used 1.1 g of cosmetic cotton (Rossmann AG) or "Deurex Pure" respectively. "Deurex Pure" is a wax based, cotton like product that is specifically produced for oil spill cleanup [138]. The filled pad is then placed in between two polyimide films (DuPont Kapton, 50 μm) just covering the edge to prevent cutting through the material during heat sealing. This welding was done in a custom-made tool consisting of two hollow brass cylinders with a diameter of 48 mm and a wall thickness of 2 mm. The cylinders were heated to 230 °C and pressed on the pad from both sides for about 15 s, welding the two PP films together (see Fig. 3.13c, 3.14c). The nanofur was destroyed in the area the pads are welded together. Afterwards the uneven edges were cut off using another circular punch with a diameter of 48 mm (Fig. 3.14d).

The resulting pads have a surface area of about $2\pi(d/2)^2 = 30.4$ cm^2 covered with nanofur. Due to the hot welding, the nanofur structure close to the edge is destroyed and a 2 mm margin is not covered with nanofur. The height of the final pads is about 10 mm. Extrapolating the shape of the pads as a spheroid their volume can be calculated as $4/3 * \pi r^2 * h/2 = 10.13$ cm^3.

To measure the quantity of oil the pads can absorb, they were fully submerged in hydraulic oil, transmission fluid, and petrol. The viscosities (at 40 °C) and densities of these exemplary oil products are: TOTAL Azolla ZS 32: 32 mm^2/s, 875 kg/m^3, TOTAL Carter EP 320: 320 mm^2/s 320 kg/m^3, and Super 95: 0.85 mm^2/s, 740 kg/m^3 at 40 °C. These values span a typical range of viscosities for various engine oils and transmission fluids used in everyday tasks and machines [139]. Therefore, such oils are typical pollutants that are likely to cause oil spills, which are supposed to be cleaned up by nanopads.

In regular intervals the pads were taken out of the oil and excess oil was allowed to drip off for two minutes Figure 3.15 shows photos of nanopads after soaking in Azolla ZS 32 after various amounts of time. For better visibility the oil was colored using a small amount of black oil paint. Figures 3.15 and 3.17 show the quantity of oil absorbed by the pads over times. The pads absorb immediately about 0.6 to 0.8 g of oil. This amount is consistent with the quantity of oil that the nanofur surface absorbs. After that, the oil absorption per time decreases because the oil has to penetrate into the nanopads through the punched holes. Therefore, it takes some hours before the pads start to saturate. Finally, additional oil is absorbed very slowly. The last measurement was taken after 48 hours to ensure that the pads were saturated completely. The absorbed quantity of oil is similar for all three
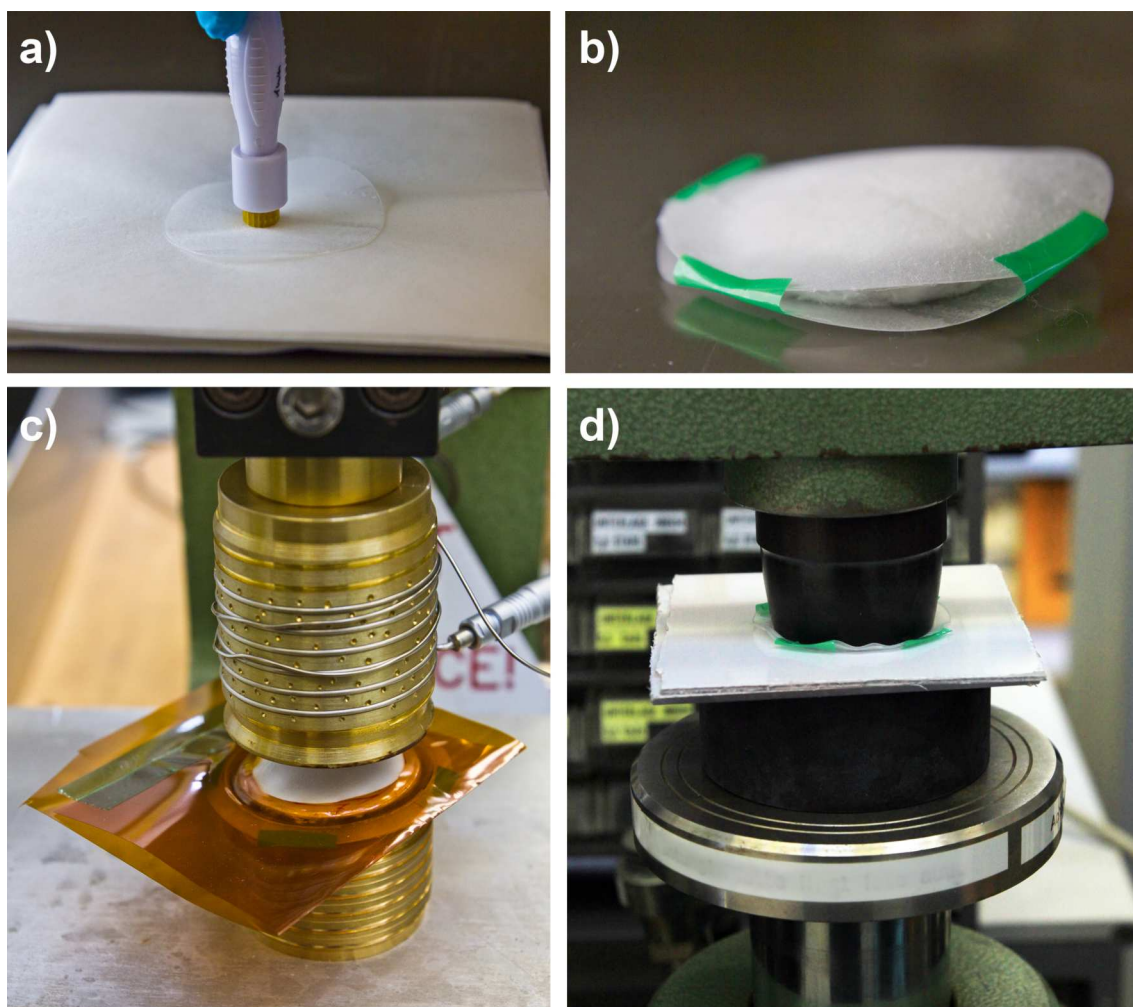
Figure 3.14: Fabrication nanopads from polypropylene nanofur film. **a)** In the first step, circular pieces are cut from nanofur film with a circular punch. Subsequently, tiny holes are pierced in the nanofur film using a needle pen. The needles had a diameter of about 100 µm. **b)** To simplify filling the pads with oil absorbent material, the two halves are held together by scotch tape. **c)** Such a preprocessed pad is placed between two polyimide films to avoid cutting through the material while welding. The upper, hollow cylinder is heated and then pressed onto the pad for 15 s welding the two halves together. **d)** Finally, a circular punch is applied to cut off the excess edge leading to an evenly round pad. The content of this figure was previously published in [111].

tested oils, the absorption speed, however, is not. As it can be expected, the viscosity of the oil determines how fast the oil penetrates into the nanopads. A lower viscosity leads to faster absorption. As soon as the nanofur is covered with oil, this oil film prevents water from penetrating into the nanopads.
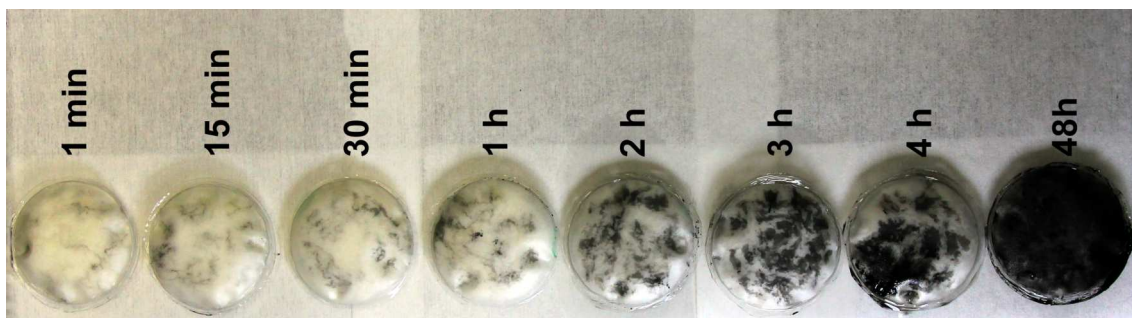
Figure 3.15: Cotton filled pads after absorbing colored Azolla ZS32 oil for increasing amounts of time.
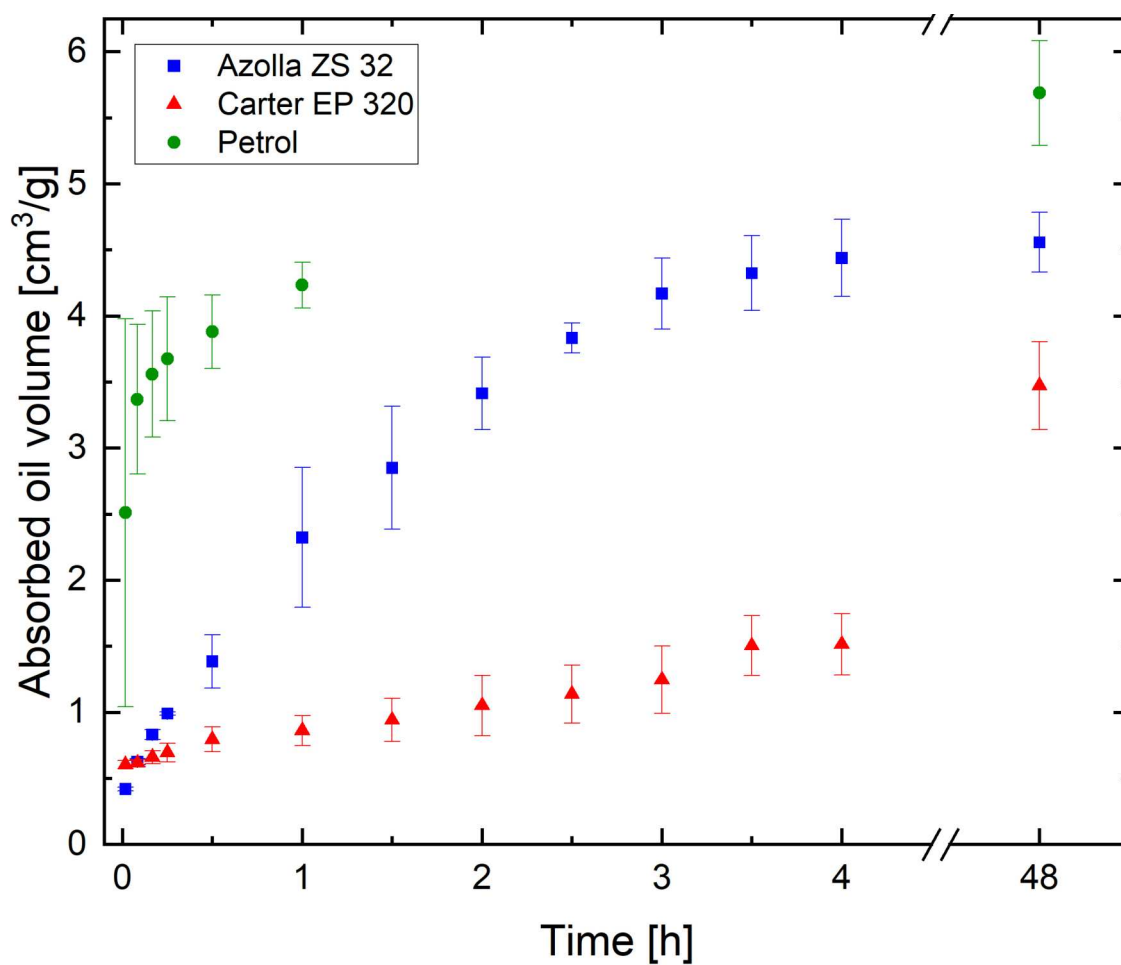
Figure 3.16: Volume of absorbed oil per g of the pads filled with cotton. The higher the viscosity of the oil the slower it is absorbed. After about 4 h the oil absorption happens very slowly. The content of this figure was previously published in [111].

These nanopads are obviously just one exemplary product that can be made from thin polymeric nanofur, proving its usefulness. Many other applications from packaging
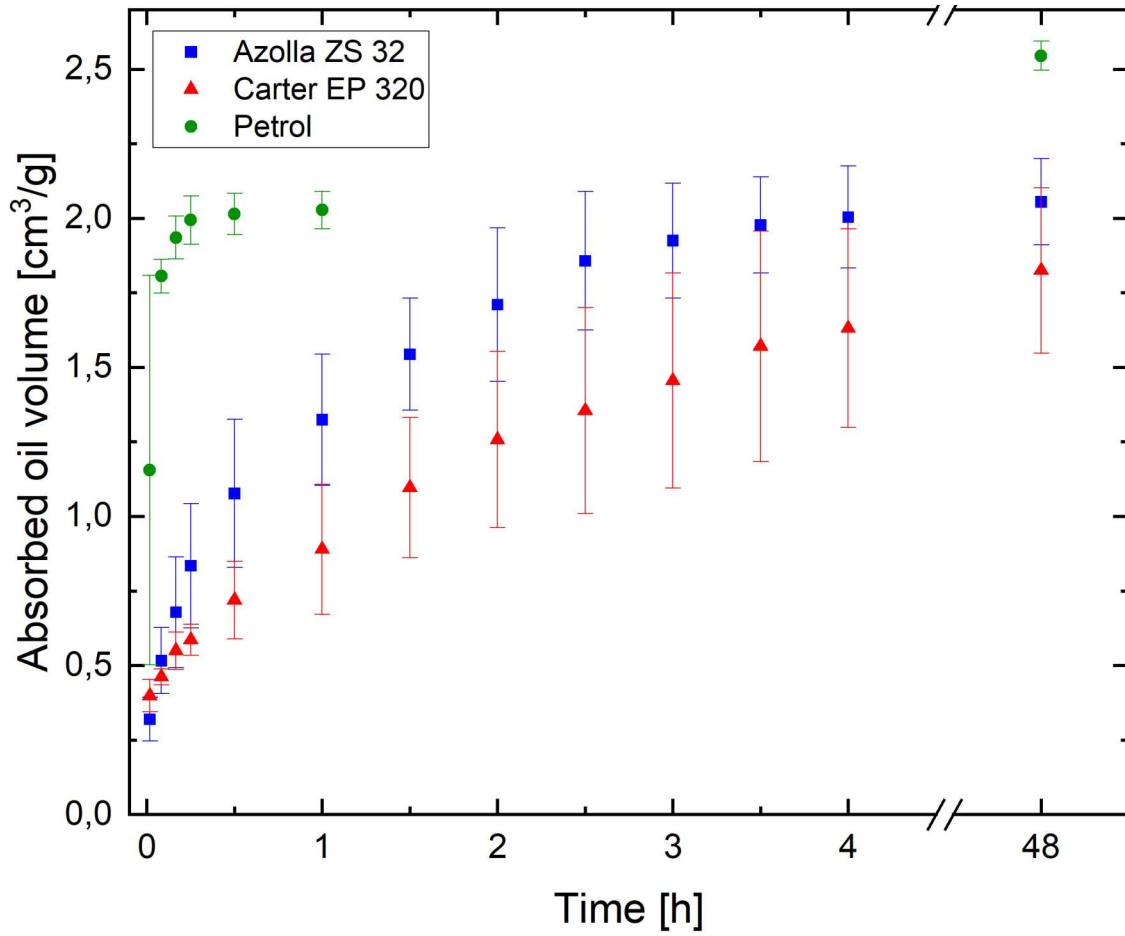
Figure 3.17: Volume of absorbed oil per g of the pads filled with Deurex. The higher the viscosity of the oil the slower it is absorbed. After about 4 h the oil absorption happens very slowly. Interestingly, the total amount of oil absorbed is significantly lower than for the pads filled with regular cotton from cosmetic pads.

to new types of filters can be envisioned. The process developed for the production of thin nanofur showed good results. Now it is the task of potential industrial partners to further optimize and implement a (combined) process and bring it to market in the form of actual products. The development of this process proofed that roll-to-roll hot embossing is a promising technology for the large scale production of biomimetic surfaces. Unfortunately, this process cannot be used to produce arbitrary surface features. The next chapter describes an approach to roller embossing of arbitrary structures.

Chapter 4

Direct Large-Scale R2R Micro-Structuring of Polymer Film

This chapter focuses on the R2R embossing process that was developed building on the methods and lessons learned when optimizing the R2R hot pulling process presented in the previous chapter. This roll-to-roll hot embossing process aims to imprint distinct features with precisely defined geometrical shapes as opposed to the non-ordered surface of the nanofur. The first section gives a short introduction to R2R hot embossing and the existing approaches. The next section introduces the basic method developed in this thesis, while the third section depicts details of the attachment of molds to the structuring roller. The fourth section introduces an approach to produce large scale molds for roller embossing and the last section describes the optimization of the new R2R process.

4.1 Introduction to R2R Hot Embossing

The demand for large area patterned polymer film has been rising in recent times because it is frequently used in a variety of commercial applications like microfluidics [140], biomedical applications [141], sensor applications [142], optics and especially coatings for photovoltaic panels [143]. Common approaches to manufacture these polymer films include micro injection molding and hot embossing [144, 145]. Especially for thin films, hot embossing can have some advantages [145]. A explained in detail in Chapter 2, it consists of four basic steps. Heating and melting of a semi-finished product - usually a polymer film or thicker sheet - then imprinting a mold in the molten polymer using an appropriate embossing force. After that the polymer is left to cool and solidify while still under pressure in the mold. Once the polymer has sufficiently cooled the part can be demolded. This way of traditional (P2P) hot embossing has always had some drawbacks; mainly the limitation to a relatively small structurable area, due to enormous embossing forces needed when embossing larger areas as well as low tolerances for alignment/angle errors and flatness of the plates, which becomes increasingly difficult to achieve for large areas. Furthermore the batch wise production with long cycle times and therefore low productivity has been a limiting factor for traditional hot embossing. If very large substrates have

to be structured, e.g., polymer films for solar panels, fabrication of molds with an area of multiple square meters becomes challenging and costly. While P2P hot embossing is a very useful tool in laboratory settings, these limitations have kept the technique from becoming a widespread process in industrial settings. To overcome the limitations of traditional hot embossing several variations of so-called roll-to-roll (R2R) hot embossing processes have been developed. The review [49] gives a good overview over the currently available options for roller embossing.

In general roller embossing can be divided into two distinct groups. Roller-to-plate (R2P) embossing and true roll-to-roll (R2R) embossing. In R2P embossing (see Fig. 4.1a) a structured and heated roller is moved over a stationary, temperature controlled plate. The roller is pressed onto the polymer with the set embossing force, melts the polymer on contact and imprints the mold on its surface into the polymer. This method aims to simplify the embossing machine, thereby reducing costs while at the same time increasing the throughput, when compared to traditional P2P embossing [50]. This approach also has some drawbacks; mainly that it still requires batch wise fabrication thereby limiting productivity. Imprinting thin film can be challenging and will require an additional sacrificial layer. Furthermore the time to heat and melt the polymer as well as fill all cavities of the mold with it, is very short - essentially all these steps can only happen in the short time that the contact line of the roller touches a given position on the film.
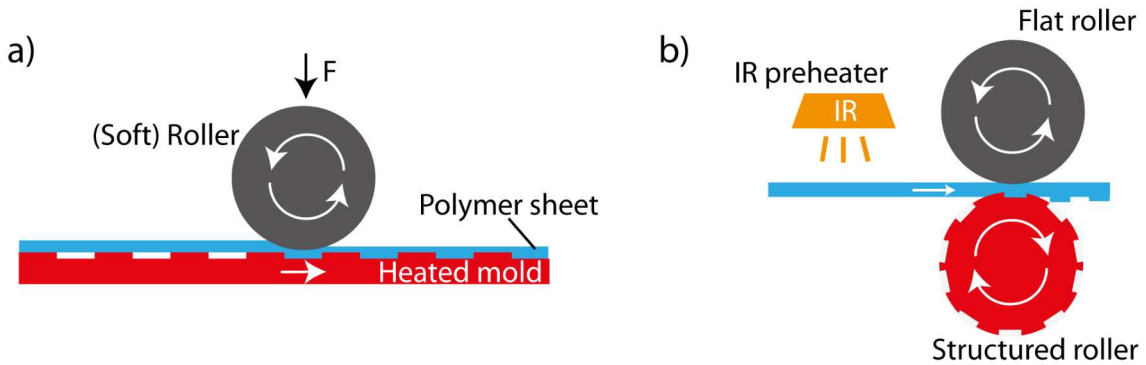
Figure 4.1: a) Roller to plate hot embossing. A structured roller is moved over a flat, temperature controlled plate, thereby structuring the polymer on the plate. **b)** R2R hot embossing. A polymer sheet is led through temperature controlled rollers that emboss a structure into the polymer. To aid with melting the material, sometimes pre-heaters are placed before the rollers.

An improvement over R2P embossing in terms of productivity is the R2R embossing process. In general this process uses two counter-rotating rollers that feed a film or sheet of polymer in between them (see Fig. 4.1b). One - or in some cases both rollers - are structured and heated well above T_M of the polymer. The surface of the polymer is molten and the structures on the rollers are embossed into the film. This process - while very efficient because of continuous production - has several drawbacks as well; the most significant of which is the limited amount of time for the actual embossing step. Since the roller has

an (idealized) line of contact with the polymer, the material has to be heated, molten and then pressed into the cavities of the mold all in the short amount of time that the roller is actually in contact with the polymer film. This makes the process very sensitive to variations of the feed speed of the rollers [51]. The roller must furthermore, due to the short contact time, be set to a very high temperature in order to melt a sufficiently thick layer of polymer. This leads - especially for relatively thick polymer sheets - to significant mechanical stress between the hot surface of the polymer film and the still cold core layers which can damage the structures when cooling or warp the entire part [52]. Furthermore, the short time to fill all cavities of the mold can lead to incomplete filling resulting in a significant height loss from mold to structure. Another drawback is the demolding of the structures. The temperature of the polymer film will increase, the longer it is in contact with the roller. This leads to the structures being demolded when they are the hottest and therefore softest - this can possibly lead to damages, higher shrinkage, loss of precision, higher roughness [146] and in general reduced quality of the imprint. Slowing the speed of the rollers or wrapping the film partly around a structured roller is therefore not helpful and might - if done too excessively - also led to the film melting over its entire cross-section causing it to rip and possibly stick to the rollers thereby jamming the machine and stopping the production. While some of theses drawbacks (partly melting the polymer film, demolding hot/soft structures) of R2R hot embossing are what actually enable the production of R2R nanofur by means of the hot pulling process described in the previous chapter, a process like this is certainly not ideal for imprinting precise geometrically defined structures.

A variant of R2R imprinting are so-called hybrid R2R imprinting processes where a film extrusion line is placed in front of the rollers and the imprinting is done directly into molten polymer. Relatively little work has been done so far using this approach [49]. Some of the drawbacks of R2R embossing outlined above can, at least in theory, be avoided or mitigated using such hybrid R2R embossing process. Therefore this approach was used and further developed in the course of this work, as outlined in the next Chapters.

A different alternative that also comes to mind when trying to mitigate the problems of "traditional" R2R embossing is UV imprinting. Great progress has been made in recent years in the implementation of precise roller UV imprinting [49]. In this process a thin layer of UV curable resist is applied to a substrate acting as a conveyor belt. The substrate is then led around a structured roller that embosses its features into the resin. A UV lamp cures the resist while it is still in contact with the roller. This approach has some advantages such as the minimal embossing forces as well as high precision due to fast curing resins and is today even used in niche commercial applications. However, it is not suited to applications where vast areas, sometimes in the order of square kilometers, are structured such as packaging, construction or coatings for solar panels. This is mainly due to the high price of UV curable resins, when compared to standard thermoplastic polymers. A simple comparison of the typical prices of widely used thermoplastic polymers and UV curing resins indicates that resins are more expensive by at least a factor of 30 to over 100, which is prohibitive for many commercial applications.

This prohibitive expense for UV roller embossing, as well as the aforementioned draw-backs of many R2R processes for thermoplastic polymers led us to implement a different approach that aims to eliminate these problems and complications of traditional R2R embossing. To achieve this we used classic film extrusion in conjunction with structured and cooled - as opposed to heated - rollers. The next chapters introduce our setup (see Fig. 4.2) and review the benefits of this approach. The influence of several important parameters are examined and the resulting imprints are compared to classic hot embossing.

4.2 The Direct Roll to Roll Hot Embossing Process

As stated above we implemented an improved R2R structuring process, that we call "Direct R2R hot embossing". "Direct" is a reference to the fact that we are imprinting directly into already molten polymer, as opposed to using solid sheets as a raw material. This gives us several advantages. First, we do not have to melt the polymer when in contact with the roller. Second, this process has - due to an adapted feed through of the material - a much longer mold filling time compared to traditional R2R embossing processes. Third, we demold the structures at or even below the glass transition temperature of the polymer, leading to more precise structures and less possible damage.

Figure 4.2 gives an schematic overview over the setup used. It consists of a lab-scale single screw extrusion machine (Collin E20E) with a screw diameter of 20 mm, a barrel length of 500 mm and seven heating zones. The maximum throughput is about 10 kg/h, depending on the material used. The melt temperature can be adjusted up to 400 °C. The polymer is extruded through a heated sheet nozzle (Collin BSD 120) with a width of up to 12 cm and a gap size between 0.2 mm and 2 mm. After extrusion the polymer film is led through a calender (Collin CR 72/72/72-200 T). The main two rollers that do the actual imprinting and smoothing of the polymer film are temperature controlled in a range of 20 °C to 120 °C; the lower chill roller is kept at 6 °C. The conveying speed of the rollers can be adjusted independently from the feed rate of the extrusion machine. While travelling through the calender the polymer film is wrapped around the lower main roller for about half a revolution. This is the roller that is structured for all further experiments. The methods of structuring the roller will be discussed in the next section. The pneumatic cylinders pushing the rollers together and thus excerting the embossing force were upgraded from the factory ones so that they can now excert a combined force of 5300 N. After the embossing step the film was wrapped around a chill roller for half a revolution with the non structured side facing the roller and then led to the windup unit of the calender. Here the tension of the film can be adjusted by setting the torque of the windup motor.

4.3 Structuring of the Rollers

The major difficulty in roller embossing is the structuring of the rollers themselves. In our case there are three options available for structuring the rollers: direct structuring, clamped shims and welded shims. Direct structuring is done by patterning on the surface
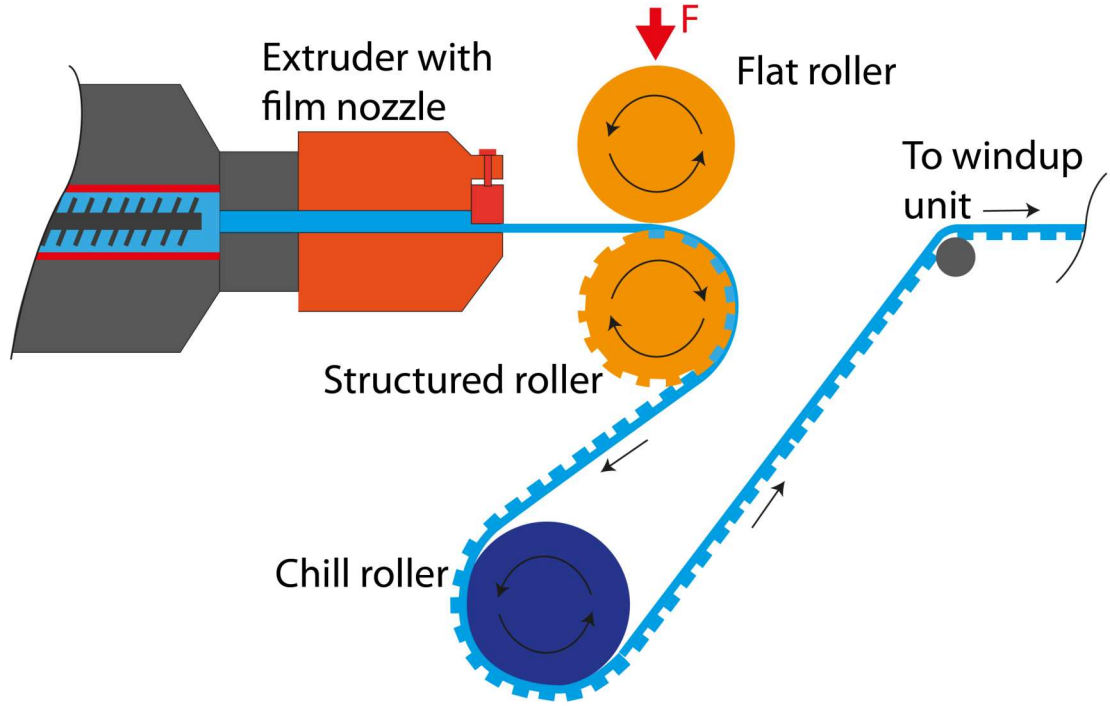
Figure 4.2: Setup used for R2R imprinting. The light blue parts are the polymer melt respectively the solidified polymer film. The polymer melt is extruded as a thin film onto the rollers, where the structure is embossed and it is cooled down. By the time the structures are demolded, the polymer has solidified. The solid but still hot polymer film is wrapped around a chill roller where it is cooled to room temperature and then led to a windup unit. If the imprinted structures were very sensitive, the polymer film could also be cut in regular intervals in order to avoid breaking the structures while winding the polymer film up.

of the rollers directly. This leads to completely seamless patterns on the roller which allows an "endlessly" long film to be patterned without any interruptions of the structures on the surface. In the case of relatively coarse applications around 10 μm direct structuring can be done by precision milling or EDM [147], for applications requiring smaller features interference lithography as well as several other lithography techniques [147, 148, 149] exist. In general one could say that all these techniques are quite specific and require a lot of expertise to operate and are therefore not widely adopted - the widely available lithography systems usually require flat surfaces. Furthermore patterning directly in nickel, stainless steel or other materials suitable for manufacturing durable molds and rollers by means of lithography is - while possible [150] - still quite challenging. For these reasons direct structuring of rollers by lithography was not employed.

The other two options require so-called shims - thin, flat sheets that contain the negative of structures to be imprinted. These can be manufactured using almost all combinations of techniques that are available for flat substrates. After manufacturing the positive structures on a substrate, a conductive layer is applied and an electroplating step is performed. Here,

49

about 150 μm to 300 μm of nickel is deposited. It is important that either the nickel can be separated mechanically from the substrate or the substrate material can be chemically dissolved [91, 151]. The result is a thin nickel sheet that can now be bent around the roller and be attached. If multiple shims are needed, a first, thicker, master shim can be produced in this way and several copies of that shim can be made by means of electroplating nickel on nickel.

The development of the attachment mechanisms was conducted together with Marc Rossrucker in the framework of his Master's thesis [152]. Attaching the shims to the rollers can be done via a clamping mechanism (see Fig. 4.3) using a special clamping roller on the calender. The roller has a groove about 15 mm deep that can hold a clamping bar. This clamping bar can be expanded by tightening grub screws that press the ends of the shim against the sidewalls of the groove. The shim is wrapped around the roller so that the ends rest on the sidewalls of the groove, where the clamping bar can grab and hold them in place. The shims have to be quite thin - in our case about 100 μm - to be able to be wrapped around the tight radii of the groove. To allow for a smooth rolling motion of the rollers against each other a cover strip is added on top of the clamping bar. This method of attaching shims enables the removal and replacement of the shim from the roller in a very easy and quick fashion because a shim can be replaced without the need to dismantle the calender to change out the roller. This method is therefore suitable if, for example, multiple designs of shims are to be tested in a quick fashion for prototyping.
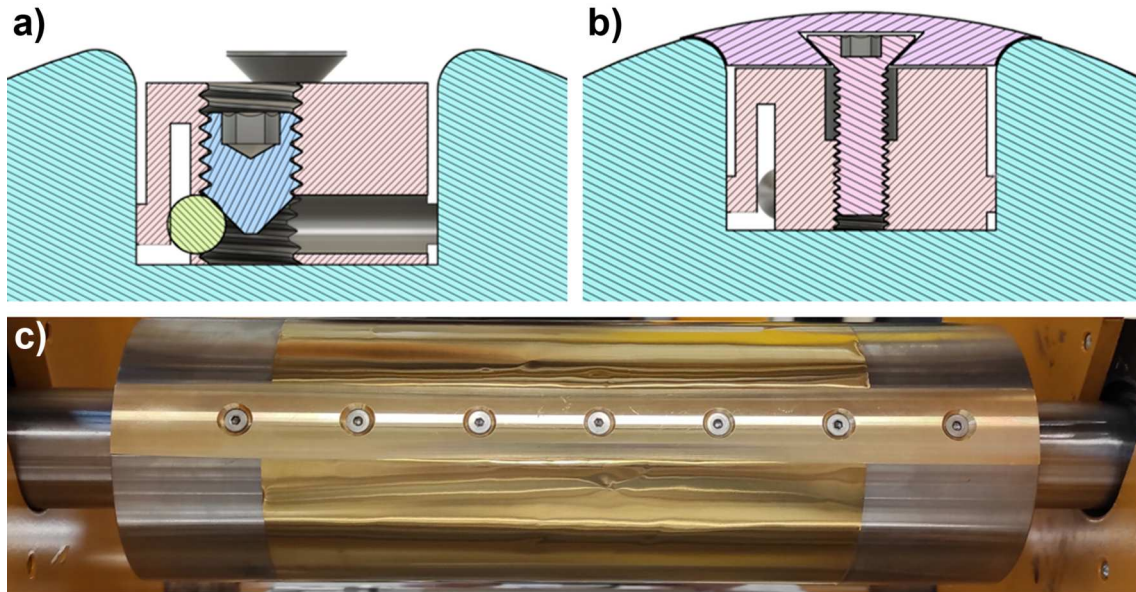
Figure 4.3: Setup of the clamping mechanism. **a)** Section through the clamping mechanism. The shim is not depicted - it would wrap around the roller as well as the two radii at the top. The grub screw presses the bearing ball against the clamping lip on the left thereby attaching the shim firmly to the walls of the grove in the roller. **b)** A brass cover strip is added to allow for smooth rolling motion. The seam between imprints is equal to the width of this cover strip. **c)** The clamping roller with a thin brass shim attached.

The third method for attaching the shims to the roller is spot welding. The shim is welded onto a hollow steel cylinder using an industrial spot welding gun (see Fig. 4.4). The weld spots are set at one edge of the shim; it is then wrapped around the cylinder and the other edge is spot welded into place. The seam created this way is much smaller than the one of the clamping roller. There are no welds necessary around the circumference of the shim.
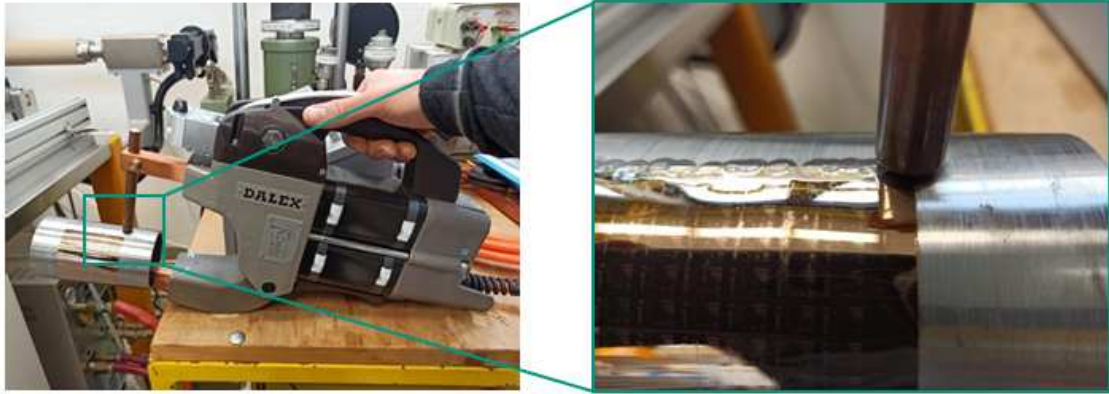
Figure 4.4: The spot welding gun used for attaching nickel shims to hollow steel cylinders. A series of weld spots is placed on one end of the shim; it is then wrapped around the cylinder and the other edge is welded on. The inevitable seam is about 5-10 mm wide, which is fine for lab applications and might also be for various industrial uses.

The hollow cylinder with the shim welded on can then be assembled onto an expanding roller core on the calender (see Fig. 4.5). This roller core was first manufactured from stainless steel, which lead to problems caused by the material's insufficient heat conductivity. Therefore another roller was manufactured from a high strength 7075 aluminium alloy. Furthermore graphite film was introduced in between the parts of the roller core as well as in between the roller and the steel cylinder that the shim was welded to in order to increase heat conductivity. Welding the shims is a more durable method of attaching them to the rollers that also minimizes the seam that comes with using shims instead of direct structuring. More precise welding methods are available that would minimize the seam to under 100 μm [153]; however this is not necessary for many applications, as frequently the film is cut in smaller pieces for further processing anyhow, e.g. for microfluidic chips, coatings for solar panels and many more. Therefore the spot welding method was chosen for these experiments; mainly because it is quick and easy and is, on the other hand, sufficient for most applications.
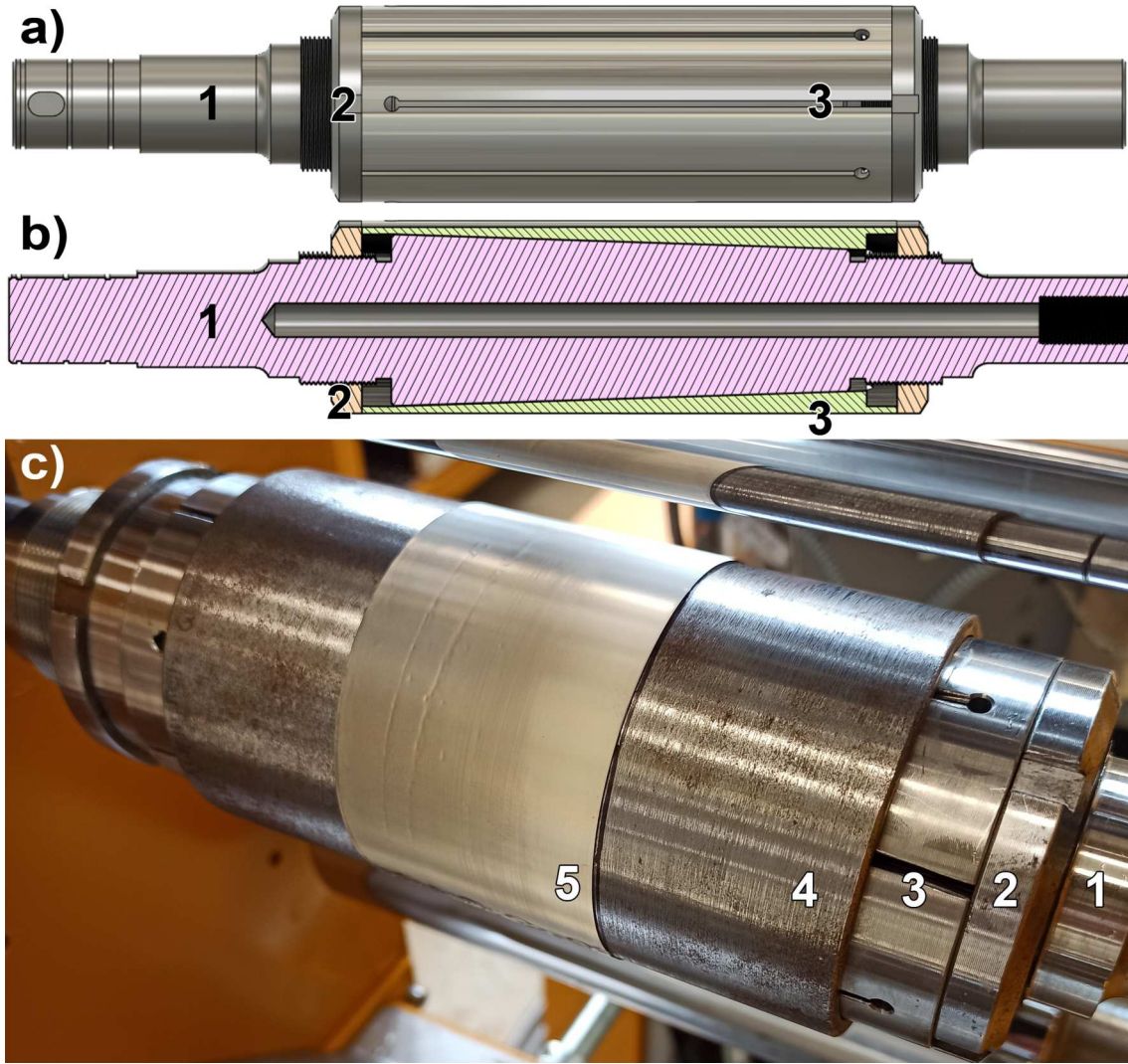
Figure 4.5: a) Schematic of the expanding roller for attaching welded shims to a roller. **b)** Section through the roller. **c)** The expanding roller with a shim attached. The components are: 1) Conical roller core; 2) Tightening nut; 3) Slotted sleeve with conical inside surface; 4) Hollow steel cylinder; 5) Shim welded to steel cylinder.

4.4 Stitching of Master Structures to Fabricate Large Molds

A significant challenge in roller embossing is the fabrication of sufficiently large molds. Since most tools used in microstructure fabrication are built for flat substrates (mainly glass and silicon wafers) the shim-approach described in the previous section seems to be the most convenient route for most applications. Unfortunately, many machines used in a lab context are capable of processing wafers of only 6 " (152.4 cm) in diameter, which, even with a shim width of just 50 mm, only yields a 143.9 mm long shim, which is too short to wrap around the rollers presented in the previous section (diameter 72 mm, circumference 226.19 mm). Considering that the rollers used in this study are relatively small, especially when compared to roller extrusion machines used in industrial contexts and the fact that

the largest wafers used for commercial applications are 450 mm in diameter, the need for a fabrication method using some kind of stitching of individual molds can easily be identified. While some options already exist, such as welding multiple nickel shims [153] or several variations of step and repeat processes [154], the approach developed in this study uses a minimal number of tools, is therefore highly cost effective and can be implemented in most labs rather easily. Furthermore the seams and especially the vertical displacements of the parts, e.g. the "step" created in between the parts, is smaller than the seams created by welding.

The stitching process that was implemented is based on replication of a single master structure or master "cell" by means of UV imprinting using PMMA resin or traditional hot embossing. A master mold, preferably made of nickel or another durable material, has to be fabricated. This can be accomplished by using traditional tools for structuring wafers and resins such as spincoating, sputtering, lithography or etching and afterwards forming the master mold from these structures by electroplating. For better flatness and rigidity this master mold is attached to a steel plate via "hot glueing" in a hot embossing machine. For this procedure, a thin (0.3 mm) sheet of PEEK is placed between the backside of the mold and the steel plate it is to be attached to. To protect the nickel master mold from being scratched by the flat steel counter plate of the hot embossing machine, a piece of aluminium foil is placed on top of the master, separating it from the steel plate. The PEEK is melted while the hot embossing machine is closed. The mold is pressed firmly into the molten polymer with its backside. After cooling the mold is attached to the steel plate in a very similar fashion as with hot melt glue. Since the melting point of PEEK is much higher than most other polymers this form of attachment can be used for hot embossing as well as UV imprinting. In our case this gluing process was done by using a hot embossing machine, but this can in principle also be achieved with a hot plate and flat weights; also welding or soldering the master mold to the steel plate might be viable options.

The mold is then used for a simple UV imprinting process using a UV curable PMMA resin (Harzspezialisten SK resin 1390). The resin is poured over the mold forming a 3 mm thick layer and then cured under a UV lamp until it is hardened. Demolding is done manually using a razor blade to pry on the excess PMMA to demold the part without touching the structured surface. This process is repeated until a sufficient number of PMMA replicas have been manufactured. This replication step can also be achieved via hot embossing. If done so, it is important to consider that laser cutting (the next step) hot embossed PMMA leads to burrs on the edges. This is also true for many other polymers. Therefore it is advised to choose another method of cutting (waterjet / wafer dicing) if hot embossing is to be used as replication technique.
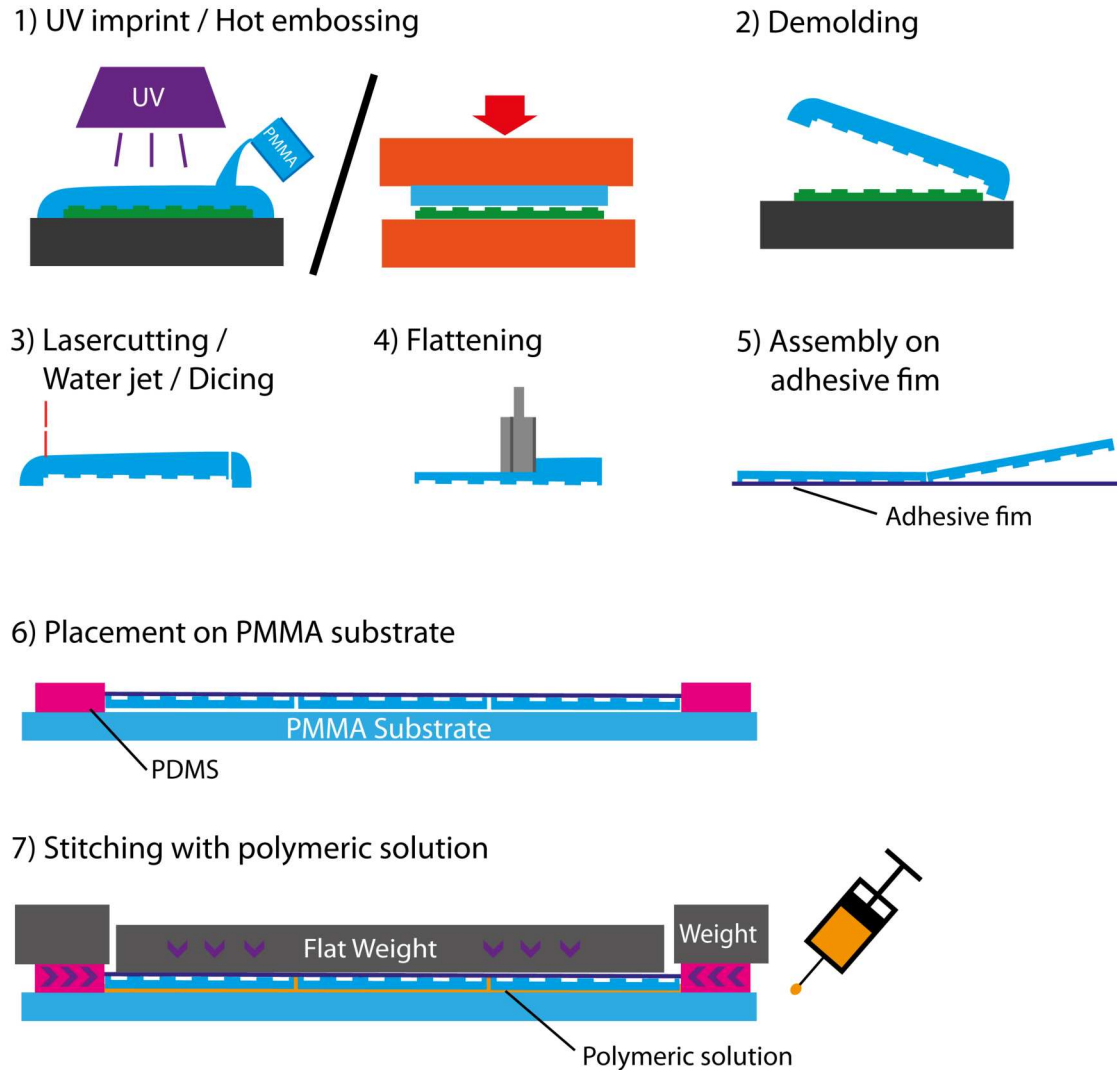
Figure 4.6: Schematic of the stitching process used to manufacture large molds. First the master structure that is to be replicated and stitched must be attached to a steel backing plate. Afterwards the master structure is replicated several times - this step can either be done via UV imprint or hot embossing (1). After demolding (2), the edges are cut off using a laser cutter/water jet or wafer dicer (3). Then the backsides of the pieces are milled flat and to an equal thickness using a precision mill (4). For stitching the individual pieces are assembled on an adhesion film (Ulton systems, Silicone-Free) with the structured side facing the film (5). The pieces are then turned and placed on the polymer substrate. PDMS blocks with weights apply a clamping force that closes the gaps between the individual pieces (6); a flat weight on top ensures that all pieces are stitched together with minimal height offset. A solution of PMMA in ethylacetate is applied to the sides of the pieces; capillary action transports the the solution underneath and in between the pieces (7).

The excess PMMA is then cut off using a laser cutter (Universal Laser Systems VLS3.75). Since cutting with lasers leaves sloped sidewalls, the structured side of the replicas has to be placed facing away from the cuthead to minimize gap size between the parts later on.

After ensuring that all parts have precise, rectangular and straight edges, the pieces are placed on a precision flycutter (Reichert-Jung Polycut E), the structured side facing down, so that the backsides of the pieces can be flattened. All parts are milled down to an equal thickness of about 1.5 mm. The accuracy of the flycutter used is 0.5 μm; on less precise machines the imprecision could be mitigated by milling all pieces at once in a single pass, permitted the flycutter was wide enough. After these preparations the individual pieces are ready for the actual stitching process, which is shown as a schematic in Fig. 4.6 and with photographic images in Fig. 4.7.
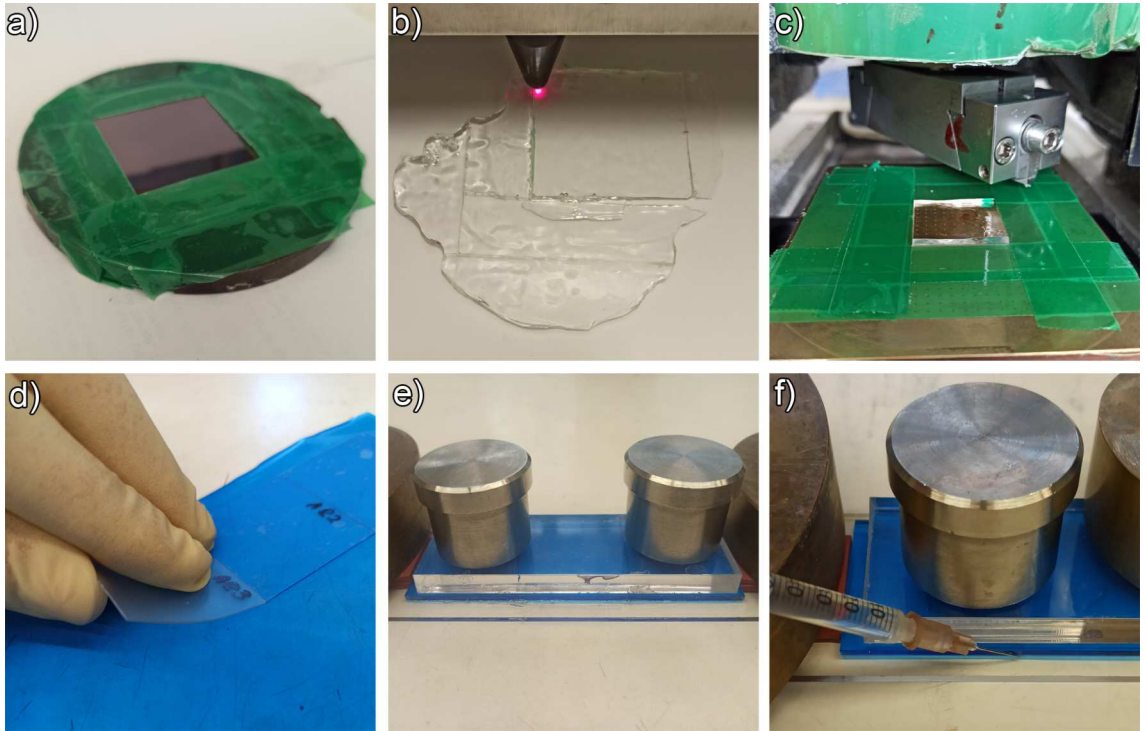
Figure 4.7: Images of the stitching process. The steps are the same as illustrated in the schematic above. **a)** PMMA replica produced via UV imprinting still in the mold. **b)** Laser cutting to achieve straight edges. Water jet cutting or cutting with a wafer dicer would be viable options as well. **c)** Flattening the backside of the pieces using a precision flycutter. **d)** assembling the parts on a piece of adhesion film (Ultron systems, Silicone-Free). **e)** The parts are placed on a PMMA substrate and clamped down by weights on a flat plate. PDMS blocks apply slight pressure from the sides, forcing the gaps to shut. **f)** A polymeric solution (PMMA in ethylacetate) is sucked into all gaps by capillary action.

Stitching two dimensional arrays of pieces, e.g. a 3 x 3 array, is done in a two step operation. First three 3 x 1 arrays are stitched and, after cutting their edges to ensure they are straight, the three 3 x 1 arrays are stitched together to the full 3 x 3 array. Flat PMMA plates with a thickness of 2 mm were used as substrates. The individual pieces are placed facing down on an adhesive film. While placing the pieces the film was slightly stretched and the pieces were pushed together by hand, minimizing the gap in between the individual parts. The parts are now held together by the adhesive film on the structured side. After flipping the parts, they are placed on the PMMA substrate. Two blocks of crosslinked PDMS (Wacker Elastosil 6010) are placed on the top and bottom edge of the part. When a force is applied to these blocks by placing a weight on top, they expand, thereby pushing the parts that are to be stitched together, ensuring minimal gaps between the parts. To minimize the vertical displacement of the parts relative to each other, a flat plate and some weights are placed on top of the parts, pushing them down onto the substrate. To stitch the parts together and fill the microscopic gaps in between them, a polymeric solution of PMMA and ethyl acetate is used, which is produced by simply dissolving PMMA granulate (Lucite Diakon CLG356) in ethyl acetate. The viscosity of the solution must be fairly low, almost comparable to water. Drops of the solution are then placed at the side edges of the parts to be stitched. Since the gap between the substrate and the parts, as well as the gaps between the individual parts, are very narrow, the capillary effect is strong enough to suck the polymeric solution under and into the gaps, completely filling them. The adhesive film prevents overfilling of the gaps, which can happen when polymeric solution flowing from opposite sides collides in a gap between the parts. After the ethyl acetate has evaporated, the weights and PDMS blocks can be taken off and the individual pieces are now stitched together to form one solid PMMA part. The adhesive film can be peeled off without any residue, as it is designed to do. The edges of the part can then be straightened using laser-cutting and the process can then be repeated until the full array is stitched. This stitching process was also carried out using ABS and an ABS-Acetone solution.

Afterwards the stitched array of PMMA master structures is coated with 7 nm chromium and 50 nm gold by sputtering. The sample is then placed in an electroplating setup, where a nickel layer of 500 μm is applied. This nickel shim can then be removed from the master mechanically, aided by ethyl acetate as solvent if necessary. This nickel shim can then be wrapped around a roller and welded in place as described in the previous chapters. Figure 4.8 shows the gap region in between the stitched part on a finished nickel shim. The gap region is usually between 30 to 50 μm in width while the vertical displacement is below 30 μm and often times even in the single digit μm range. Unfortunately the nickel shim shows a bulge at the seam with a height of 60 μm in this case. On average the height of the bulge is around 30 μm. It results from the solvent evaporating from the polymer solution used for the stitching process. This leads to shrinkage and therefore a depression at the seam of the stitched polymer pieces. When the polymer master is then electroplated this depression results in a bulge of the produced nickel shim.
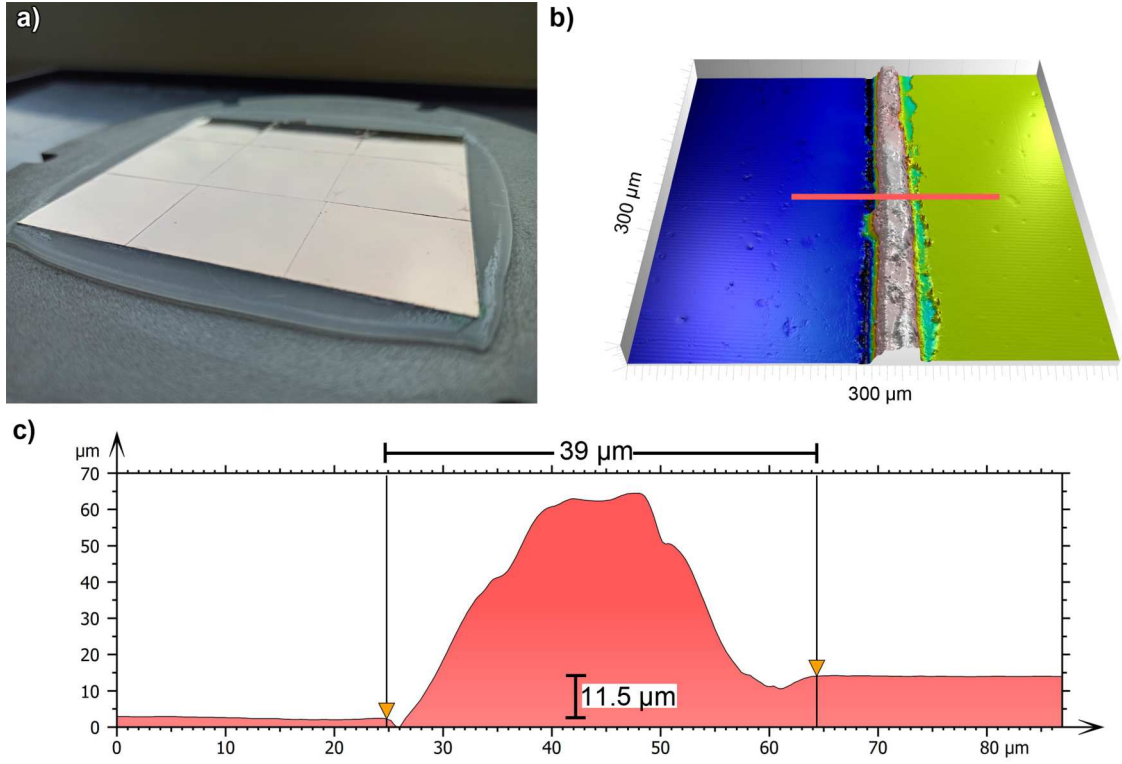
Figure 4.8: Gap region of the stitched pieces. **a)** Photographic image of a stitched nickel shim. This shim is already attached to a steel plate in order to be used as a plate-to-plate hot embossing mold. **b)** 3D rendering of a CSM image of a stitch region of the nickel shim. The red line is where the profile was taken from. **c)** Profile of the stitch. The width of the stitch is usually between 30 to 50 μm. The vertical displacement of the stitched parts never exceeded 30 μm and is often in the single digit μm range.

It is obvious that this stitching process can be improved in a number of ways. Better UV imprinting step can aid in achieving a better structure quality. UV nano imprinting machines, often times based on UV wafer bonding machines, are commercially available [155], although often times demolding has to be done manually. Nevertheless, the added pressure during curing might aid in forming better structure quality. Hot embossing is a viable option if another method than laser cutting is available. While laser cutting can provide clean and straight edges, it fails on many hot embossed materials, as many polymers (e.g. PP, PC, COC, etc.) form burrs, ridges or rounded edges when lasercutting. PMMA is one of the few polymers that can be cut with clean edges by lasercutting. Water jet cutting or wafer dicing might be good alternatives for materials that are difficult to cut with lasers. The alignment of the structures could not be precisely controlled with the lasercutter available - many wafer dicing machines provide at least some kind of alignment tool. Since it was not relevant for the sandfish inspired surfaces that were to be stitched and imprinted (see Chapter 5), this was not a priority in our case. While the manual stitching, using weights and PDMS blocks to apply lateral clamping force, led to surprisingly accurate results, a specific tool applying pressure from the sides as well as from the top might

further minimize some of the alignment errors. Furthermore, due to logistical reasons, not the whole process was not carried out in a cleanroom environment. Even though the samples were thoroughly cleaned with pressurized air when entering a cleanroom, some contamination may be found on the samples. Lastly using another polymer than PMMA might improve the electroforming process significantly, since PMMA is notoriously difficult to metallize reliably [156, 157]. While these improvements to the process would have led to even more precise stitching, it was demonstrated that relatively well stitched molds for use in roll-to-roll applications can be obtained, even with this very simple and cost effective setup.

4.5 Parameters for R2R Imprinting

As simple as the concept of the direct roll-to-roll hot embossing process might seem; the parameter range is quite large and extensive trials were necessary to find sets of parameters that lead to good quality film as well as satisfactory micro- and nano-imprints. For some parameters there seems to be a trade-off between the quality of the overall film (dents, wrinkles, clarity, ect.) and the quality of the microstructures (edge rounding, height loss). In general film extrusion processes - even with flat, unstructured film - are very delicate and require precise control of process parameters [51].

The set of examined parameters can be divided into two parts: One for the extrusion part of the process, where reference values can be found in literature, and parameters for the imprinting process. The extrusion parameters are mainly the temperature values for the individual heating zones of the extrusion machine and the screw speed. For temperature profile, we chose a simple linear profile with temperature values close to the polymer manufacturers recommendations. The screw speed was varied to fit the needs of the imprinting process. Melt temperature, pressure and viscosity at the sheet nozzle are set indirectly by the temperature profile in the extruders barrel and the screw speed.

The imprinting parameters included sheet nozzle gap size, the gap between nozzle and roller, roller pressure and temperature, conveying speed and film tension. Adding up all parameters, there are 15 individual parameters each of which can be set in a wide range. A full factorial design of experiment is therefore unpractical; hence a fractional factorial design of experiments approach was chosen. It can be noted that, while these experiments were conducted using COC, smaller experimental runs with PMMA showed that the general trends presented in this section also apply there.

4.5.1 Experimental Setup for Roller Hot Embossing

To gain a general understanding of the extrusion process, flat polymer film without any structuring was produced at first. This led to five parameters that seem to have the most influence on the quality of the film. The polymer (Topas 8007S-04), the gap between nozzle and roller (about 1.5 cm) as well as the nozzle gap were kept constant during the entire experimental series. Since the nozzle gap, and especially its uniformity, has great influence on the macroscopic film quality, great care was taken to set it to exactly 0.3 mm and

then adjust it slightly on several points along its width until a uniform film thickness was achieved. The windup unit's torque and therefore the film tension had negligible influence on film quality and was therefore set in a way that led the entire process and especially the windup to run smoothly. The parameters that were varied were therefore:

- Melt temperature

- Screw speed / feed rate

- Roller speed

- Roller temperature

- Roller pressure

Each of the parameters was varied on five levels. A full factorial experiment would hence need $5^5 = 3125$ individual experimental runs, which is unfeasible. Therefore a fractional factorial design based on the Taguchi method was chosen. The design of experiments consisted of $5^{5-3} = 25$ individual runs. References containing the orthogonal arrays needed for creating this fractional factorial experimental design can be found in literature [158, 159]. In order to derive a relation between, e.g., roller speed and structure height, the structure height of all runs were the roller speed was set to level one are averaged, then all runs were the roller speed was set at level two are averaged, etc. This method results in a graph that shows a general trend of the influence of the roller speed on structure height. On the one hand, this method of experimental designs leads to a manageable number of experimental runs, on the other hand main interactions of several parameters are mixed among each other as well as with secondary and tertiary interactions and can not necessarily be separated from each other. This limited accuracy was deemed acceptable in this first step, since it was intended to later conduct further one by one experiments for selected factors. The results are calculated by averaging all runs, where the experimental parameter was set on one level. To calculate, for example, the relation of film thickness and roller speed, the film thickness of all runs where the roller speed was set at level one (2 m/min) are averaged. The same was done for all runs where the roller speed was set at level two (3 m/min), etc. Finally the results can be plotted in a graph with the roller speed on one axis and its effect on film thickness on the other (see Fig. 4.11). For these fractional factorial experiments, the five parameters stated above were varied on five levels. The orthogonal array used for the design of experiments as well as the actual parameter values for each level can be found in tables 7.1 and 7.2 in the appendix.

To be able to evaluate the quality of the imprints and be able to actually measure the results quantitatively, a set of test structures was produced. The layout consists of a cell of about 7 x 5 mm^2 that is repeated multiple times over the whole shim to be able to compare multiple regions on the shim. The layout of the cell shown in Fig. 4.9. It features several sets of lines and pillars with a minimal width and distance of 2.5 μm up to a width of 20 μm with a distance of 50 μm. Several other structures can be found such as several arrays of holes and pillars in various sizes, checkerboard patterns, lenses, logos and Siemens stars.

The test structures were produced by direct laser writing (Heidelberg Instruments DLW66 fs) in AZ photo resist (AZ 1505) on a 6" silicon wafer. A thin layer of chromium (7 nm) and gold (50 nm) was then sputtered on the structures before a 150 μm thick layer of nickel was applied by electroplating. The wafer and the AZ resist were then etched leaving the nickel shim behind that is then mounted on the rollers as described in the previous section. Due to this fabrication process all structures have the same height of 1.6 μm. Unfortunately some small defects can be found on the shim; in some cells the smallest pillars are not completely formed, the center of the Siemens stars has not been perfectly manufactured in some cells and the sidewalls are not perfectly vertical, but have a very slight slope, which is something that cannot be avoided using the existing manufacturing techniques. Therefore multiple measurements on different parts of the shim have been taken for each imprinted sample, to ensure getting a complete picture.
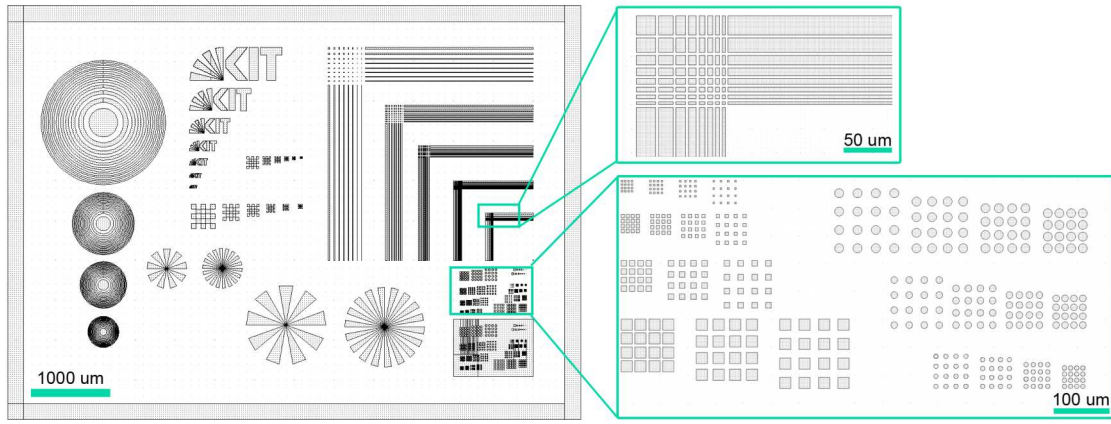

Figure 4.9: The layout of the test structures used for the optimization of the R2R process.

4.5.2 Results of Fractional Factorial Imprinting Experiments

The experiments were conducted together with Tina Schindelhauer in the framework of her Bachelors thesis [160]. The evaluation of the fractional factorial experiments was done using one of the large checkerboard patterns (see Fig. 4.10). This pattern is about 300 x 300 μm^2, while the individual fields of the pattern are ideally about 60 x 60 μm^2. The width and the ratio of "high" to "low" fields of the checkerboard was measured ($R = W_{Low}/W_{High}$) to check for the slope of the sidewalls and edge rounding. Vertical sidewalls would correspond to a ratio of $R = 1$. Since fabricating vertical sidewalls is, in general, challenging, the mold unfortunately has slightly sloped sidewalls; the ratio is about $R = 1.05$. Furthermore the overall height of the structures was measured in order to quantify weather there is a height loss from the master structure to the imprint.

Some of the parameter combinations led to defects in the film such as wrinkles, dents, gels or variations in film thickness. For these samples a spot without defects was chosen for the measurements and the defects were marked down as comments. Unfortunately statistical design of experiments needs qualitative, measured values to be able to compute
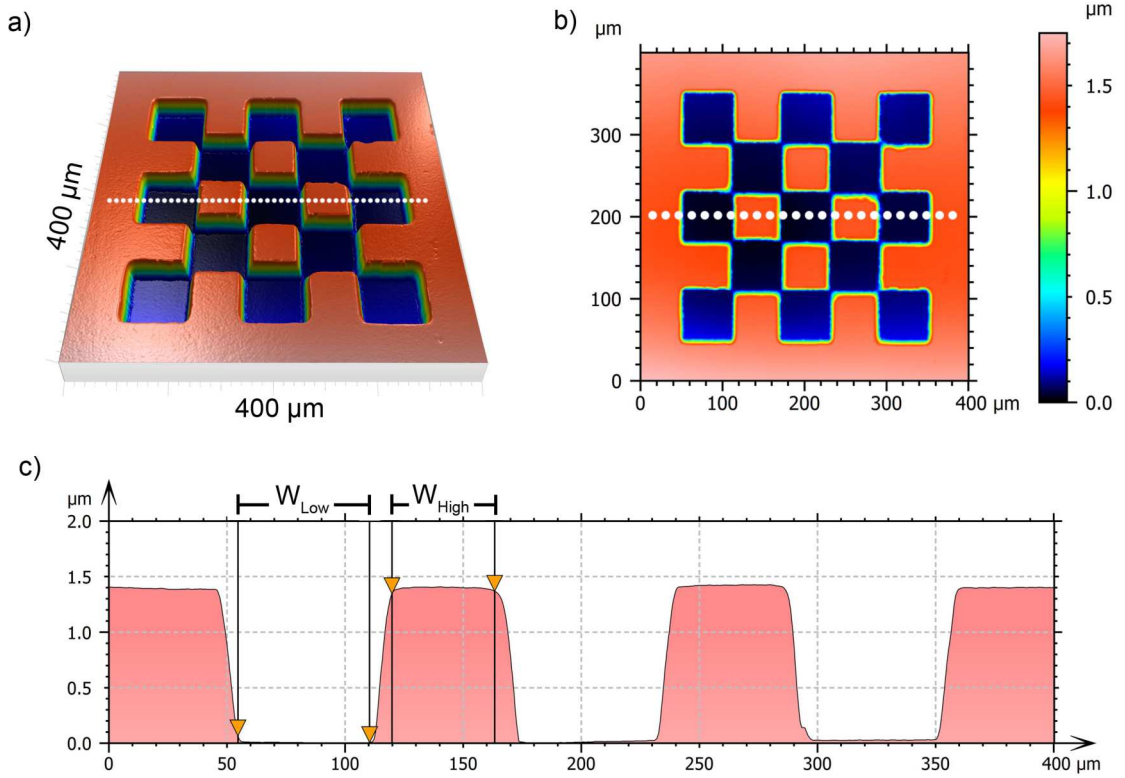
Figure 4.10: a) Exemplary 3d view of one of the analyzed checkerboard patterns. **b)** Topography view of the checkerboard pattern. The white dotted line shows where the profile was extracted from. **c)** Profile of the checkerboard pattern. The ratio of the width of the high to the low fields is a measure for edge rounding as well as sloped sidewalls.

results and no objective way was found to include these defects in the evaluation. Therefore it is possible that the "best" parameter combination for a given target, e.g. "minimal edge rounding", might on the other hand lead to large scale defects that make the overall film unusable. Nevertheless these experiments can help identify sensible parameter ranges for more detailed experiments later on and also aid in developing a "feeling" for the process and the machinery involved.

The following graphics show the effect that different parameters have on the quality of the imprints. The influence of the roller speed on film thickness, which is plotted in Fig. 4.11, is quite unremarkable. The higher the roller speed the thinner the film, which is to be expected since this is one of the ways in which film thickness is controlled in commercial cast film production. This confirms that the statistical analysis method works well. For the other two parameters - checkerboard aspect ratio and structure height - the roller speed has no significant influence.

The opposite is true for the roller temperature and embossing force (see Fig. 4.12). Here - both increased temperature as well as increased embossing force - lead to the checkerboard aspect ratio to decrease and approach $R = 1$ while the structure height increases to the full height of 1.6 μm. For melt temperature and screw speed the results are not as obvious (see
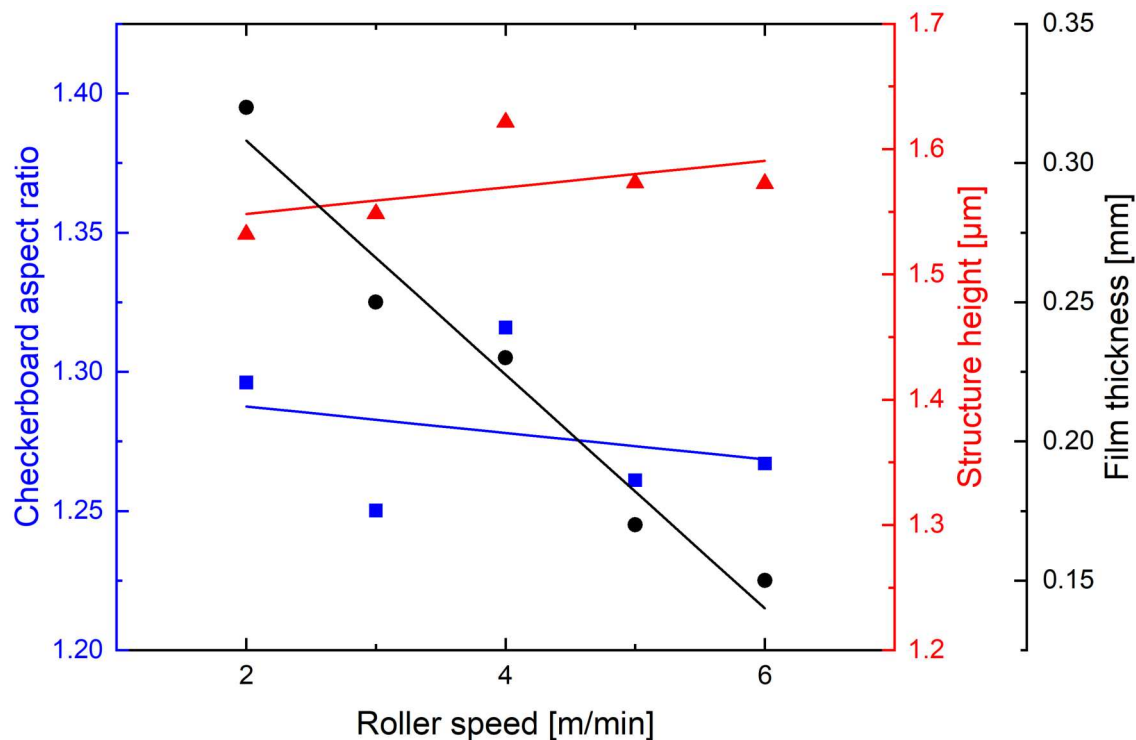
Figure 4.11: Influence of Roller speed on film thickness, structure height and edge rounding. Roller speed does not affect step height (▲) and the checkerboards aspect ratio (■). Film thickness (●) decreases with an increase in roller speed, which is to be expected as adjusting the roller speed is used in commercial film production to set the film thickness.

Fig. 4.13. The checkerboard aspect ratio decreases with increasing melt temperature up to a temperature of 245 °C, for 250 °C the aspect ratio is much higher and therefore worse. The structure height has an outlier at 230 °C and seems to increase slightly with increasing melt temperature. For the screw speed the aspect ratio varies significantly, while the structure height is worst at the middle value of 150 min^{-1} while it is good for the slowest and fastest value. This great variability might indicate that the screw speed is of low importance for structure quality, it has nevertheless a great influence on the macroscopic film quality. If the screw speed is set too low, not enough material is provided and deep grooves in the film along the longitudinal direction are formed. This might also, in part, be the result of contamination, defects or subpar polymer flow in the sheet nozzle. If the screw speed is set too high, the material eventually folds itself and consequently forms large wrinkles in the film. It was therefore decided to choose the screw speed in a way that minimizes macroscopic defects in the film in the following experiments by increasing the screw speed to the point that the longitudinal grooves just disappeared.
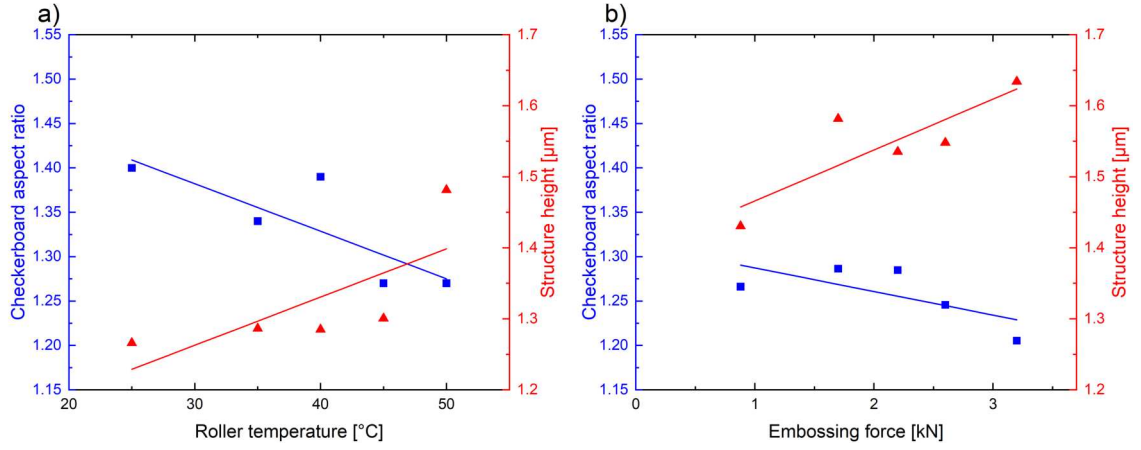
Figure 4.12: a) Influence of the roller temperature on edge rounding and structure height. An increase in roller temperature leads to an increase in structure height (▲), although the limit value of 1.6 μm is not reached. Furthermore the checkerboard's aspect ratio (■) decreases and therefore approaches the value one with increasing roller temperature, indicating less rounded edges. **b)** Influence of the embossing force on edge rounding and structure height. An increase of embossing force leads to an increase in structure height (▲), up to the optimum value of 1.6 μm. Furthermore the checkerboard's aspect ratio (■) moves closer to the value of one with increasing pressure, indicating sharper edges.
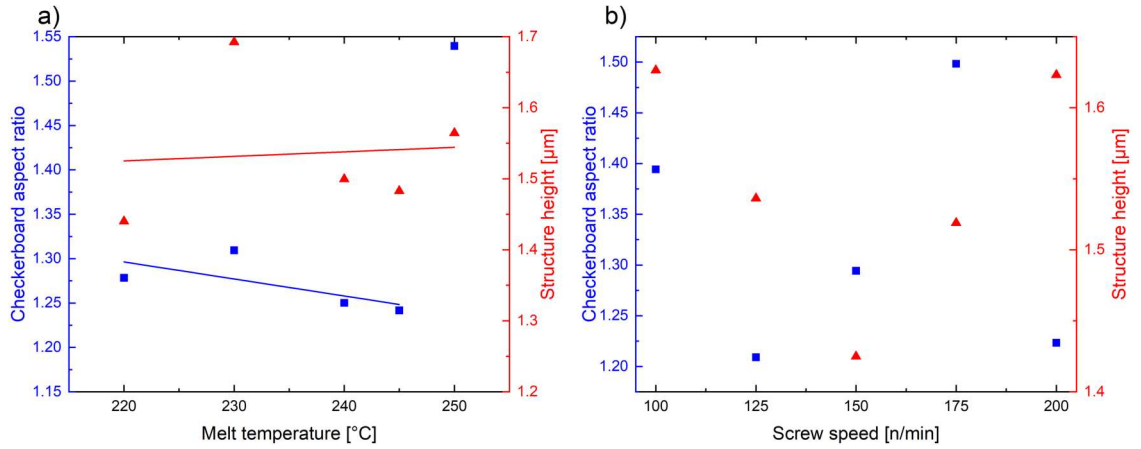
Figure 4.13: a) Influence of the melt temperature on edge rounding and structure height. An increase in temperature leads to an slight increase in structure height (▲). One outlier can be found at 230 °C. Furthermore the checkerboard's aspect ratio (■) moves closer to one with increasing melt temperature, up to 240 °C. **b)** The calculated values for the screw speed scatter significantly. Therefore the influence of screw speed on structure quality is not yet fully understood. The screw speed has great influence on the macroscopic film quality. If it is set too low not enough material exits the nozzle, which leads to sink marks along the film. If screw speed is set excessively high, the material will wrinkle. Therefore it was decided to set it in a way that minimizes these macroscopic defects.

4.5.3 Results of Selected Full Factorial Imprinting Experiments

The fractional factorial experiments allowed identification of parameter ranges that might be interesting for closer inspection. These experiments were carried out one parameter at a time while the other parameters were kept constant.

Embossing Force The pressure provided to the pneumatic cylinders forcing the rollers together was varied from 1 to 4 bar, which, given a cylinder diameter of 75 mm and two cylinders, is 880 N to 3500 N of embossing force. Given an approximate film width of 8 cm, this leads to a theoretical maximum line load of 44 kN/m. While higher pressures and therefore embossing forces would be possible with this machine, this leads to a stop of the rotation of the rollers at the weld spots of the shim due to the uneven surface and the insufficient torque of the driving motors. While a faster roller speed leads to higher maximum embossing force at which the machine stops, 4 bar (3500 N) was identified as the practical limit in this case. All parameters other than the embossing force were kept constant - Melt temperature: 250 °C, screw speed: 150 min^{-1}, roller temperature: 40 °C and roller speed: 4 m/min. Figure 4.14 shows measurements with the confocal scanning microscope of the produced structures at various pressure settings. Hole-like structures, *i.e.*, structures that are below the surrounding film are imprinted more easily than pillar-type structures. The larger pillars are formed very well and to the maximum height of 1.6 μm even at lower embossing forces, although the edge rounding is quite significant. The small structures are imprinted insufficiently or not at all. An increase of embossing force leads to smaller structures being imprinted and the more coarse structures to have less rounded edges. This correlation was also reported in literature [112]. It is interesting to note that the embossing force has only a negligible influence on film thickness, the overall flatness of the film, however, is better at higher embossing forces.

Melt temperature The temperature profile in the extrusion machine can be essential for a good quality product. The machine used for these experiments has seven individual temperature zones. The inlet zone is kept at 40 °C to preheat the polymer pellets without sticking them together and clogging the inlet. For the remaining zones a linear increase in temperature from 150 °C to the maximum temperature at the nozzle is chosen. The temperature in the nozzle zone is set around 20 °C higher than the intended melt temperature. The processing temperature of the COC used (Topas 8007S-04) is given as 230 °C to 240 °C by the manufacturer. Therefore we varied the melt temperature from 230 °C to 250 °C in increments of 5 °C. While higher temperatures are possible for a short time without causing immediate thermal degradation, the very low viscosity of the polymer melt makes it impossible to feed the material through the machine at startup. Lower temperatures lead to streaks, gels and possibly parts of unmelted material in the final film. The other parameters are again kept constant at a screw speed of 150 min^{-1}, embossing force of 880 N, roller temperature of 40 °C and a roller speed of 4 m/min. Figure 4.15 shows the results of extruding with different melt temperatures. Higher melt temperatures reduce the amount of edge rounding and enable the imprinting of smaller structures, especially for pillar-type

Pillar-type structures

Hole-type structures

1 bar (≈ 880 N)
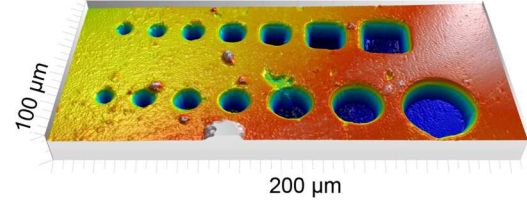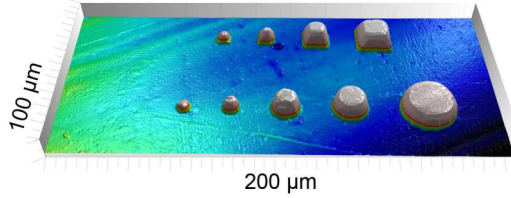
2 bar (≈ 1750 N)
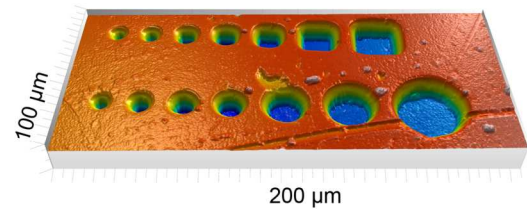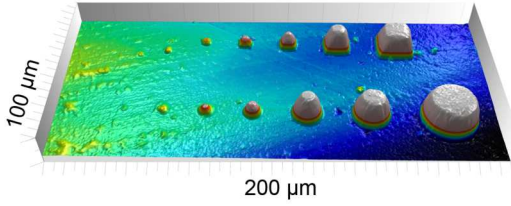
3 bar (≈ 2650 N)
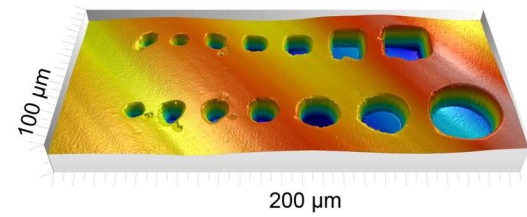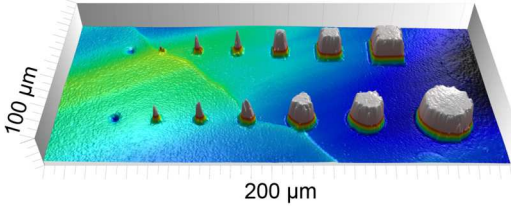
4 bar (≈ 3500 N)
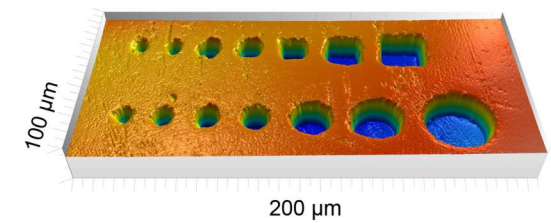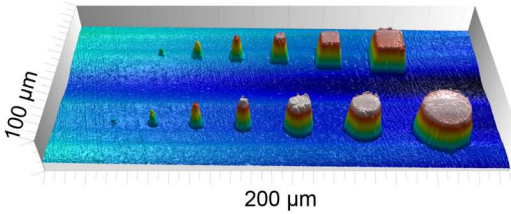
Figure 4.14: Force dependency of the imprints. On the left side pillar-type structures and o the right side hole-like structures are depicted. Higher embossing forces (higher line loads) lead to more accurate imprints, especially for smaller structures. Furthermore it can be observed that holes are more easily imprinted than pillars. The scale of the vertical axis is 2 μm, the largest circle has a diameter of 30 μm, the smallest has a diameter of 4 μm.

structures. When exceeding 240 - 245 °C edge rounding becomes more pronounced again while the smallest structures are still being imprinted. It can therefore be recommended to select the temperature as high as possible without exceeding the manufacturers' recommendations This is in line with literature recommendations for the production of flat cast film [88].

Figure 4.15: Effect of melt temperature on structure quality. Higher melt temperatures lead to better imprints, especially for small pillar-like structures. If the melt temperature exceeds 240 - 245 °C the edges of the structures appear to be more rounded. The scale of the vertical axis is 2 μm, the largest circle has a diameter of 30 μm, the smallest is 4 μm in diameter.

Roller temperature   The roller temperature was varied between 20 °C and 50 °C while the other parameters were kept constant at a melt temperature of 230 °C, screw speed of 170 min⁻¹, embossing force of 880 N and roller speed of 3 m/min. Earlier experiments showed that roller temperatures under 20 °C lead to very poorly imprinted structures. Figure 4.16 shows the results of the experiments regarding roller temperature. It is obvious that higher roller temperatures lead to better imprints. With increasing roller temperature, the structures are closer in height to the master structure as well as more sharply defined, with less edge rounding. Smaller structures get imprinted correctly at higher roller temperatures. Temperatures over 45 °C lead to polymer film sticking to the roller and periodically ripping off in a stick-slip type of motion. This leads to large visible marks across the entire film and a worsened structure quality. For some pillar like geometries, a ring like structure was formed around the pillar, when the roller temperature exceeded 45 °C, which might also be an indication of a sticking effect. Early tests showed that coating the shim with a PTFE based mold release agent (Teflon AF 1600, AGC Chemicals Europe Ltd.) can mitigate this sticking effect and enable embossing at higher roller temperatures, possibly leading to increased structure quality. This effect will be discussed in detail in the next paragraph.
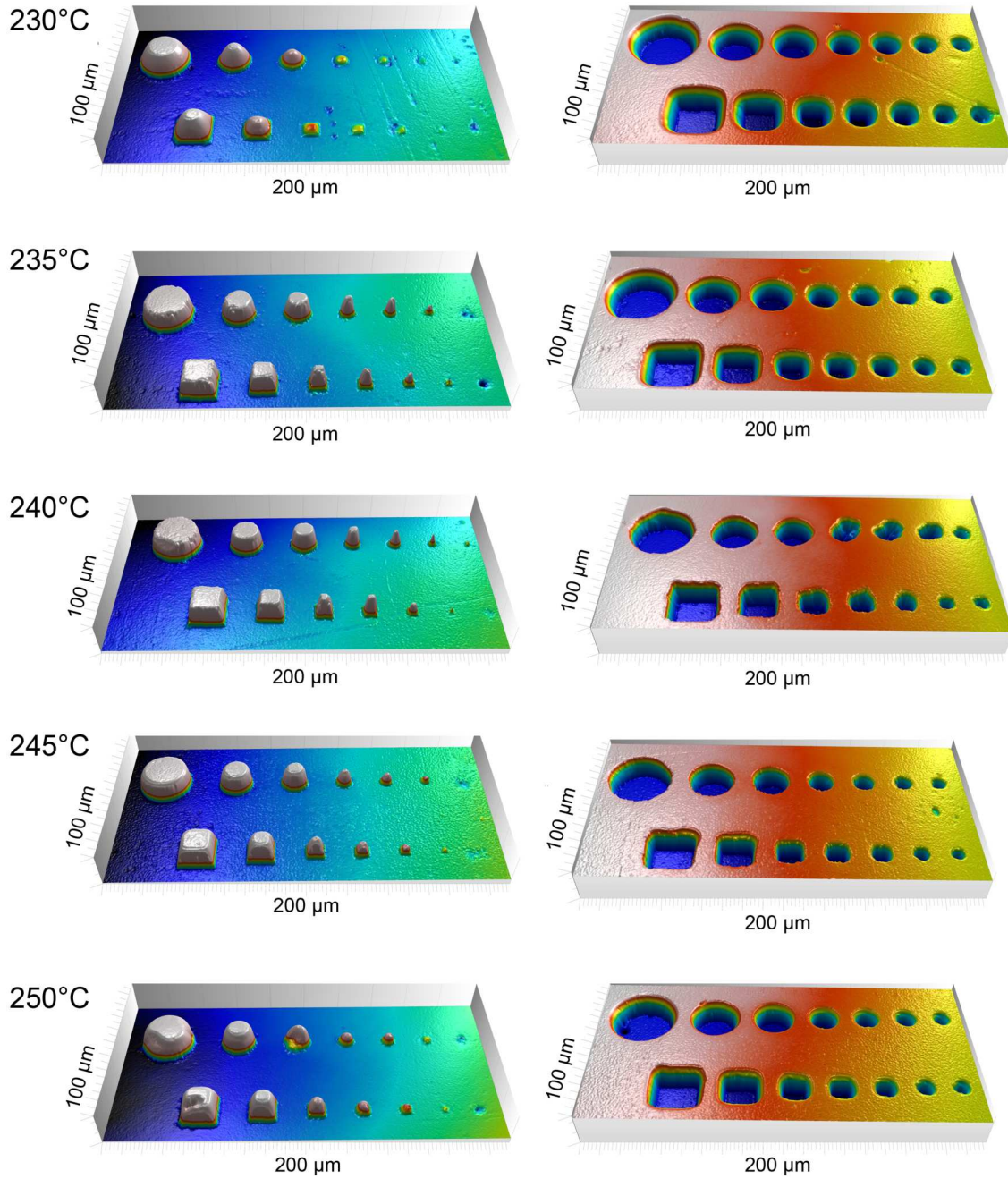
One unexpected challenge that arose was the heat dissipation of the roller, that was apparently too low, resulting in an increasing roller temperature over time. The higher the melt temperature, the faster the roller heats up, to the point where the polymer film stuck to the roller and reasonable film fabrication became impossible. Depending on parameters, after a couple of produced meters the roller was too hot to further produce any film. A new roller made of 7075 aluminum improved this issue but could not resolve it completely. Placing thin graphite film in between the different parts of the expanding roller led to a further improvement of the overall thermal conductivity of the roller. With these measures, the heating of the roller became manageable in the context of a proof of concept - for production on an industrial scale a redesign of the cooling system would be necessary.

Coating of the shim and the use of mold release   As stated above structure quality can be improved by increasing the roller temperature in order to keep the polymer surface more viscous and therefore enable better flow into all cavities of the mold. However, roller temperatures above 45 °C lead to sticking effects and subsequently macroscopic marks across the film, that are clearly visible even by the naked eye. To overcome this issue, coating the shim in mold release might provide a viable solution. As a first test parts of the shim containing test structures was covered with Teflon AF 1600 in FC 40 CYTOP solution (AGC Chemicals Europe Ltd.). After the solvents evaporated a 300 nm thick layer of PTFE was left on the shim. In order to proof the effect of this coating, only one half of the shim was covered, while the other was not coated. This shim was then imprinted at a melt temperature of 230 °C, extruder speed of 170 rpm, roller speed of 3 m/min and a roller temperature of 40 °C. It has to be noted that these experiments were done before the improvements to the cooling system of the roller described in the section
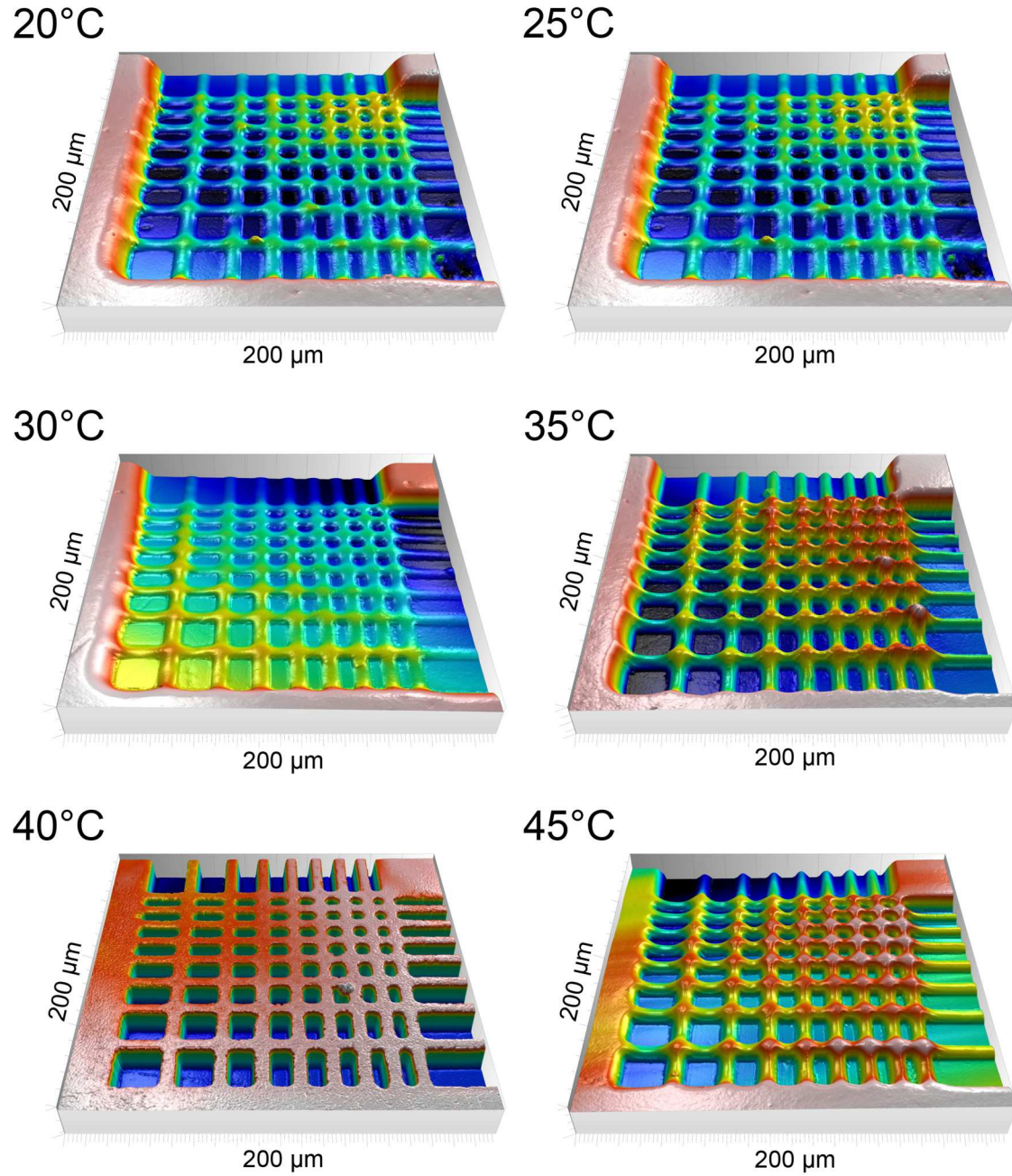
Figure 4.16: Test structures imprinted at different roller temperatures. Higher roller temperatures result in improved imprints with minimal edge rounding and even the smallest structures are fully formed. If the roller temperature is too high, sticking of the polymer film to the roller occurs, which leads to visible marks on the film. In these areas the structure quality is bad and large deformations in the film are present. The scale of the vertical axis is 2 μm, the largest square (front left corner) is 20 x 20 μm, the smallest (back right corner) is 3 x 3 μm.

above were implemented. Thus the roller temperature was 40 °C at the beginning of the experiment but then slowly rose as more film was produced. After about two minutes of production first sticking effects were observed in the uncoated section of the shim. While still small, the marks produced by this sticking effect were clearly visible even with the naked eye. Structure quality in the area of these marks is very poor. The coated part of the shim did neither show sticking effects nor the resulting defects. As can be expected mold release agent aids in mitigating the sticking effects and therefore enables imprinting at higher roller temperatures, which has been shown to produce more detailed imprints in the previous sections. However when observing the actual microstructures, it is immediately obvious that the structure quality is greatly impaired by the PTFE coating (see Fig. 4.17). The small structures are not imprinted at all, while the edges of the larger structures are rounded. This is readily explained by the relatively thick layer of PTFE covering the structures. Typical layer thicknesses for mold release agents are above 100 nm and many release agents form particles and aggregations with diameters in the μm range [76]. Therefore these agents can only be used for relatively coarse structures. For such kinds of large structures mold release might provide the benefit of lower roughness surfaces - in contrast to that the use of these industry standard mold release agents does not seem to make sense for imprinting in the low/sub- μm range [161]. Other works covering the use of mold release agents in hot embossing applications come to similar conclusions [76]. Another option to mitigate the sticking effect would be the use of chemical or physical mold releases such as silanization or coatings applied by physical/chemical vapour deposition that can achieve thicknesses of about 10 nm. However, complex handling, especially when applying these coatings to large shims, as well as high costs might render such solutions unpractical for some applications.
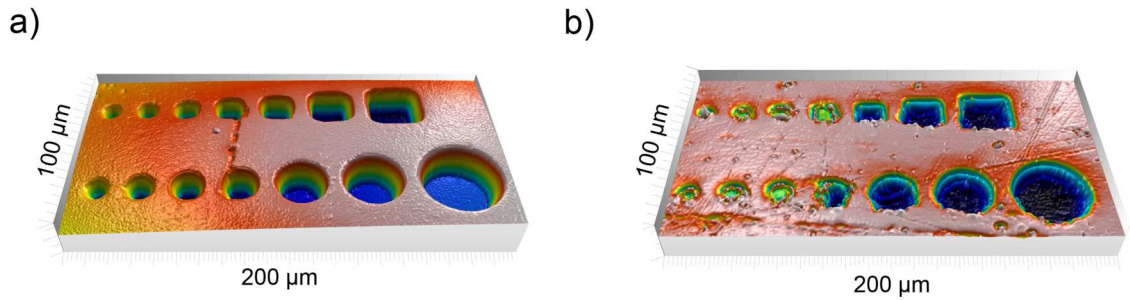
Figure 4.17: Comparison of microstructures imprinted without (**a**)) and with (**b**)) mold release. The height of the vertical axis is 2 μm, the diameter of the largest circle is 20 μm, the smallest is 4 μm in diameter.

4.5.4 Comparison of R2R and P2P Imprinting

In this section the structures produced by roll-to-roll hot embossing are compared to structures produced by traditional plate-to-plate embossing. The structures chosen for this comparison are on the one hand the "Nemo EduKit" - a set of structures intended to be used in education in the context of micro optics [162] - and on the other hand the structures found on the scales of various reptiles. The functions and applications of these reptile structures are presented in detail in Chapter 5.
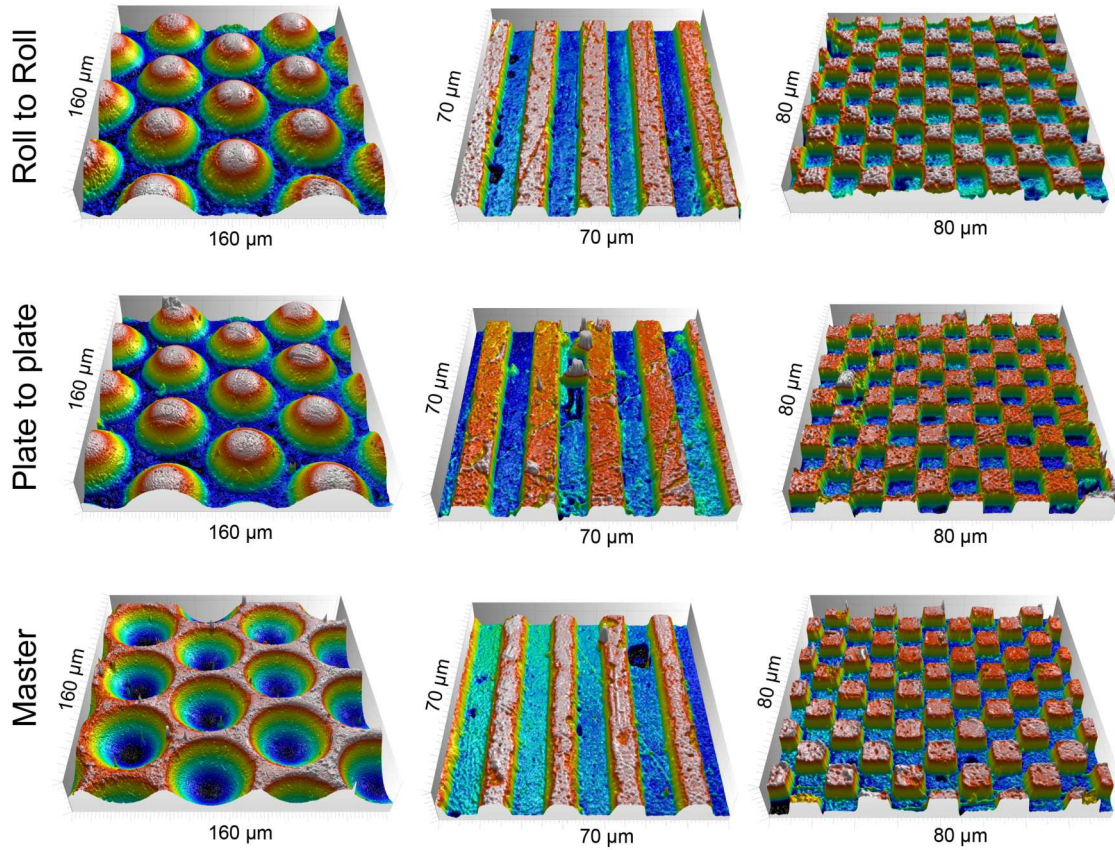
Figure 4.18: Comparison of R2R and P2P embossing. The leftmost column shows a microlens array, the middle column shows a diffraction grating and the right column shows imprints of a checkerboard pattern. Unfortunately the shim used to produce these structures had a number of defects, but in general the imprints are of very similar quality. The scale of the vertical axis is 6 μm for the micro lenses and 1.5 μm for the grating and checkerboard pattern.

As a first example Fig. 4.18 shows selected structures of the Nemo EduKit, once imprinted with the presented R2R process and once with traditional P2P embossing. Unfortunately the master shim that was used for both imprints had a number of defects that are in turn replicated in the imprints. Nevertheless the imprints looked very similar for both the relatively large lenses (diameter: 40 μm), the diffraction grating (line width: 8 μm)

as well as the checkerboard pattern (size of individual fields: 8 by 8 μm). This shows that roller embossing structures in the single digit μm range is not only possible but can yield results of similar quality as plate-to-plate embossing. Experiments conducted with industry partners lead to believe that even smaller structures - even in the sub-μm can be imprinted.
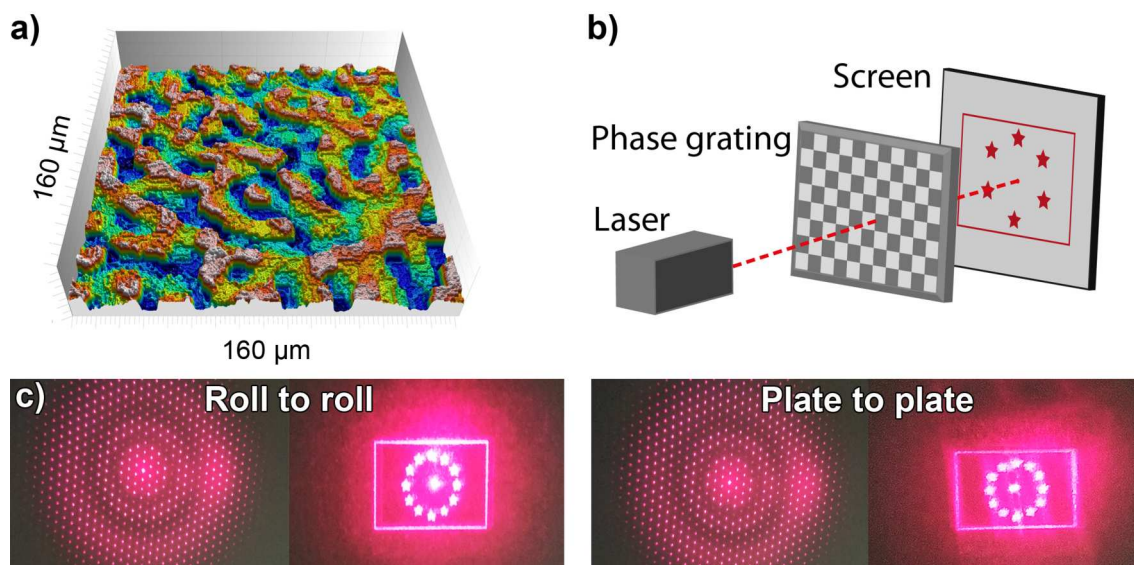
Figure 4.19: a) A selection of phase gratings are part of the NEMO EduKit. If a laser source is pointed through a phase grating, the beam can be shaped into arbitrary profiles. The CSM image (vertical axis = 3 μm) depicts a part of the phase grating used to form the light beam into the European Union's flag. **b)** Schematic showing the use of a phase grating to shape a laser beam. **c)** The photographic images show different light patterns (concentric rings and European flag) created by using phase gratings embossed with P2P and R2R hot embossing. The light patterns created by R2R and P2P embossing are almost identical, proving that these P2P and R2R produced structures are identical in function.

The NEMO EduKit also contains various phase gratings. While these structures might look arbitrary at first glance, such gratings can be used to shape a laser beam into almost any other shape. The varying material thickness of this grating introduces a phase shift between different parts of the laser beam leading to an interference pattern in the desired shape. Gratings like this are often used to transform a Gaussian beam profile into a top hat profile, but many other options are possible. The NEMO EduKit has a grating that shapes the Gaussian beam profile into concentric rings and another grating that shapes the beam into an European flag. Figure 4.19 shows the gratings, a schematic of how they are used as well as the resulting interference patterns. The gratings were produced by R2R and P2P embossing in order to compare the embossing processes. Both, R2R and P2P embossed gratings perform almost identical, i.e., the gratings are identical in function.

Figure 4.20 shows another comparison, it depicts reptile inspired structures imprinted with R2R and P2P. The shims used for the imprints were not identical, as the shim for the R2R imprints needed to be stitched using the process presented earlier in this chapter.

Since the master structure is copied multiple times in this stitching process, the molds used for the R2R and P2P imprints are in effect negatives of one another. Since the valleys of the R2R embossed structures show the same rounding as the peaks of the P2P embossed structure, this edge rounding can be disregarded as it is clearly part of the master mold. The main difference between these samples is the surface roughness that is increased for the sample embossed with the R2R process. The average roughness (Ra) for the R2R sample is 8.97 nm and 4.95 nm for the P2P sample, excluding the structure itself. While the roughness of the R2R imprinted sample is almost twice as large as of the P2P embossed one - it has to be noted that the overall structure height of the reptile inspired surfaces is only about 200 nm and a surface roughness below 10 nm is still very smooth.
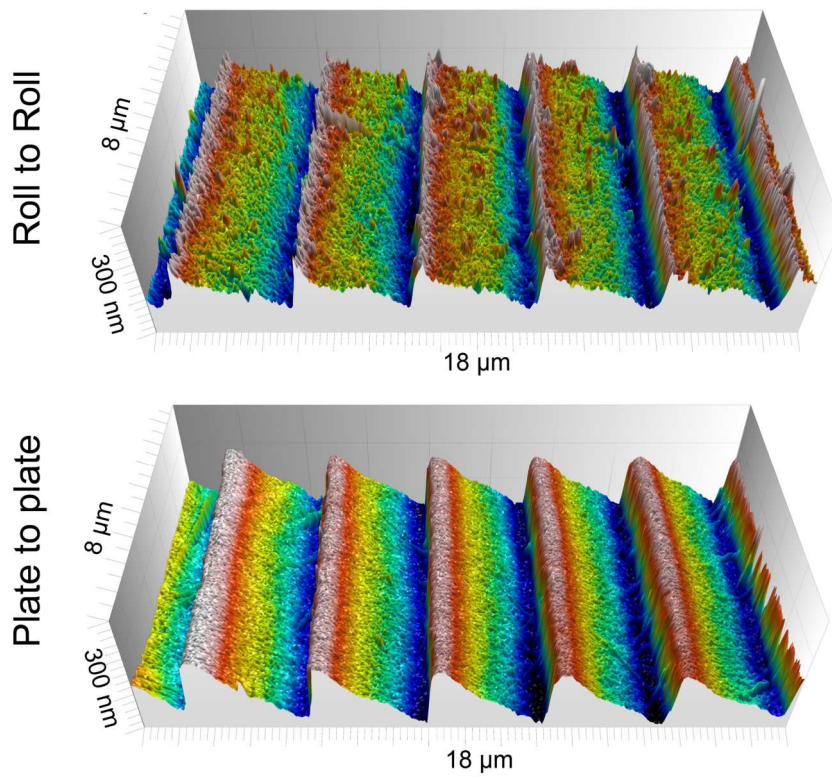
Figure 4.20: AFM scan comparing R2R and P2P embossing using sandfish inspired surfaces (see Chapter 5). While both processes manage to imprint the structures quite well, the increased surface roughness of the roller embossed sample is immediately obvious. The increased edge rounding is due to technical reasons in the shim production process.

In general it can be noted that there are some limitations to the roller embossing process presented in this thesis. For very high aspect ratio structures any roller process will always be less precise than plate-to-plate embossing due to the rolling motion of the mold bending pillars or causing sloped sidewalls on hole like structures. While larger roller diameters can mitigate this problem, mold fabrication becomes much more challenging for larger rollers. In P2P embossing almost all thermoplastic polymers can be used while the R2R process presented in this thesis can only imprint structures in thermoplastic polymers

that are compatible with film extrusion, e.g., have an sufficiently high melt flow index. Lastly, for some very small, sharply defined, pillar-type structures with a lateral size below about 5 μm plate-to-plate embossing will yield better results. On the other hand roller imprinting greatly increases productivity of the hot embossing process and enables the production of large scale, continuous samples, which is not possible in P2P embossing. For many of the structures found in micro optics, micro fluidics or micro mechanics the direct extrusion R2R process and traditional plate-to-plate embossing can produce similar high quality results.

Chapter 5

Towards R2R Fabrication of Sandfish Inspired Surfaces

This chapter introduces biomimetic surfaces inspired by an interesting reptile, the sandfish. It explains their interesting features and outlines the possible technical applications of such surfaces in the field of solar power. First the geometry of various artificial sandfish scales are tested on a custom built experimental setup in order to determine the optimal geometry of the microstructures. Afterwards surfaces featuring these geometrical parameters are produced using the stitching process and the roller embossing process presented in the previous chapter, as well as via UV imprint. Lastly the produced film is laminated onto photovoltaic panels and tested under laboratory conditions as well as in the field in order to prove the usefulness of sandfish inspired surfaces to photovoltaics.

5.1 Surfaces Inspired by the Sandfish

An interesting example of a microstructure that is of great interest for large scale structuring is inspired by the so-called sandfish (*Scincus scincus*). The sandfish became widely known for its ability to locomote quickly on and underneath loose granular soil; its movements resembling a swimming motion, hence the name. Its main habitat are the North African deserts from the Sahara up into the Arabian Peninsula [44]. There this lizard uses a strategy of burying itself underneath the sand to ward off predators and cope with the extreme heat in direct sunlight. Complete burial can take less then two seconds [44]. The sandfish is able to move significant distances underneath the sand and reach speeds of up to 30 cm/s by employing a form of locomotion literature calls "sand swimming" [163, 164, 165, 166, 167]. Interestingly the scales of the sandfish do not seem to experience significant wear even when moving through an extremely abrasive medium such as desert sand that would scratch most technical surfaces. It has to be noted that the sandfish does not solve the abrasion problem through shedding of the skin since this takes place only every three months [163], neither is this a result of special material properties of the scales as they consist mostly of ordinary β-keratin. The remarkable friction and abrasion properties of sandfish scales have led to many studies into their origin and possible applications in tech-

nical environments [163, 164, 165, 168, 169, 170, 171, 172]. These studies found micro- and nanostructures on the scales of the sandfish that can, at least in part, explain the properties of the scales. Figure 5.1 depicts the structures found on sandfish scales as well as the structures found on various snake scales. The dorsal scales of the sandfish show relative straight, step like structures with small ripples at the edge. The height of these steps is around 300 nm and the periodicity around 3 μm, while the ripples at the edges are about 40 nm. In Figure 5.1 the ventral scales of a snake - more specifically the Chinese cobra (*Naja atra*) can be found as well. The structures found on snake scales are remarkably similar to the ones found on the sandfish, which seems logical, considering that both scales are constantly in contact with the ground. The structures on snakes are also ramp-like, but instead of a straight edge the structures resemble more of a finger like shape. While the periodicity is about the same as for the sandfish, the height is considerably lower. The pictures were taken by Weibin Wu [46]. His Ph.D. thesis focused on the frictional properties of sandfish and snake scales on the micro-scale. An very interesting finding of this study was the anisotropy of friction on reptile scales like these. Using AFM it was found that the friction coefficient of various materials (AFM cantilever, PDMS microspheres, sand grains) on reptile scales is higher in the direction tail-head than in the direction form head to tail by a factor of 1.5 to 14.3. This anisotropy most likely evolved through evolution in order to aid in locomotion [46].

This friction anisotropy can be used to move granular media. The setup is surprisingly quite simple - a vibration motor, similar to the ones used in smartphones, was attached to a glass slide that had a snake scale attached on the other side. The small size of sandfish scales prevented their use for this experiment [46]. By activating the vibration motor the particles move slowly in the direction of the lower coefficient of friction, eventually falling off the sample. This way it was shown that surfaces with an anisotropic coefficient of friction can be used to transport granular media. This principle can now be used to aid in cleaning solar panels. Dirt and dust on photovoltaic panels, blown there by wind, can cause efficiency losses of 80 % in just five months if no cleaning is done [9, 6, 173]. This is especially true for dry and dusty climates such as in the middle east where efficiency losses of 0.55 % per day have been observed [173]. A study aiming to maximize the financial gain from solar farms estimated the optimal the cleaning interval of solar panels based on various factors, such as price of labour, efficiency losses, and price of the produced electricity, anywhere from weekly to once a month for very dusty climates [174]. One has to keep in mind that in these arid regions water used for cleaning is often a scarce resource, that has, more often than not, to be transported with trucks. An automatic cleaning system that uses no water would be ideal for solar farms in desert regions. Weibin Wu demonstrated a first proof of concept in his PhD thesis by moving individual grains of sand in distinct directions using microstructured surfaces and vibration. This effect was coined "dry self-cleaning" [46].
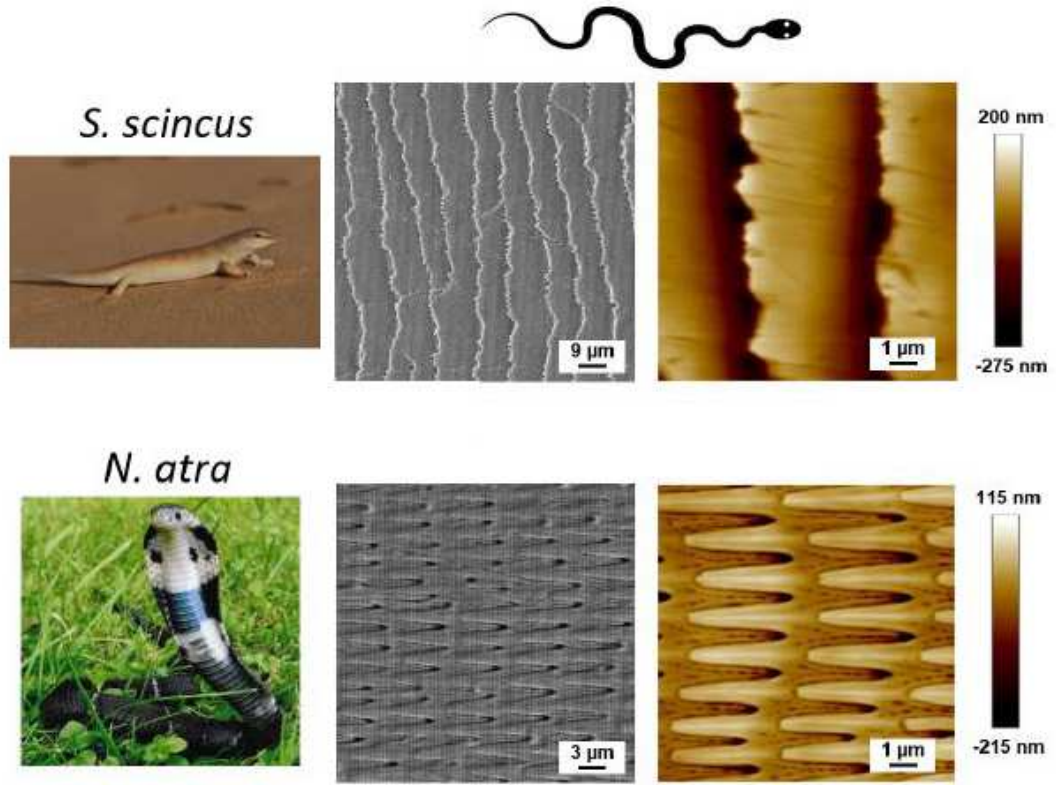
Figure 5.1: Structures on the scales of the sandfish (*Scincus scincus*) and the Chinese cobra (*Naja atra*). While the structures of the sandfish resemble very flat steps with nano-finger-like structures at the edges, the snake scales resemble flat finger-shaped ramps. Both structures lead to anisotropic friction. Pictures reproduced from Weibn Wu et. al. [46].

The aim of my part of this study was to determine the viability of dry self-cleaning on a large scale. Therefore, a new experimental setup for studying the effects of different microstructure geometries and excitation parameters had to be developed. Using this setup a range of different samples was tested in order to determine the optimal parameters. Following these experiments, molds were prepared and the structures were imprinted into a polymeric film. Lastly the film was laminated onto solar panels and experiments in the lab as well as in the field were conducted to prove that the concept of dry self-cleaning can work in the real world.

5.2 Experimental Setup for Granular Transport

This chapter describes and analyzes the experimental setup that has been used in previous works to test the transport of granular media on reptile-like surfaces via vibrations. Subsequently it describes the modifications and improvements that have been done in the scope of this work to improve these measurements.

5.2.1 Existing Setup

The setup used in earlier publications is shown in Fig. 5.2. It consisted of a glass slide or silicon wafer to which the sample - in this case snake scales of different species - were glued using a two component glue or double sided tape [46]. The glass slide was fixed in place on the table of an observation microscope using regular green tape. Next to the sample one, or in some cases multiple, vibration motors were glued to the glass slide. These had a height of 2.7 mm and a diameter of 10 mm and were driven, using a standard laboratory power supply, at 1.5 V and 0.05 A. This led, at least in theory, to a circular vibration with a frequency of 110 Hz with harmonics at 220 Hz and 330 Hz [45]. Previous works described this vibration as more or less "random". In practice dismantling one of the motors showed that, due to their construction, there is most certainly a part of the vibration in the vertical direction, and due to the probably quite large manufacturing tolerances for cheap motors like the ones used, not all motors perform exactly in the same way. While this setup was sufficient for a first proof of concept of particle transport via vibrations - an improved version was deemed necessary in order to gain more control over the applied vibration, *i.e.*, amplitude and frequency. A first step to develop such an improved setup started with analysis of the exact vibrations created by the simple vibration motors.
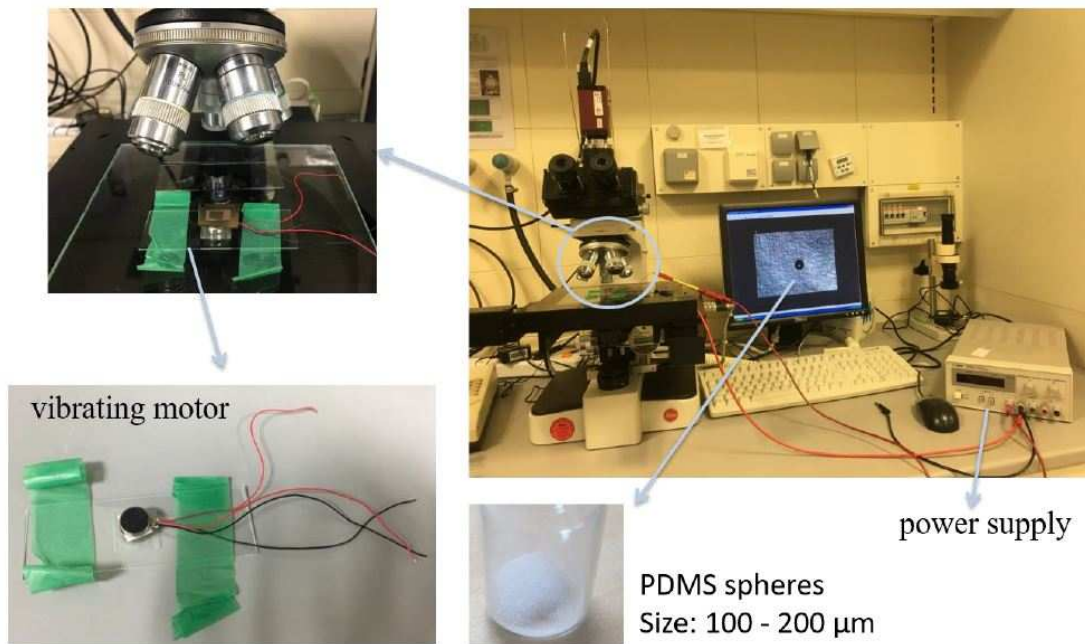
Figure 5.2: The setup used to test the transport of granular media on reptile-like surfaces through vibration. The vibration is created by a small vibration motor, the movement of the particles can be observed through a microscope. Image reproduced from Weibin Wu et. al. [46].
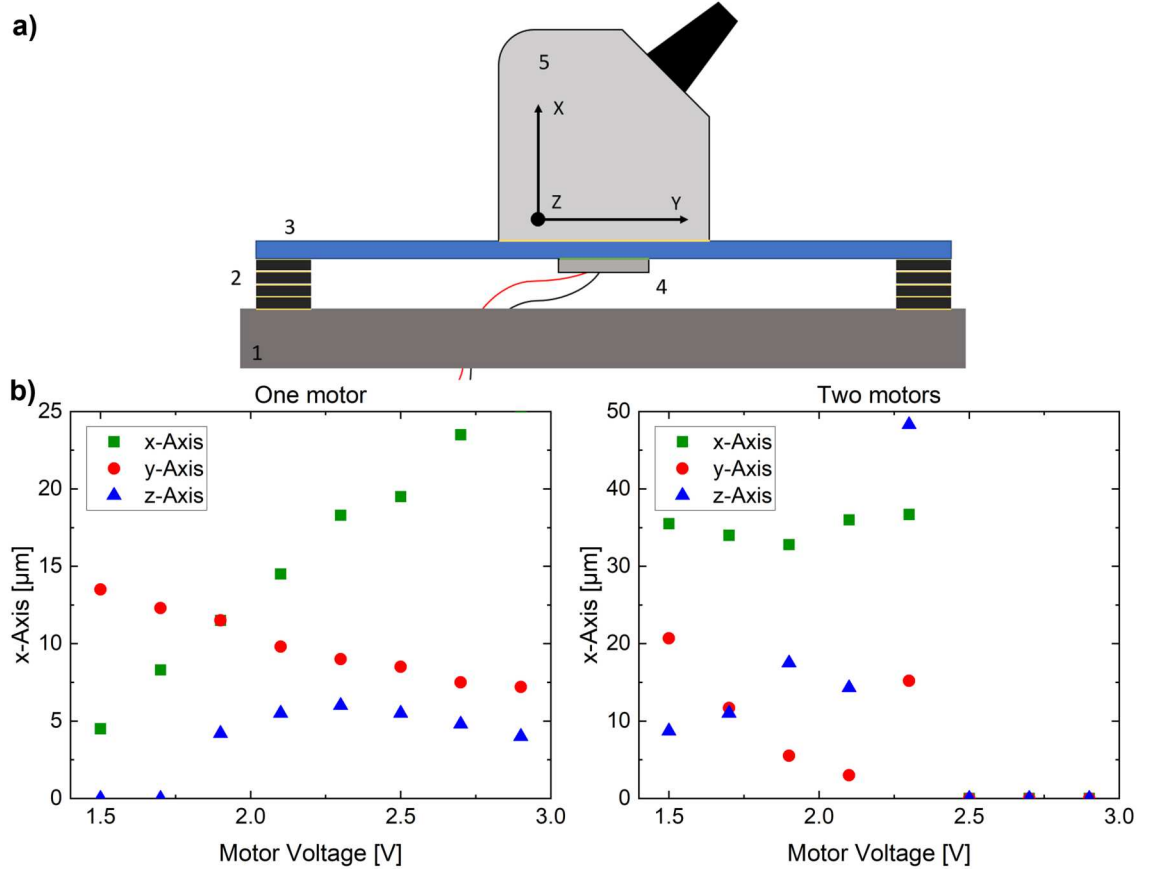
Figure 5.3: a) Schematic of the setup for testing the vibration motors. 1) Heavy substrate plate, 2) Elastic polymer strips, attached with double sided tape, 3) Glass slide, 4) Vibration motor, 5) Vibration Sensor PCE-VM 3D. **b)** Displacement of the glass slide with one and two motors. The higher the voltage on the motor, the higher the displacement in x direction. With two motors the displacement is considerably larger, also there seem to be interference/synchronization effects.

To get a better understanding of the vibration that these motors create, a test setup, displayed in Fig. 5.3, was built. It used a PCE Instruments VM 3D vibration sensor to record the vibrations created by the motors. This instrument is conceived to measure mass imbalances in rotating parts or defects in ball bearings. Its large mass in comparison to the samples of snake scales usually used in previous works will definitely influence the measurements. Nevertheless these measurements can still serve as a benchmark for further design steps of an improved setup. This exact vibration measurement setup with elastomer strips on the sides and the vibration motor mounted underneath the sample has prior been tested with snake scales and PDMS spheres and the results of Wu et al. [46] were replicated using it.

Figure 5.3b) and c) review the results of the measurements for one and two stacked motors, respectively. The vibration is three dimensional and the x,y and z components are in the μm ranges. Its amplitude increases with the voltage used to drive the motors. Strong variations of the amplitude, especially when using two motors indicate constructive/destructive interference or synchronisation effects of the vibrations. In general, we can therefore actually assume that this vibration is, for our practical purpose, 'random'. If we assume that the lateral components of the vibrations are responsible for the particle transport we can conclude that an improved setup should at least be able to reach an amplitude of 35 μm. The frequency of the vibrations was measured by recording the acoustic signal of the motors and conducting a Fourier transform to calculate the frequency. The frequency of around 110 Hz was confirmed. To give more flexibility a frequency interval of 0-400 Hz was deemed appropriate for an improved setup. Several other "soft" requirements, such as the simple and easy exchange of samples, were collected and used to design the setup presented in the next section.

5.2.2 Vibration Stage

While a multitude of commercial options for vibrating test-beds exist, almost all of those are too large (smallest sample masses in the range of several kilograms), or can not guarantee precise control over the amplitude of the vibration. For theses reasons it was decided to build a customized vibrating stage that better fulfills the requirements for the planned experiments. This section covers the design process for an improved setup to test the movement of particles on reptile-inspired surfaces, which includes the mechanical design as well the selection of the actuators. The mechanical and electrical design work was carried out in cooperation with Marcel Ade in the framework of his master's thesis [175].

Mechanical design   Several different setups for a vibration stage, from aerostatic bearings with external actors to different variations of electromagnetic actors, were collected, criteria for the selection were defined and the different concepts were rated. After some consideration, it was decided to build a piezo-actuated compliant mechanism that is shown in Fig. 5.4a). This mechanism is similar to the stages used in mirco-positioning in, e.g., atomic force microscopes [92]. The motion is guided via compliant joints, that use the elastic deformation of the material. In this case the joints are realized using simple cantilevers with a rectangular cross section. Because of the rectangular shape the area moment of inertia of the cantilevers is much higher normal to the surface of the stage than in the intended direction of movement, leading to a precise motion in one axis. The mechanism also serves as an interface and a housing for the actuator. The interface of the actuator to the mechanism is realized by a small, rounded protrution that serves as an articulating joint and point of force transmission. At the other side of the actuator it can be prestressed via a screw with a flat end. Driving the stage directly with piezo actuator would theoretically be possible, but sourcing sufficiently large piezo stacks that support the required frequencies proved to be difficult, so a lever with a ratio of 6.5 to 1 was introduced to be able to use actuators with a smaller displacement to realize a stage displacement of

over 30 μm. Another compliant bearing was introduced near the tip of the lever to reduce the rotation of the stage around the z-axis. The bending stiffness of the lever plus the stiffness of the cantilevers used to guide the motion add together to the spring constant of the mechanism. The exact geometrical measurements of the lever and the cantilevers were a result of iterative FEM simulations (see Fig. 5.4b). The goal of these simulations was to create a mechanism that can work with commercially available piezo actuators, while at the same time realizing the needed amplitude of the vibration. Furthermore the mass of the mechanism needed to be as low as possible to keep the eigenfrequencies, which limit the maximum frequency at which the setup can run, as high as possible. The dimensions were chosen in a way that at a force of 400 N the stage would be deflected in x-direction by 37 μm, while the maximum stress in the joints is around 30 MPa which is well under the elastic limit as well as the fatigue strength of the chosen aluminium (EN AW 5754). To be able to drive the actuator at high frequencies a hole at the side of the housing was introduced to provide air cooling for the actuator. Furthermore mounting holes for the stage itself as well as a sample holder were introduced. Since this design requires intricate and very precise cuts to be made in 12 mm thick aluminium, wire EDM was chosen as manufacturing process. These works were carried out in the machine shop of the IMT A version of the mechanism with two independent axis was developed and simulated, but it was decided that for the scope of this thesis a one axis version would be sufficient.

Selection of actuators It was decided that piezo actuators are the easiest and most precise type of actuator to produce the movement of the stage. Using the provided performance charts, the stack multilayer piezo actuator P-887.51 by Physik Instrumente was selected. This actuator has a nominal displacement of 13.9 μm at 400 N, so with the usual spread in piezo actuator performance it is able to reach a displacement between 12.5 μm and 15.1 μm. Its capacity of 3.1 μF, maximum operating voltage V_{PP} = 120 V and current of I_{max} = 0.47 A at 400 Hz required the use of an analog voltage amplifier (Physik Instrumente E-617.001). The voltage signal that controlled the amplitude and frequency of the vibration was generated by a standard function generator (Voltcraft FG 2102), that plugged its signal into the aforementioned voltage amplifier.

The dissipation losses of the actuator, when used at its electrical limits, can add up to 271 W, which heats up the actuator to 175 °C. This in turn would lead to an additional thermal expansion of the actuator of 11.1 μm. This would create improper stress in the joints of the mechanism. Therefore the actuator has to be cooled; in this case it was decided to use an impingement cooling. Pressurized air enters the housing through a hole in the side, hits the side of the actuator and exists through the bottom of the actuators housing thereby keeping the temperature of the actuator in acceptable limits. Experiments showed that at full displacement and maximum frequency the cooling can keep the actuator temperature at about 5 K above room temperature.

Lastly the interface protrusion of the housing, that prevents the actuator from being bent, introduces large point loads on the piezo actuator. To keep the brittle ceramic from breaking metal end caps were glued on the ends of the actuators to distribute the load
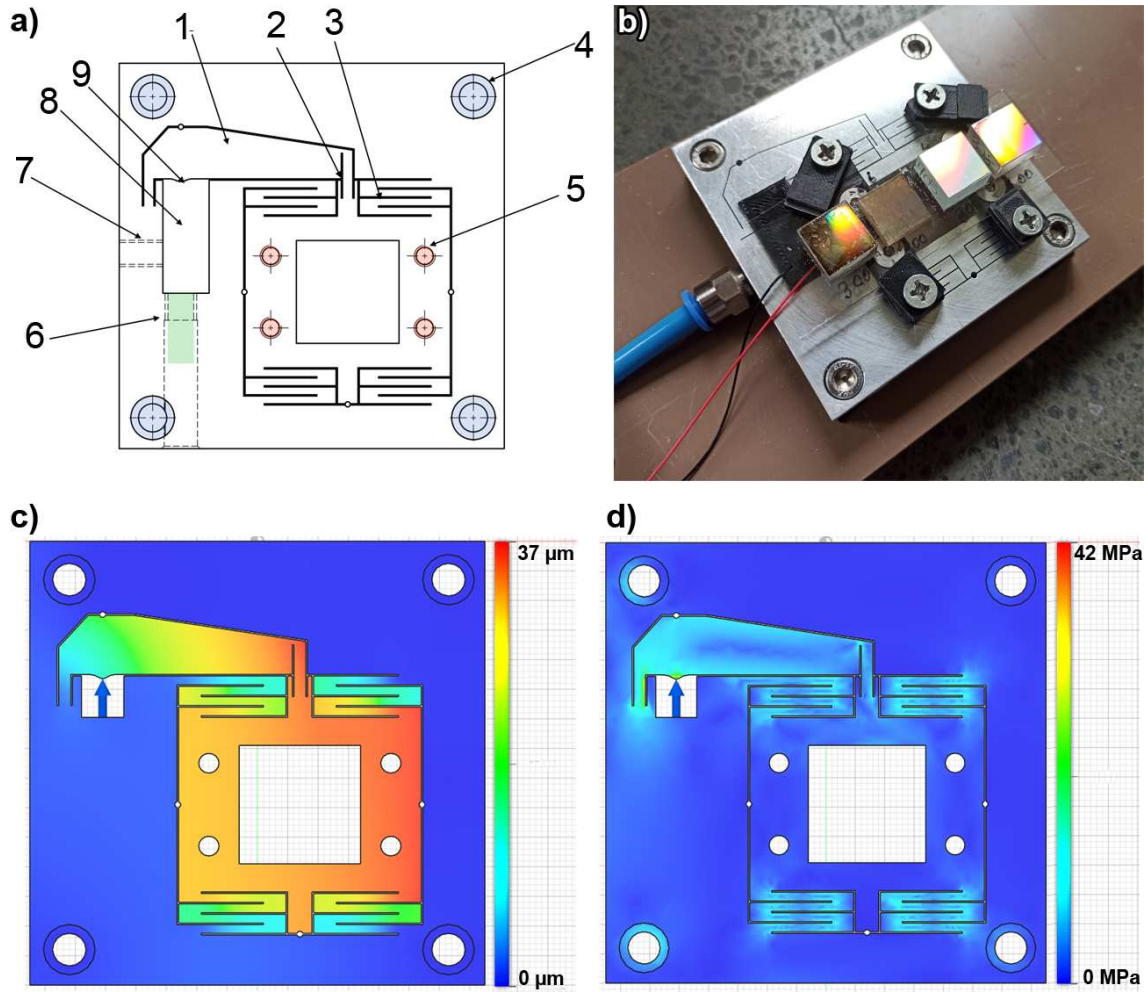
Figure 5.4: a) The compliant mechanism for the vibrating stage. 1) Lever to increase the actuators displacement 2) Relief cut that mimimizes rotation of the stage around the z axis 3) Cantilevers that allow motion in one axis 4) Mounting holes Opening for piezo actuator 5) Mounting holes for sample holder 6) Screw for pre-stressing the actuator 7) Air duct for cooling of the actuator 8) Hole for the actuator 9) Interface protrusion. **b)** Image of the vibration stage with samples mounted on a sample holder. **c)** FEM simulation showing the deformation when the actuator is applying 400 N of force. This leads to the maximum deflection of the stage. **d)** Von Mieses stress in the material at 400 N of actuator force.

more evenly to the interface of the actuator.

5.2.3 Particle Tracking

In order to enable precise measurements and facilitate the analysis and comparison of different samples for different conditions, the observation of the movement of particles with the naked eye or a microscope is not sufficient. Tracking particles frame by frame manually works for single particles on few samples and measurements, but is far too tedious

to do for the kinds of measurements required. Therefore, an automated particle tracking system had to be implemented. Since commercially available solutions either did not work with the equipment that was at hand or did not fulfill the requirements we decided to develop a customized particle tracking algorithm. The software implementation was completed together with Alexander Rempel in the framework of his Bachelors' thesis [176]. The algorithm utilizes in six basic analysis steps:

Video recording For the first tests the digital camera "IDS uEye UI-1220SE-M-GL" (IDS Imaging Development Systems GmbH) was used. It is able to record an .avi video with a resolution of 500x500 pixels at a frame rate of 50 Hz. This camera was used in the development of the particle tracking system as well as in some pilot measurements with real samples. At frequencies above 200 Hz of the stage, a lot of movements were missed and the trajectories were not accurate due to the low frame rate of this camera. For later experiments this camera was replaced by a "Kron Technologies Chronos 1.4" camera that was recording a video with 700x700 pixels at 120 frames/s, which was sufficient to track particles accurately. In order to create sharp images, the exposure time of the camera was set as short as practically possible, in our case that turned out to be 0.6 ms. To aid the image recognition algorithm later on, a sidelight was used to illuminate the samples.

Image processing and recognition. The goal of the image recognition is to create a 2D grid with the positions of all particles in it for every frame of the video. The algorithm works as follows:

1. Enlarge the original picture: as it turned out, a higher resolution of the pictures is helpful for the further processing of the image. The Lanczos algorithm was used to enlarge the images [177].

2. Threshold operation: a cutoff is chosen by the user; all pixels with a brightness value under this cutoff are considered background and therefore set to black, all pixels above this threshold value are considered to be parts of the particles and are set to white. If camera settings or the lighting of the sample change this value needs to be adjusted.

3. Morphological operators: after the threshhold operation artifacts, both in the background as well as in the foreground are usually present. These can be eliminated by the following operations [178]:

   - Opening operator to close unwanted foreground objects
   - Closing operator to close unwanted background objects
   - Erosion operator to better separate individual particles

   To simplify the settings a graphic user interface was programmed to allow for optimized image processing. Afterwards all foreground pixels are assigned a value that

represents its Euklidean distance to the nearest background pixel. The local maximums of these values represent the centers of individual particles and are considered the position of the particle.

Connect the positions to trajectories. We assume that all particles are in motion, so that the position of all particles changes from frame to frame. If the framerate is high enough in relation to the speed of the particles, a particle that had a position in one frame will be close to the previous location in the next frame. Now, we have a simple allocation problem that we can solve by calculating the Euclidean distances of all points to all other points and choosing the connections between the points in a way that minimizes the sum of the euclidean distances between the points [179]. To speed up the algorithm, a position prediction was implemented, that can calculate the probable trajectory of a particle based on the trajectory of the particle in the last couple of frames and thus enables the program to disregard the computation of euclidean distances to many points that are way out of the area the particle is expected to be in. Furthermore there are some edge cases that need to be taken into account such as particles getting out of the field of view of the camera, particles attaching to one another and thus not being distinguishable as two individual particles anymore or the reverse case of a seemingly single particle suddenly "splitting" into two. After taking care of these edge cases the software gives us a number of lists that contain the respective location of every particle in each individual frame. These are called trajectories in the following.

Processing the trajectories and saving the data. The coordinates of the particles are given as pixel coordinates in the digital camera image. To get real world values in millimeters a calibration routine was added. Without changes to the setup a calibration object such as a strip of metal of known dimensions is placed on the sample holder and a picture is taken. The software can identify the object, calculate a scaling factor s in mm/px and then convert the pixel coordinates into real world coordinates. The speed of the particles can be calculated from

$$\overrightarrow{v}_{i,t,pixel} = \overrightarrow{x}_{i,t-1} - \overrightarrow{x}_{i,t} \tag{5.1}$$

with $\overrightarrow{x}_{i,t-1}$ and $\overrightarrow{x}_{i,t}$ being the positions of particle i in one picture and the preceeding one. With the following formula the velocity of the particles can be converted to mm/s.

$$\overrightarrow{v}_{i,t} = \overrightarrow{v}_{i,t,pixel} \cdot s \cdot f_{framerate} \tag{5.2}$$

Afterwards the trajectories are saved in plain text format that can easily be read by spreadsheet software, for example.

Interpretation of the trajectory data. To make the interpretation of the trajectory data easier the software calculates different measurements from the saved data:

- Average velocity vector of all particles at a given moment of time:

$$\overline{\overrightarrow{v}_t} = \frac{1}{m} \cdot \sum_i^m \overrightarrow{v}_{i,t}$$

For a better visualization the vector can be converted to polar coordinates where its radial component is the average velocity of particles and its angle is the average direction of the particles moving. $\phi = 0$ is defined as straight up motion in the image. Therefore:

$$\overline{\rho_t} = |\overline{\overrightarrow{v}_t}| \tag{5.3}$$

and

$$\overline{\phi_t} = arctan(\overline{v_{x,t}} - \overline{v_{y,t}}) \tag{5.4}$$

- Average velocity of a particle: The average sum of the velocity of all particles can be calculated by:

$$\overline{\varrho_t} = \frac{1}{m} \cdot \sum_i^m |\overrightarrow{v}_{i,t}| \tag{5.5}$$

This is the average velocity of all particles, not considering their respective directions of travel.

- Directionality: the quotient:

$$\lambda_{dir} = \frac{\overline{\rho_t}}{\overline{\varrho_t}} \qquad \rightarrow \qquad 0 \le \lambda_{dir} \le 1 \tag{5.6}$$

can help asses the directionality of the average movement. A value of zero would coincide with particles moving randomly about the sample, their velocities cancelling out, while a value of one indicates that all particles would be moving in the exact same direction.

- Number of particles not moving: Our observations showed, that some particles do not move or move very little for - at least - parts of the videos duration. Therefore particles with a velocity below a user defined threshold are disregarded for the velocity and directionality measurements. The number of theses particles in every frame is counted by the software.

- Polar histogram: the particle movement is split into a user defined number of direction windows, similar to a compass rose. Each of these windows is evaluated individually for number of particles in it, average velocities, etc. Furthermore a polar histogram can be generated, showing how many particles travelled in each of the direction windows.

- Data quality: since a trajectory needs at least two positions of the same particle, which is not always given, since particles bunch together and are indistinguishable, split up or move in/out of frame sometimes, usually the number of particles is higher

than the number of valid trajectories at any given moment. We define a quality quotient as follows:

$$\lambda_Q = \frac{N_{Trajectories}}{N_{Particles}} \tag{5.7}$$

Empirical observations showed $\lambda_Q \geq 0.95$ to be a good value to ensure a good measurement.

After the implementation the algorithm was extensively tested and verified, both with "simulated" particle videos where the measurement results were known, and with actual real world measurements. To make the operation of the particle tracking system easier, a graphic user interface was implemented. After successful verification that the system was working, actual measurements were conducted, the results of which are presented in the next section.

5.3 Movement of Particles on Technical Surfaces Inspired by the Sandfish

The goal of the experiments described in this section was to vary the geometry of the sandfish inspired features on the surface as well as the parameters of the excitation to find the optimal combination of parameters that lead to the most efficient cleaning of the surface. Once the optimal geometry of surface features is found a larger mold with these features can be fabricated to cover entire solar panels. These experiments were conducted together with Amelie Hamm in the framework of her master's thesis [180]. The experiments were all carried out in the following fashion:

1. The sample is attached to a standard microscope slide using double sided tape (Tesa Extra Strong), making sure that the sample is glued in the correct orientation. The microscope slide is attached to the vibration stage using the provided clamping mechanism.

2. The lighting of the sample has to be adjusted so that the camera can gather enough light to produce a correctly exposed picture, even at shorter shutter speeds. A grazing light leads to high contrast images and therefore improves the performance of the particle tracking software. Focal length and point of the camera were adjusted so that the sample filled the entire picture and the particles are all in focus.

3. The calibration strip was placed on the sample and a picture is taken. Now the settings of the camera should left as they are. This calibration image is later used by the tracking software to convert pixel coordinates into real world measurements.

4. About 50 - 100 particles were randomly placed on the sample using a small spatula.

5. The function generator and amplifier were switched on. The recording of the camera was started and the output of the function generator activated. This starts the vibration.

6. After one minute, or if no particles are left on the sample, the video recording is stopped. The sample is cleaned using pressurized air and is now ready for the next run.

7. The video is saved and then loaded into the particle tracking software. The trajectory data is saved alongside the video for further evaluation.

5.3.1 Technical Sample Surfaces Inspired by the Sandfish

Producing samples with step-like structures similar to the sandfish proved to be surprisingly difficult. Several approaches with different anisotropic etching techniques were discussed and after some initial experiments most of these techniques had to be discarded as unpractical or not feasible with the equipment and experience available at the IMT. One of the more promising techniques to produce sandfish-like structures, even on a rather large scale, is laser interferance lithography [181]. Since this technology was not available at the KIT, the group of A. Lasagni from the TU Dresden kindly provided some of their samples. These were produced directly in stainless steel, which would even have been a nice mold material for replication by hot embossing. However, the dimensions were about a factor of ten larger than the sandfish structures and the surface seemed to be very rough. Initial experiments showed that moving dust particles on a surface this rough can be quite challenging. Since both, reducing the dimensions as well as smoothing the surface were deemed quite difficult, this technique was also disregarded as not feasible for the planned experiments.

So-called blazed optical gratings were finally used instead. These have a precisely defined period, height and blaze angle and an overall shape that very closely resembles the structures found on the sandfish [182]. The main differences are, that the tiny, finger like structures at the edge of the steps, are missing in the gratings and their very high regularity. This regularity of the steps leads to - intended - optical effects; mainly refraction of incoming light. For a technical surface on a solar panel this is likely not a desirable quality; however, for finding the ideal combination of period, height, blaze angle and excitation parameters, the availability and relatively low cost of these gratings make them perfect test samples. Gratings like these are usually produced with precision mechanical ruling engines that scrape the individual grating lines using a diamond blade [182, 183]. Copies of this master can then be manufactured and sold relatively cheaply.

For our experiments we chose ten different gratings, the geometries of which are summarized in Table 5.1. The gratings have dimensions of 20 x 20 mm^2 and a height of 10 mm. The samples are made of a polymer resin on a float glass substrate. All samples were sputtered with a thin layer of aluminium. The gratings have a theoretical height, specified by the manufacturer (Richardson Gratings). Measurements showed that the actual height of the gratings deviates significantly from this specification. Therefore the samples were measured using AFM to confirm their actual height. The samples were named with the following convention: [Period in μm]-[Height in nm], e.g. 17-135. Furthermore friction measurements using the AFM in contact mode were conducted in order to determine the

extent of the friction anisotropy that the samples provide. The ratio of the friction force in trace (up the steps) to the force in retrace (down the steps) was chosen as a dimensionless measure of the extent of the anisotropy. Since this ratio has no unit, no calibration of the AFM was needed as the unit (in this case mV) will cancel out. As a reference a metallized polymer replica of a snake scale (*Naja Atra*) was added. The structures on this sample have a period of 3 to 5 μm and a height of 70 to 120 nm. It has to be noted, that this sample is by no means flat, but has, due to its biological origin, lots of scratches and dents in its surface. Furthermore a metallized flat sample without any structure was measured as a reference. Since the scales of sandfish are very small (< 1 mm^2) no sandfish scales or replicas thereof were tested as it is very hard to determine if there is any effect on an area that small.

Symbol	Name	Lines/mm	Blaze angle [°]	Period [μm]	Height (Specs) [nm]	Height (measured) [nm]	Anisotropy ratio
	08-80	1200	8.6	0.83	127	80	1.58
	08-210	1200	26.7	0.83	420	210	2.34
	17-135	600	4.3	1.67	125	135	2.94
	17-215	600	8.6	1.67	253	215	2.49
	17-650	600	28.7	1.67	911	650	2.48
	33-135	300	2.57	3.33	150	135	2.35
	33-235	300	4.3	3.33	250	235	1.39
	33-460	300	8.6	3.33	505	460	2.73
	33-1200	300	26.7	3.33	1677	1200	7.23
	67-235	150	2.13	6.67	248	230	1.71
	Snake	-	≈ 4	≈ 3-5	-	$\approx$ 50-100	≈ 1.1 - 1.4 [46]
	Reference	-	-	-	-	-	0

Table 5.1: The samples used for the experiments. The gratings have a theoretical height that can be calculated from their period and the blaze angle, both specified by the manufacturer. These values differ significantly from the actual height of the grating structures. The samples were named using their period and their measured height. In addition to the gratings a polymer replica of a scale of the Chinese cobra (*Naja Atra*). Furthermore a flat sample without any structure was added as a reference.

5.3.2 Determining Parameter Ranges for Design of Experiments

To be able to do a meaningful design of experiments, some preliminary experiments were carried out. In principle frequency and amplitude of the vibration can be varied with our

setup. The aim of these experiments was to decide on parameter levels and increments for both frequency and amplitude to minimize the number of individual experiments necessary in the main experiment. Furthermore particle size and the height of the structures were varied to confirm that both parameters have a significant influence.

For the first experiments the sample 33-180 was selected since its geometry is very similar to the structures found on sandfish scales. First tests showed that at frequencies below 150 Hz almost no particles move; the upper limit is given by the vibration stage, that can reach frequencies up to 400 Hz. For these first experiments a frequency increment of 10 Hz was chosen. The maximum amplitude that can be reached by the vibration stage is 28.25 μm. To gain an understanding of the influence of the amplitude, another experimental series with half the maximum amplitude was carried out. Both series were carried out with seasand with a grain size of 80 - 300 μm. This is approximately the same grain size that is prevalent in the natural habitat of the sandfish [184].
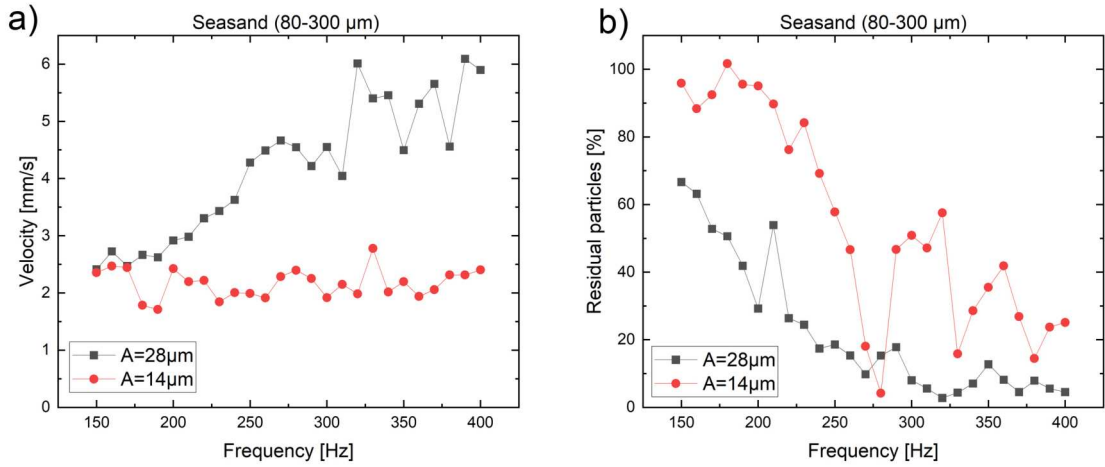
Figure 5.5: The average particle velocity (**a**)) and residual particles (**b**)) for different frequencies for seasand. As expected the velocities are higher for higher vibration frequencies and amplitudes. Consequently, the number of residual particles left on the sample after 60 seconds decreases for higher frequencies and amplitudes. Since not necessarily all particles are recognized at the beginning of the video values slightly above 100 % are possible. For both series the sample 33-180 was used.

The results of these experiments are reviewed in the following figures. Figure 5.5 shows the average velocity of the particles on the sample for different frequencies. Higher frequencies lead to higher particle velocities; this is more pronounced for the higher amplitude. The absolute values scatter a lot, especially for higher frequencies but a general trend can be observed. The number of residual particles that are left on the sample one minute after activating the vibration decreases for higher frequencies and amplitudes, as is to be expected. These experimental runs were also carried out using different particle sizes and different sample surfaces. In none of these runs was a frequency detected that led to a repeating pattern or an especially good value for velocity or residual particles. In order

to reduce the number of experimental runs and time necessary, it was decided that a frequency interval of 50 Hz in the following experiments would be sufficient to observe the general trends. Since the differences for the larger and lower amplitude were significant these two amplitude values were kept for the following experiments.

Another series of experiments was carried out using three different particle sizes. Seasand (SiO_2) (Merck KGaA) with a grain size of 80 - 300 μm, e-corundum (Al_2O_3) (Hafra Strahltechnik GmbH) F90 with a grain size of 125-160 μm and even finer e-corundum F220 with a grain size of 53 - 75 μm. Figure 5.6 displays particle velocity and residual particles for different frequencies for all three particle types. Smaller particles move with a similar average velocity as larger particles. The number of residual particles left on the sample is considerably higher for the smaller particles, especially for the finest e-corundum. This indicates either that smaller particles move more randomly, therefore staying on the sample for longer, or that the number of particles, that are not moving at all is much higher for smaller particles, since these particles are disregarded for the calculation of the average velocity. Since the curve of residual particles for e-corundum F90 is constantly in between the curve of the larger and smaller particles it was decided to use seasand and e-corundum F220 for the following experiments.

One peculiarity observed in these preliminary experiments was that some particles move very fast and very uniformly during the first couple of seconds after activating the vibration. These particles fall off the sample rather quickly. For the remaining time of the experiment mostly slow moving particles are observed on the sample. Since these slow particles are on the sample for much longer, they influence the average velocity much more than the fast moving particles. For that reason in some instances it is necessary to conduct a separate evaluation of the first second(s) of a video as well as the whole video to be able to differentiate between the "slow" and "fast" moving particles.
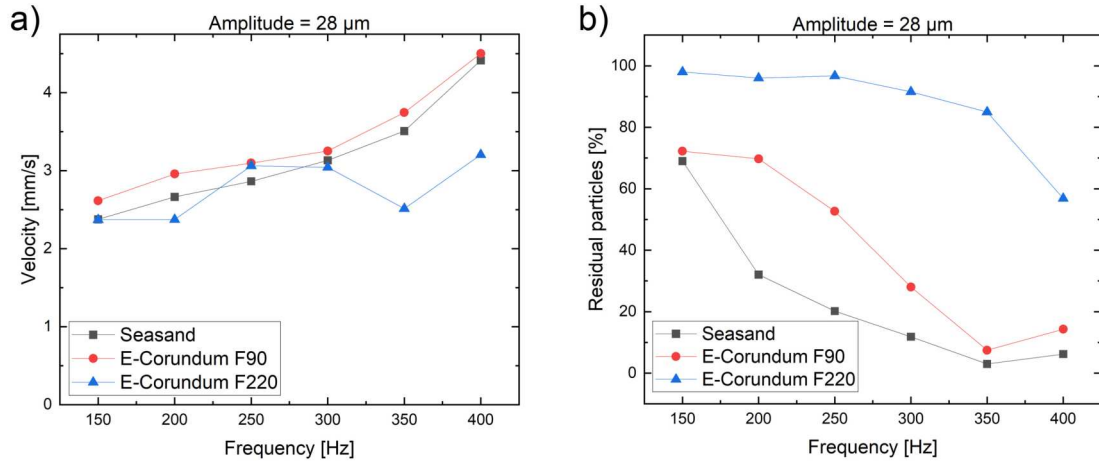
Figure 5.6: The average velocity and the residual particles left on the sample 33-180 after one minute for different frequencies and different particle sizes. Larger particles (Seasand) move faster and are cleaned off the surface better than smaller particles (E-Corundum F220).

5.3.3 Experiments on Moving Dust Particles on Sandfish Inspired Surfaces

The previous sections outlined the selection of samples and the choice of parameters of the vibration. The restriction to a frequency range from 150 Hz to 400 Hz with an increment of 50 Hz, two different amplitudes and two particle sizes on twelve samples still led to 288 individual experimental runs. These were each carried out as described in the previous sections.

Velocity of the Particles

The results, displayed in Fig. 5.7, support the assumption that particle velocity is proportional to frequency at least for the experiments with higher amplitude. Here the velocities of both seasand and e-corundum increase nearly continuously with frequency; from around 2.5 mm/s at 150 Hz up to 9 mm/s at 400 Hz. Sample 33-235 stands out, because it is among the fastest for each frequency for both seasand and e-corundum and particularly for frequencies above 300 Hz with e corundum much higher speeds are reached compared to the other samples. Amongst these other samples none stands out significantly and there is no significant difference in particle speed between the different particle sizes.

On the other hand, for the amplitude of 14 μm the particle velocity does not change with frequency at all; the average velocity is always around 2.5 mm/s to 3 mm/s. One remarkable value is the sample 08-80 at 400 Hz, amplitude of 14 μm with seasand (Fig. 5.7b). Repeated runs of this exact setup did not replicate the unusually high velocity at this setting, therefore it has to be disregarded as an outlier in the original measurement series.

To better compare the results of these experiments, an average curve was calculated
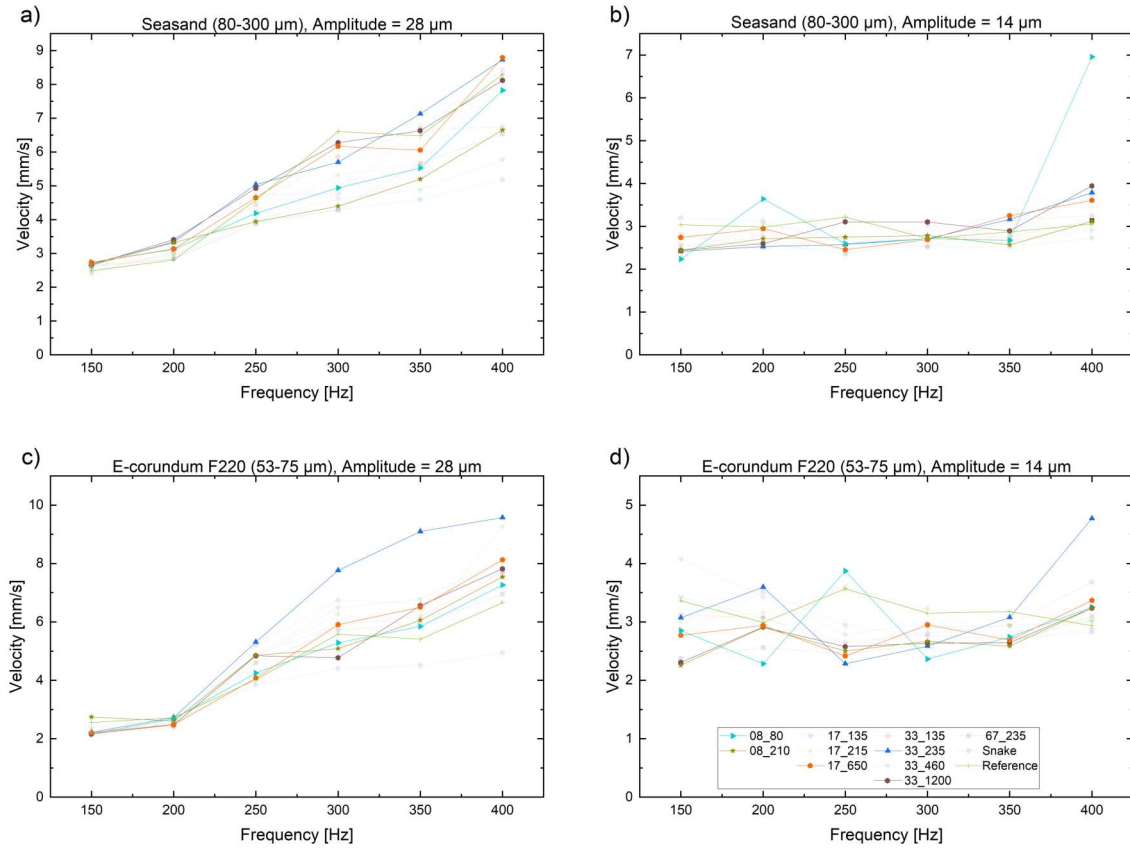
Figure 5.7: The average velocity of particles on the different samples for seasand (**a** and **b**) and e-corundum F220 (**c** and **d**) for two amplitudes respectively. For an amplitude of 28 μm the average velocity of the particles increases with frequency. For the lower amplitude this trend cannot be observed.

for each of the four setups (Seasand and e-corundum with two amplitudes respectively). Figure 5.8 shows these average curves and a linear fit applied to each curve. There is a positive correlation for velocity and frequency for an amplitude of 28 μm, while for the lower amplitude of 14 μm there is no correlation between particle velocity and frequency. The influence of particle size on the speeds of the particles is negligible.

It has to be noted that for all four settings the snake scale replica is almost always one of the 'slowest' samples. This might be explained by the scratches and dents that are present in this sample due to its natural origin. Since there is very little literature on dry self-cleaning using anisotropic friction, a comparison with other studies is difficult. However, the assumption that higher step height, which leads to higher friction anisotropy [45], would lead to faster moving particles could not be confirmed in this study.
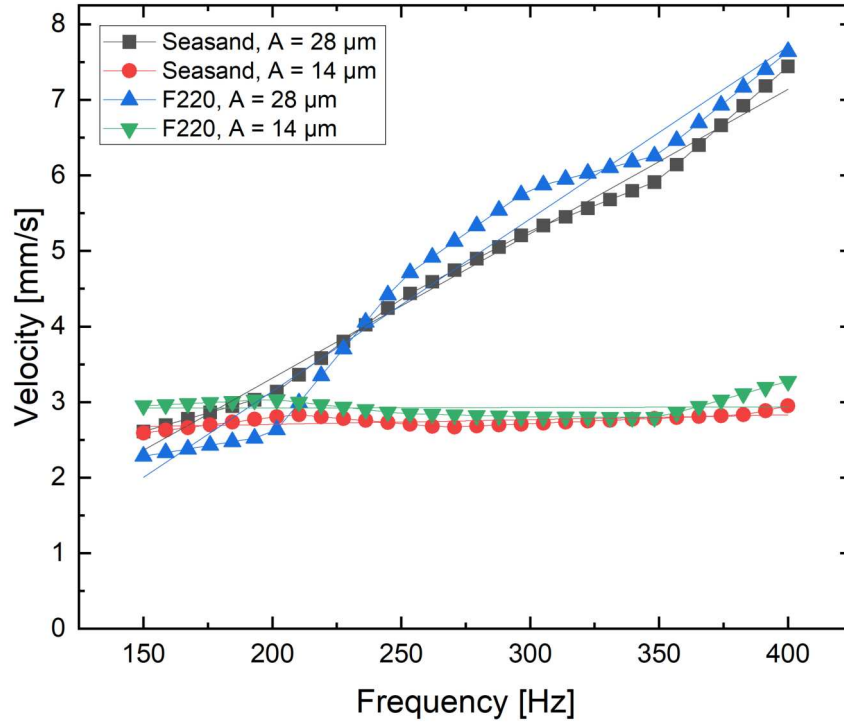
Figure 5.8: The averaged velocity curves for two particle sizes and two amplitudes. There is a strong positive correlation between frequency and particle velocity for an amplitude of 28 μm but not for an amplitude of 14 μm.

Residual Particles

Figure 5.9 shows the percentage of residual particles left on the sample one minute after activating the vibration at the respective frequency and amplitude. The general trend is, that higher frequencies lead to less residual particles left on the sample. For some of the samples the number of residual particles drops significantly when exceeding 300 Hz. Many other samples have a peculiar dip where the least amount of residual particles is achieved somewhere around 300 Hz. This dip reappears in Fig. 5.10, where all curves of residual particles have been averaged. A similar behaviour will be observed with regard to directionality as shown in the next section.

The experiments show that seasand, containing larger particles (80 - 300 μm), is cleaned off the surface much more easily than e-corundum F220 (53 - 75 μm with its much smaller particles. As expected, a lower amplitude of the excitation leads to slower movement of the particles and therefore to more residual particles left on the sample after one minute of vibration. Especially the combination of the lower amplitude and small particles leads to over 85% of particles being left on all samples. The flat reference sample has a relatively large amount of residual particles for all frequencies, supporting the claim that sandfish inspired surfaces can actually aid in cleaning solar panels more effectively. While the velocity of the particles on the flat sample is in fact similar to the particle speeds on the structured samples (see previous chapter), the particles do not move in a directional
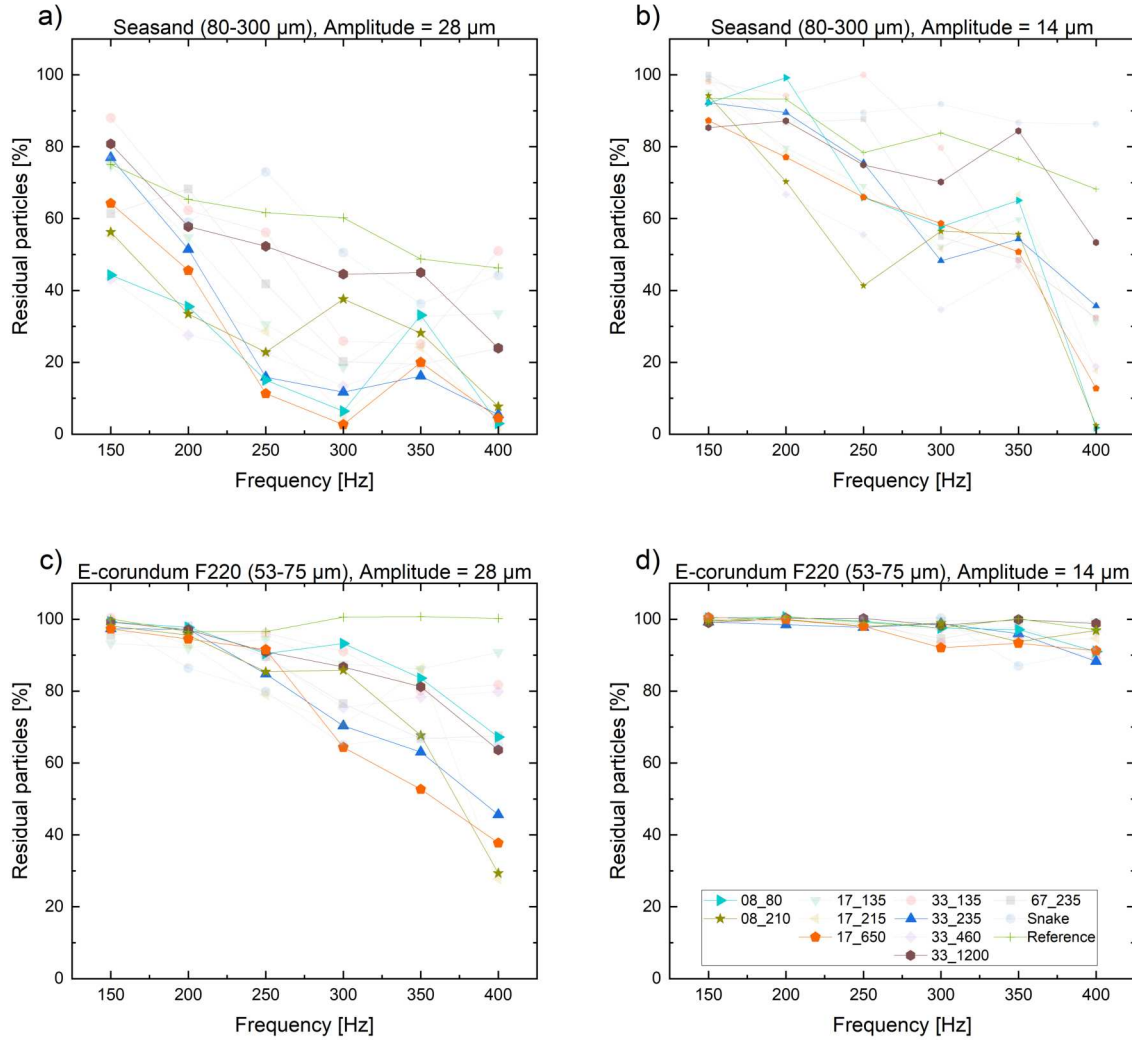
Figure 5.9: The residual particles left on the samples for seasand (**a** and **b**) and e-corundum F220 (**c** and **d**) for two amplitudes respectively. Higher frequencies lead to less residual particles, as can be expected. Smaller particles require higher amplitudes to clean the surface properly.

motion, but move randomly around on the sample, often changing direction. Therefore more are left on the sample after one minute. As is the case with particle velocity, the snake scale replica also performs relatively poorly in terms of residual particles in all four setups. This is again likely explained by the scratches and dents in the surface.

To visualize the rate of particle removal, Fig. 5.11 displays plots of the residual particles over time. This can only be displayed for one frequency at a time; here 300 Hz was chosen. For better clarity, some more interesting graphs have been highlighted. Especially for seasand with an amplitude of 28 μm there are two groups of curves. Some samples show an exponential decrease in residual particles while for others the number decreases in a linear fashion. The samples that scored particularly well in the absolute number of
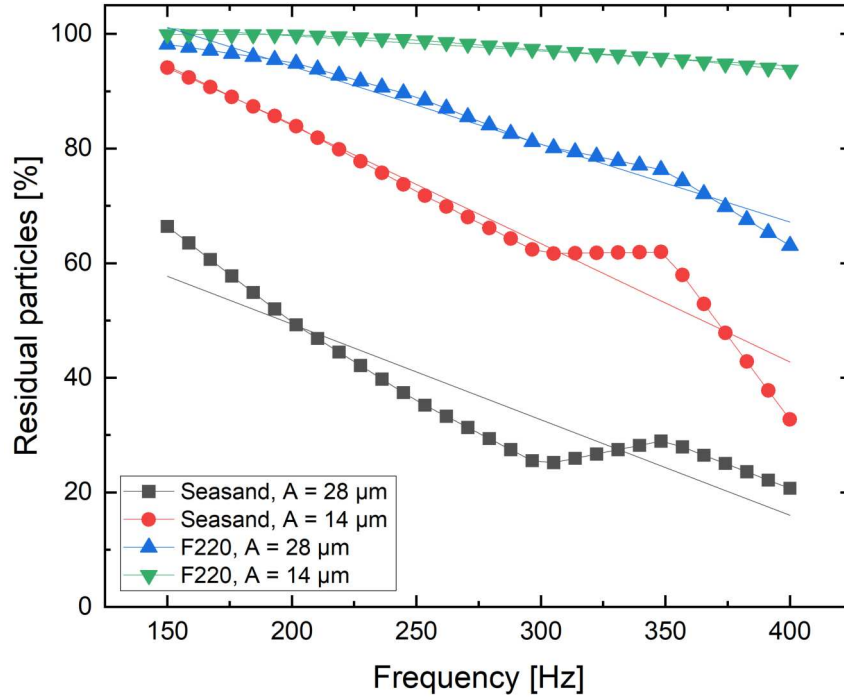
Figure 5.10: The averaged residual particle curves for two particle sizes and two amplitudes for all samples, respectively. There is a negative correlation between frequency and residual particles. Seasand is cleaned off more easily than the smaller e-corundum particles and that a higher amplitude leads to better cleaning of the samples.

residual particles (Fig 5.9) do not just have a steeper linear curve but show a very high rate of particle removal especially in the first seconds. Samples that scored worse in residual particle numbers seem to have a more linear decline. For seasand with a lower amplitude and e-corundum with the high amplitude the same trends can be observed although not as explicit. Since the residual particle values for e-corundum with an amplitude of 14 μm are generally very high, no meaningful diagram can be plotted for this setup.

Interestingly, for three of the four combinations of particle size and amplitude (seasand at both amplitudes, e-corundum at the high amplitude) the same samples seem to perform rather well. These are the samples 08-80, 08-210, 17-650 and 33-235, which all have a different period as well as a different height. From these measurements it cannot be assessed clearly weather, for example, low (210 nm) or high (650 nm) microstructures lead to better cleaning of the samples. Interestingly the sample 33-1200 scores very poorly for each of the setups. This further disproves the hypothesis that higher microstructures lead to better cleaning.

Directionality

The directonality of the movement of the particles is an important characteristic in quantifying the effect of the sandfish inspired microstructures on the surface. Ideally all particles
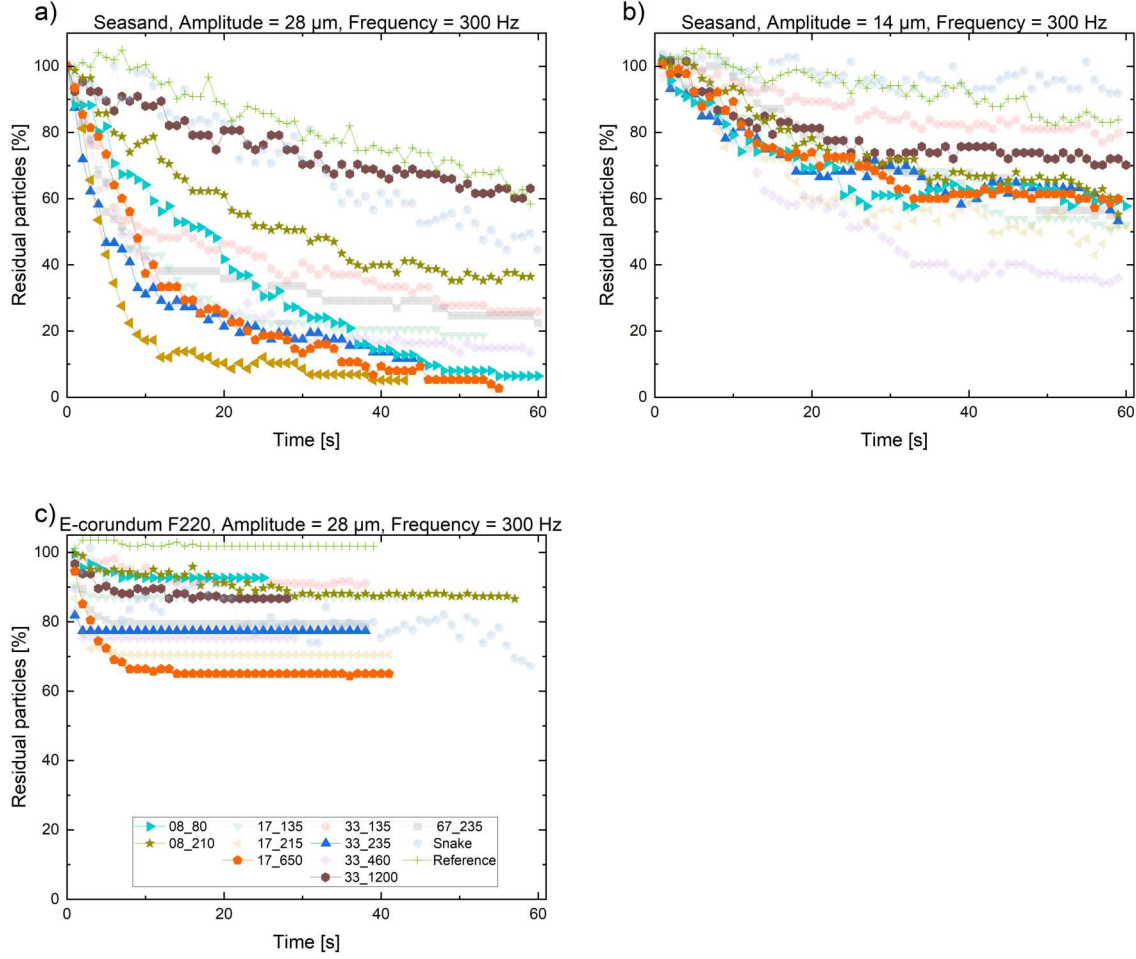
Figure 5.11: Residual particles over time. While some samples show an exponential decrease of particles on the sample, others show a linear decline in particle numbers. The samples with an exponential decrease are the ones that scored particularly well in the number of residual particles at the end of the experiment.

would move in the direction of the lower friction coefficient on a structured sample and wander randomly around a fixed spot on a flat sample. To measure this effect the software can determine the direction in which every particle moved in relation to the previous frame. We defended a directionality quotient as follows:

$$D = (\sum_0^{N_{frames}} \frac{N_{Up}}{N_{Down}}) * \frac{1}{N_{frames}} \tag{5.8}$$

where N_{up} and N_{Down} are the number of particles that have moved up or down in relation to the previous frame and N_{frames} is the number of frames of the video that is being analyzed. This way we got an average directionality quotient for each experimental setup. The samples are mounted on the vibration stage so that the particles should, in theory, move up on the structured samples. A directionality coefficient of one therefore means that

the particles are moving around the sample randomly, a value greater than one indicates movement up and a value under one corresponds to an, on average, downward movement of the particles.
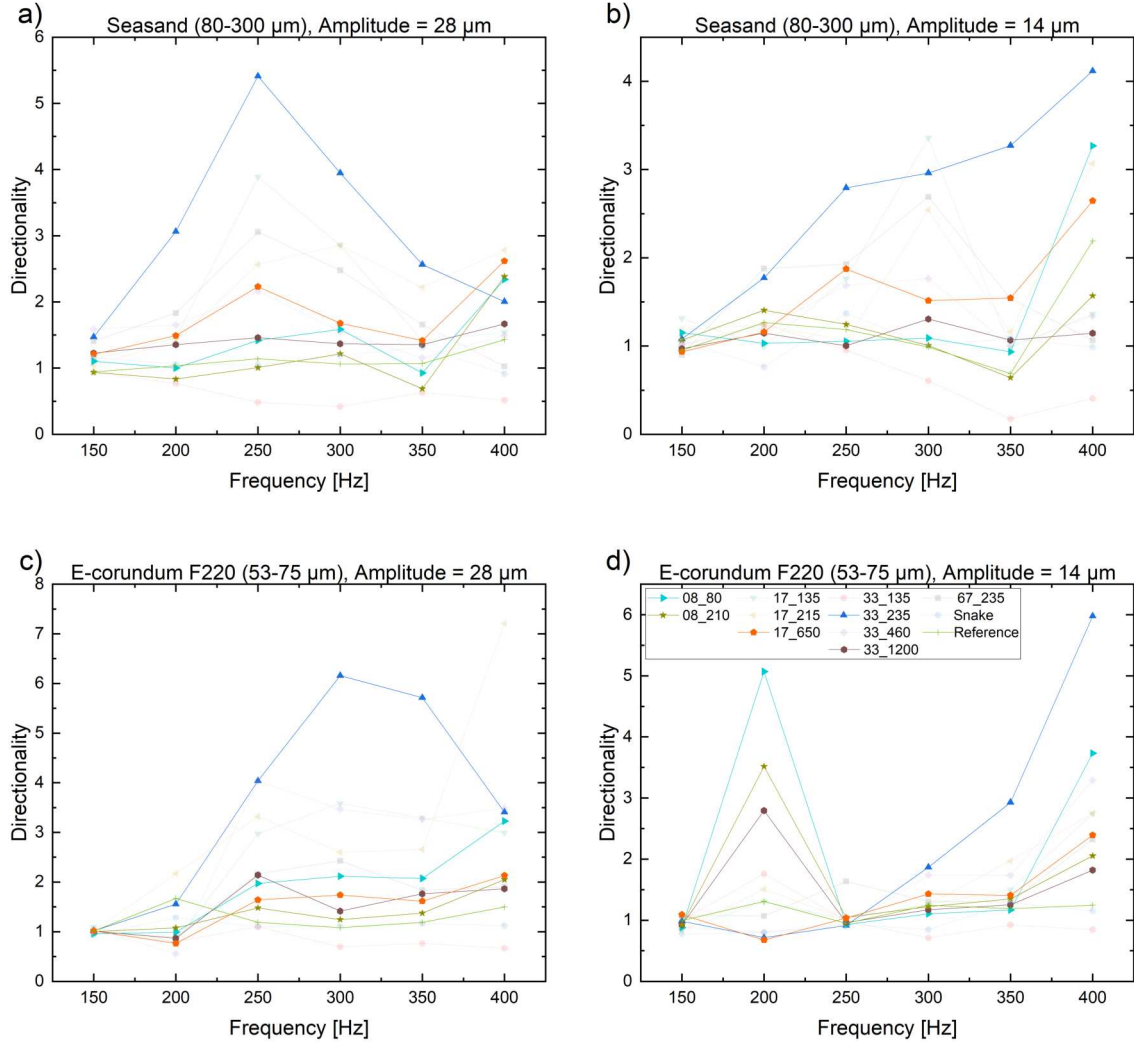
Figure 5.12: The directional ratio for seasand (**a** and **b**) and e-corundum F220 (**c** and **d**) for two amplitudes respectively. For some samples a peak in the middle of the frequency range is notable. For both seasand and e-corundum as well as for both amplitudes sample 33-235 stands out due to a very high directional ratio at least for part of the frequency range.

It is immediately noticeable that a few samples show a peak in the directionality coefficient at around 200 to 250 Hz. This is the case for each of the four setups. While this peak reminds of the dip in residual particles described in the previous section; it is located at slightly lower frequencies than the dip in residual particles. It is therefore unclear wether these two effects are correlated. Most samples show the expected directionality coefficient above one, while some samples reach a coefficient of over seven in some setups. The flat

sample has a coefficient of around one across all setups, which is also to be expected. Surprisingly the sample 3,3-135 shows a negative directionality coefficient for the experiments using seasand. An explanation for this unexpected behaviour was not found. The samples 33-235, 17-135 and 17-215 perform rather well for seasand at both amplitudes and e-corundum with the larger amplitude. These samples all have a similar height between 135 and 235 nm; the height of the microstructures alone can still not explain their performance since the sample 08-210 is also in a similar range regarding height and it does not perform particularly well.

Comparison to the Geometry of the Sandfish

As has been stated in the introduction to this chapter, the step-like microstructures found on the scales of sandfish have a periodicity of around 3 μm and a step height of around 200 - 300 nm. Figure 5.13 shows a comparison between all the samples with a step height of around 200 - 300 nm, in order to analyze the influence of periodicity. While the differences between the samples are by no means enormous, some observations can be made. All samples reach relatively similar average particle speeds, all samples show a peak in residual particles between 300 and 400 Hz and a peak in the directionality ration between 200 and 300 Hz. The sample with the lowest periodicity of 0.8 nm, 08-210, performs comparatively badly in all three measures, especially the directionality ratio is only slightly above one over most of the vibration spectrum. On the other hand the sample 33-235 scores rather well in all measures. Interestingly this is also the sample that resembles the sandfish most closely with a periodicity of 3.3 μm and a height of 235 nm.

Figure 5.14 shows a comparison of all the samples with a similar periodicity as the sandfish, so that the influence of step height can be evaluated. In terms of average particle speed there is a negligible difference between the samples. The samples with similar step height as the sandfish, 33-235 and 33-460, perform better throughout the entire frequency spectrum than both the sample with larger and smaller step height. For directionality two samples can be highlighted. Firstly, 33-135, that has a directionality ratio that is considerably below one for the entire frequency window, meaning particles move the other way than they are theoretically intended to do. This is the only sample in the entire set that showed this behaviour - a satisfying explanation was unfortunately not be found. The other remarkable sample is, again, 33-235, that has a directionality ratio of over five at 250 Hz, which is considerably larger than any other sample. However these results have to be treated with some reservation as the standard deviation, which for reasons of better clarity has not been plotted, is relatively high for many of these measurements.

Conclusion of the Particle Movement Experiments

In summary none of the tested geometries proved to be optimal for each of the tested conditions. However, some general trends regarding the optimal vibration parameters and properties of the microstructures were found:

- The higher the frequency, the faster the particles move. Furthermore, more particles
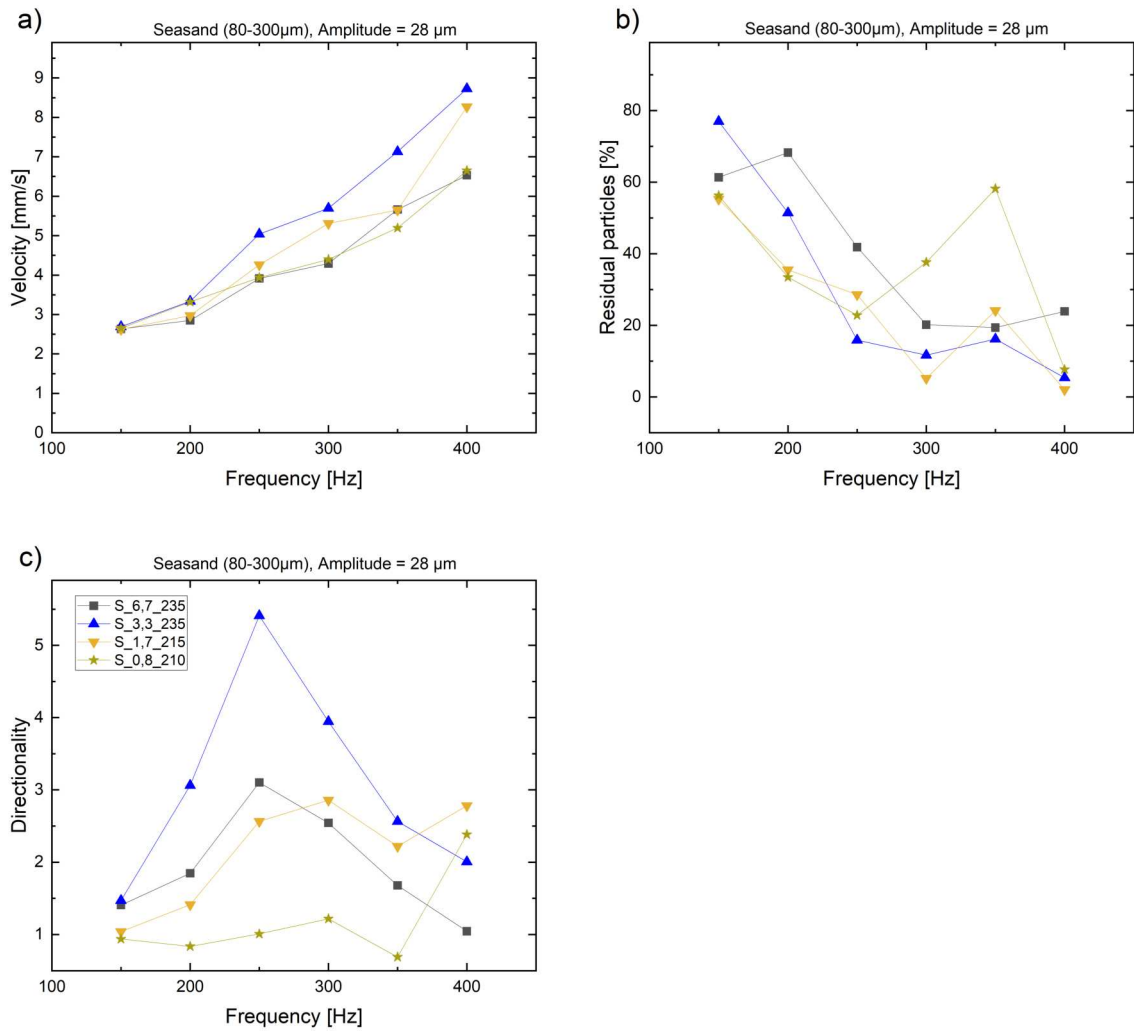
Figure 5.13: Comparison between the artificial sandfish inspired surfaces that have a height of 200 - 300 nm. Here the influence of the periodicity can be observed.

seem to move as the number of residual particles reduces with increasing frequency.

- The larger the amplitude the faster the particles seem to move and fewer residual particles are left on the sample.

- The directionality ratio peaks between 200 and 300 Hz for many samples.

- Larger particles move more easily and faster than smaller particles.

- Step height does not influence the speed at which particles move nor the number of residual particles.

- Curiously the samples that seemed to perform the best are not the ones that have the highest friction anisotropy measured with an AFM.
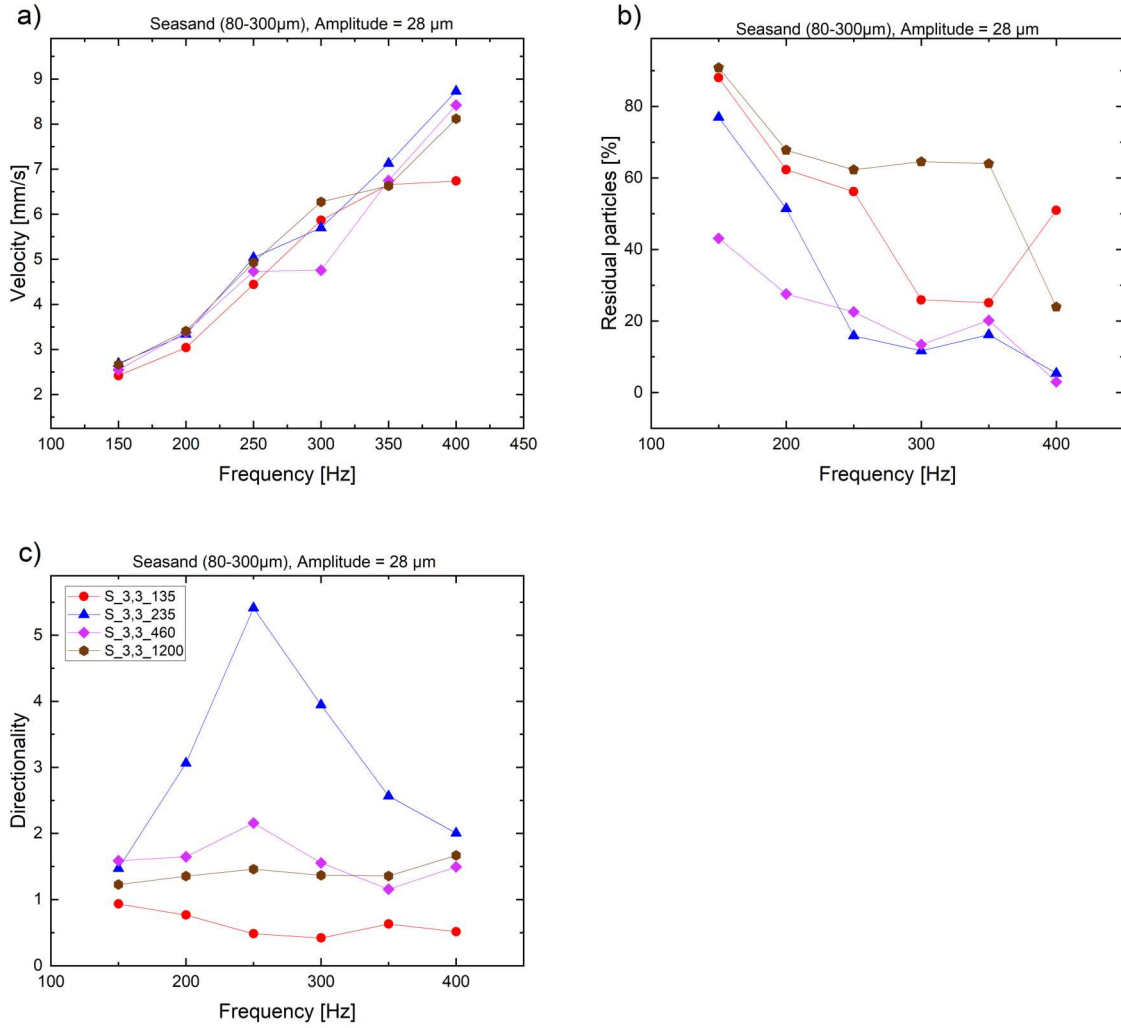
Figure 5.14: Comparison between the artificial sandfish inspired surfaces that have a height of 200 - 300 nm. Here the influence of the periodicity can be observed.

While it is difficult to select a single geometry that performs well under all circumstances, sample 33-235 performs reasonably well in most experimental runs and exceptionally well in a few. Interestingly this sample is very close to the geometry of the sandfish structures with a step height of 235 nm (sandfisch $\approx$ 200 - 300 nm) and periodicity of 3.3 μm (sandfish $\approx$ 3 μm [46]). Curiously this is not the sample with the highest friction anisotropy measured by AFM, its anisotropy is actually well below that of others of the chosen sample. The reasons for this surprising finding are yet unknown as this behaviour is very counter-intuitive. The samples with larger structure height have a higher average friction (in both directions) which might impede or slow down particle movement. Typically these samples tend to also show higher friction anisotropy. There might be a sweet spot between high anisotropy and low average friction where the samples geometry leads to optimized particle movement.

Obviously the optical gratings are very different from the sandfish scales in many ways.

Firstly the gratings are very regular and therefore diffract the light, which becomes visible in the form of rainbow colors on the sample surface when viewed from certain angles. This is not necessarily a disadvantage as there are several approaches that make use of diffraction gratings for optimizing photovoltaic panels [185]; although not all place the gratings directly on the surface of the panel. Also the gratings do not have the micro fibrils at the edges that the steps of the sandfish have. When compared to the geometry of the microstructures found on snake scales, the difference between the straight edges of the grating and the finger-like structures found on snake scales becomes even more obvious. Furthermore the gratings used for the experiments described above were coated with a thin film of aluminium which is obviously a very different material than the polymer or glass surfaces that would most likely be used on solar panels or the keratin that the original sandfish scales are composed of. Nevertheless these experiments show that it is possible to use anisotropic friction created by sandfish inspired microstructures to move dust particles in a specific direction.

5.4 Field Test of Sandfish Structures on Solar Panels

In order to quantify the improvements that sandfish inspired coatings for solar panels can provide a field test was conducted. Thin PMMA sheets covered in sandfish like structures were laminated onto small solar cells. These were then connected to a sensor unit that measures the power of the solar panels as well as environmental data, so that the performance of the coated and uncoated panels can be compared. The components for the setup were chosen in a way that kept costs low in order to enable the setup to be recreated in many different parts of the world to study the behaviour of sandfish coatings in different places and climates in the future.

Experimental Setup for Sandfish Field Tests - "Sensor Box"

The so-called sensor box consists of a main adapter, a housing for the main electronics, several housings for different sensors and connector cables for up to five solar panels. Furthermore smartphone vibration motors are attached to the solar panels to create the excitation needed to move the particles on the surface of the panels. A ESP32 (ESP32-WROOM-32) system on a chip microcontroller is used as a main data processing unit. This chip can be programmed in C and is equipped with a large number so-called GPIOs (General Purpose Input Output) pins. For communication with sensors it provides two I2C buses as well as the SPI protocoll. Attached to it is a real time clock module (DS3231) to provide accurate time to the ESP32 as well as a SD-card adapter that accepts standard micro SD cards as data storage medium. Data can be written directly onto the SD card using SPI. The following environmental sensors are connected:

- Temperature/Humidity: BME280, Humidity 0-100%, temperature 40-100. The sensor is mounted under a 3d-printed Stevenson-screen.

- Rain: AZ-Delivery rain sensor module. This module can detect moisture on the sensor plate, it cannot detect the amount and exact duration of rain.

- Luminosity: BH1750, measurement range: 0-65535 lx. The sensor is mounted in an enclosed housing with a transparent PMMA plate to protect it from rain.

- Dust concentration: Grove dust sensor V1.0. The sensor is mounted in a housing with gratings on the sides to protect it from water.

- Solar power: 5x INA-219, voltage 0-26V, current max. 3.2 A. The sensor works via a 0.1 Ω measurement shunt.

- Relays: 4x SRD-05VDC-SL-C. These relays are used to control the activation of the vibration motors attached to the solar panels.

While the absolute accuracy of these low cost sensors is certainly disputable, these measurements can still give a good idea of the kind of conditions in which the solar panels were operating. The advantage of using readily available and extremely low cost sensors is, that a number of such sensor boxes can be built by almost anyone with basic technical knowledge anywhere in the world to study the behaviour of sandfish inspired coatings for solar panels in a wide variety of climates. Readings of all the sensors are taken by the software in an interval of two minutes.

Solar Panels used for Sensor Box Experiments

The solar panels used for the investigation of sandfish inspired coatings were TRU components POLY-PVZ-8080. This is a small polycrystalline solar module with outside dimensions of 80 x 80 mm^2. Open circuit voltage (Voc) was 6 V and the short circuit current (Isc) 0.126 A, which gives the module a maximum power (P.max) of around 6 W, with a specified tolerance of ± 5 % [186].

The sandfish inspired coatings were manufactured in a similar fashion to the process described in Chapter 4.4 via UV imprinting in PMMA. The backside of the PMMA was then milled flat until the total thickness of the piece was 0.7 mm. To ensure comparability flat pieces of PMMA were milled down to the same thickness. These, structured as well as the unstructured, PMMA pieces were then laminated onto the solar panels using Norland Optics NOA 68 UV-curing optical adhesive. After applying a thin coat of the adhesive the PMMA pieces were laid on by hand in an opposite peeling motion. Afterwards any remaining air bubbles in the adhesive were pushed out leaving only a small quantity of glue in between the panel and its PMMA coating. The adhesive was then hardened for 30 minutes under an UV lamp (280-400 nm, 16.6 W, distance: ≈ 10 cm). PMMA has a very high transmittance of over 90 % of light from a wavelength of around 350 nm well into the infrared regime [187]. Similarly, the adhesive has a transmittance of nearly 100 % for wavelengths over 450 nm [188], which is perfectly suitable for solar applications, since most solar panels operate in the range of visible light above 450 nm.

On the backside of the solar panels vibration motors were glued in place using a thermoplastic hot melt adhesive. The motors used were of similar make as the ones used in the experiments described in Chapter 5.2. Five individual motors were glued to each panes to achieve sufficient vibration amplitudes. To protect the motors from rain and moisture, the panels were glued onto a small wooden holder. One of the sensor boxes built was deployed on a roof at the KIT, the other was used in an artificial indoor setup in the lab. Figure 5.15 shows the respective setups.
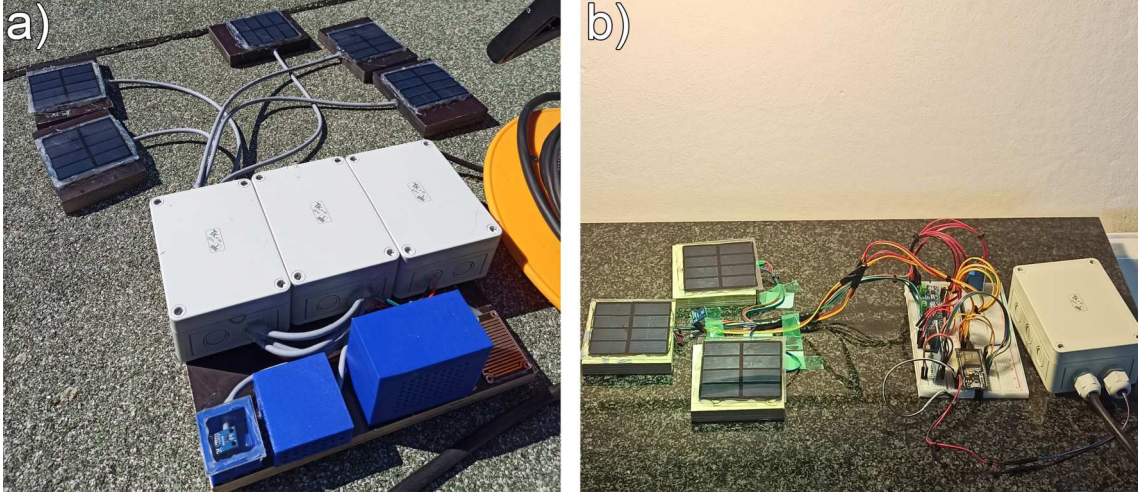
Figure 5.15: Experimental setups for the field and lab tests of solar panels with sandfish inspired coatings. **a)** Outdoor setup placed on the roof of the IMT. The solar panels are connected to the electronics housed in the grey boxes. The sensors collecting environmental data are placed in the blue housings. **b)** Simplified setup for lab tests. The sensors for environmental data have been removed. The lab tests were conducted under a daylight lamp with a power of 300 W suspended approximately 1 m above.

Laboratory Tests of Reptile Structures on Solar Panels

To gain more experience on the practical efficiency gains that sandfish inspired solar coatings might provide, a simple laboratory demonstration was set up. A simplified version of the sensor box used outdoors with only a temperature and humidity sensor and a brightness sensor as well as three INA219 current sensors was built. Connected to the current sensors were three photovoltaic panels, two with a flat sheet of PMMA and one with the structured PMMA coating. One of the flat samples served as a stationary reference while the other two panels had vibration motors attached and were set to vibrate for 30 s every 180 s. This setup was placed underneath a 300 W daylight lamp, which was suspended approximately 1 m above. A mixture of different grain size sands (50 - 160 μm) was applied every 30 minutes, simulating an extremely dusty environment. The amount of dirt applied to each panel each time was measured using a small measuring spoon. The dirt was rippled onto each panel from a height of 30 cm, so that the sand particles spread evenly over the surface of the panel. While not perfectly precise, the total number of dust applications on each panel (56 over the 28 h observation period) assures that small variations in the amount of dust actually reaching each panel should average out. The amount applied to the panels would most likely correlate to the amount of dust that a solar panel in the field would experience in many weeks or months. The data show that, as it was expected, the power of the non-vibrating, flat reference sample decreases in an exponential fashion. At the end of the observation the power output of the reference sample is only about one fifth of the initial power, which is surprising as the panel was entirely covered by a relatively thick layer of dust. As more sand was added, the power would eventually go to zero. On the other hand the vibration of the other panels keeps them relatively clean and thereby efficient. The linear fit applied to the curves of the vibrating panels reveals that the power of the sandfish sample does not decrease significantly over the whole observation period. The flat sample experiences a slight decrease in power output over time. The slope of the linear fit applied to the power curve of the flat panel is -0.04854 mW/h, which accumulates to about 5 % efficiency lost at the end of the experiment. While this might seem like a marginal decline when compared to the large decline of the stationary panel, one has to keep in mind that the sandfish coated panel did not experience any significant loss of efficiency. This indicates, that while flat vibrating panels would have to be cleaned less frequently than stationary panels, the sandfish coated panels would have to be cleaned almost never.

To put this into perspective a small calculation example can be given. Assuming the amount of dust applied to the panels in this artificial setup corresponds to the amount of dust that a panel in the field would be exposed to in six months. Then the sandfish coated panel would still experience only a minimal loss of efficiency, while the unstructured, vibrating panel would experience a loss of efficiency of roughly 0.035 % per day, which is comparable to the average daily efficiency loss of solar panels placed in California (0.05 %) [189]. The stationary reference panel would experience a loss of efficiency of about 1.57 % per day. The following formula is given in literature to estimate the most economical time
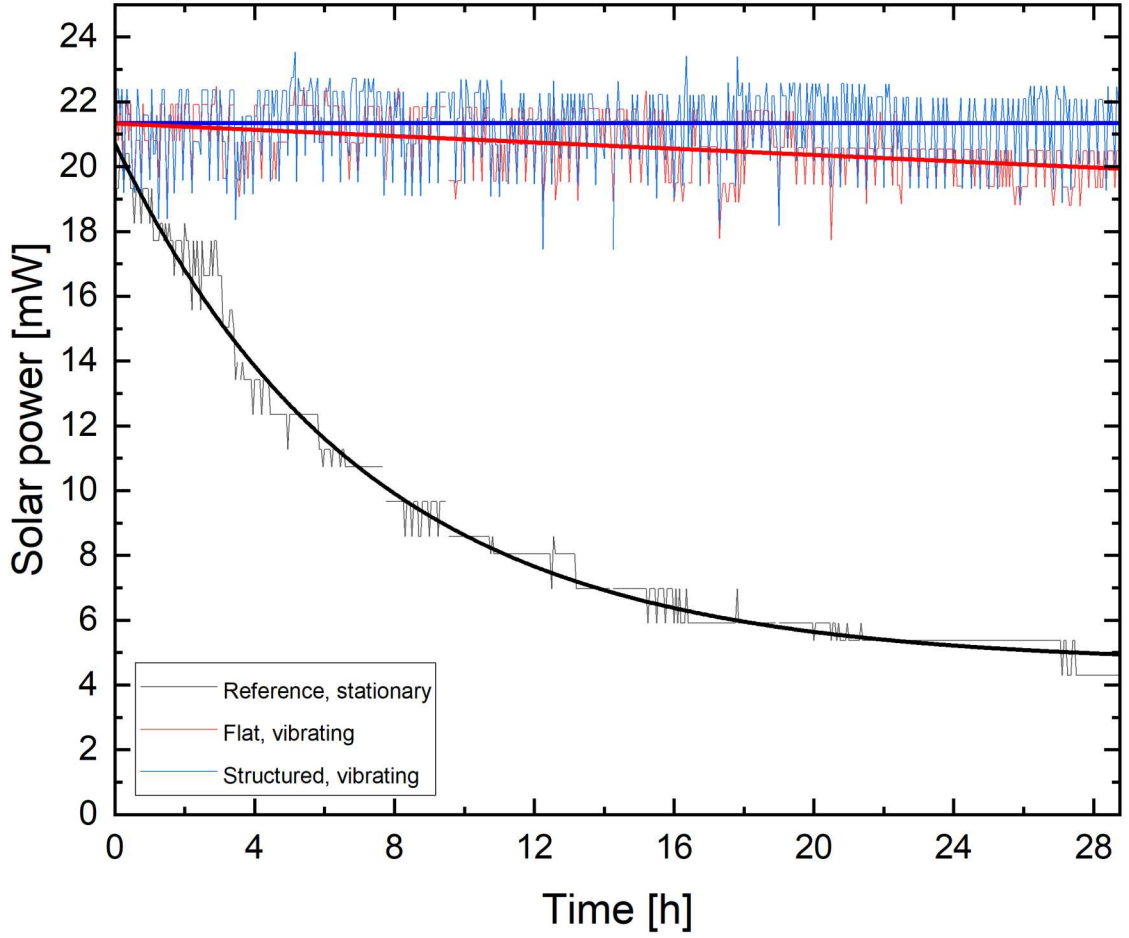
Figure 5.16: The solar power of the three panels (flat, non-vibrating reference, flat vibrating and sandfish-coated) over time a time period of 28 h. Every 30 minutes an equal amount of sand particles was spread over each of the panels. The power of the reference panel is quickly diminished while the vibration keeps the other panels reasonably clean. This experiment showed, that a sandfish inspired coating can provide a benefit.

interval in between cleanings of solar panels [190]:

$$N = \sqrt{\frac{2 * C}{\alpha h P \beta}} \qquad (5.9)$$

where N is the number of days between cleanings, C is the cost of cleaning the solar panels, α is the daily loss of efficiency, h is the average hours of sunlight, P is the power of the installed panels in kW and β is the price of electricity per kWh. Assuming the cleaning of a 1 MW solar farm costed 500 €, the panels experienced 8 h of sunlight a day and the price per kWh was 0.2 €, the reference panel would need to be cleaned every nine days, whereas the flat, vibrating panel would need to be cleaned roughly every 60 days. While that is an immense improvement, this would still be six cleanings needed every year which amounts to fictional costs of 3000 € per year. These costs would be eliminated by

the sandfish coatings. This small example demonstrates that the seemingly small benefit that the sandfish coatings provide, will accumulate over time and can actually have a noticeable real world effect. This is further illustrated in Fig. 5.17. Since polymer film is comparatively inexpensive, the sandfish coatings will not add much cost to the overall price of the solar panel. Therefore, even if the sandfish coated panels were cleaned once a year, the savings of just one year would most likely make up for the additional costs of the sandfish coatings.
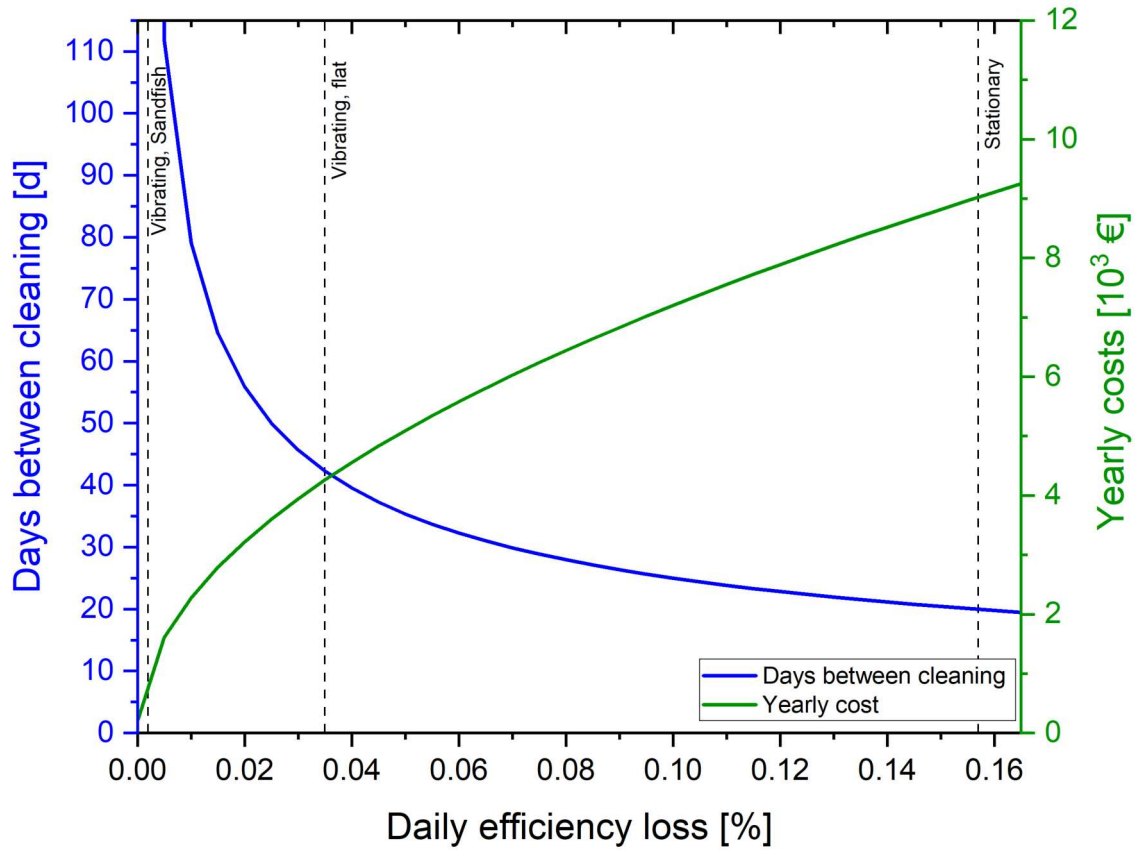
Figure 5.17: Optimum cleaning interval according to [190] and the associated yearly cost for the calculation example given above (C=500 €, P=1000 kW, h=8 h, β=0.2 €). The dotted lines represent the daily efficiency loss that the test panels experienced in the laboratory test setup. For the sandfish-coated panel a real-world loss of efficiency of 0.001 % per day was estimated. Just the vibration leads to a significant improvement of the cleaning interval. The additional improvement in daily efficiency loss that the sandfish coatings lead to seems small when compared to the improvement of just the vibration. The improvement in cleaning interval and costs that this improvement leads to is, due to the nature of the plot, quite significant.

Field Tests of Reptile Structures on Solar Panels

The setup for the field test of sandfish inspired coatings consisted of five solar panels, four of which were able to vibrate; one served as a stationary, unstructured reference sample. Of the four vibrating panels two, one structured and one flat, were vibrating for 25 s every 75 s, the other two, again one structured and one flat sample, were vibrating for 25 s every 150 s. This was done to gain insight into the time the panels need to vibrate in order to achieve a sufficient cleaning effect. Table 5.2 gives an overview over the five samples and their respective labels.

Panel name	Microstructure	Vibration	Interval
Stationary reference	None	None	None
Flat, short	None	25 s	75 s
Flat, long	None	25 s	150 s
Structured, short	Sandfish	25 s	75 s
Structured, long	Sandfish	25 s	150 s

Table 5.2: The solar panels used for the field test of the sandfish inspired coatings. One sample served as a flat, stationary reference. The other samples were vibrating for 25 s in intervals of 75/100 s. For each vibration interval - short and long - a structured and a flat sample were used.

The setup was placed outside on the roof of the IMT from August 30th to October 30th 2023 - a total of nine weeks. The roof is mostly flat and the panels were laid flat as well. From a solar efficiency standpoint, this is not ideal as photovoltaic panels produce the most power when the incident angle of the light is perpendicular to the surface. However since the sun is almost vertical at the equator, where most of the envisioned areas of operation are, and since we wanted to rule out any cleaning effects due to tilt, this flat orientation was chosen. The roof is in direct sunlight for almost the entire day except around noon, when the shade of a nearby tree falls onto the setup for a couple of minutes and in the very evening when the shade of a nearby building reaches the roof. Sensor readings were taken every two minutes and the data was saved to the SD card. This led to a total of over 750,000 individual data points being collected. Analysis of the data points reveals an expected pattern, where solar power increases during the day; when the shadow of the nearby three falls onto the roof there is a loss of power, as is when the shadow of the building falls onto the panels in the evening. The solar power data matches the data recorded by the illuminance sensor. Temperatures reach a maximum of 50 °C on a very hot and sunny day and near 0 °C during one particularly cold night. The extreme temperature variation can also be seen in the humidity, that decreases as the illuminance and therefore temperature increase and often reaches 100 % during the night. This led to condensation on the panels

in the morning. Thus the rain sensor often indicated rain, although the weather during the experiment was exceptionally good with almost no rainfall except for the last week of the observation. At the end of the experiment one can see that the maximum power produced by all panels decreases significantly, which is most likely caused to great extent by the lower incidence angles and less solar radiation reaching the panels during fall season.

Figure 5.18 shows the solar power of all five panels over time as well as the data of the other environmental sensors. Since the time of observation was nine weeks long, it is difficult to make out any differences between the power output of the panels. Thus in Fig. 5.19 two periods of three days at the beginning and at the end of the observation period were plotted separately. Unfortunately, no significant difference between the sandfish-coated and flat panels can be observed. There also appears to be no difference between the vibrating panels and the stationary reference. This is true at the beginning of the observation period, which would be expected, as well as at the end, where a loss of efficiency of at least the reference panel would have been expected. All panels showing nearly identical performance might be due to environmental factors such as the large amounts of condensation that formed on many mornings or occasional rainfall. In the climates in which the sandfish coatings are envisioned to operate this would be a rather uncommon occurrence. Another hypothesis would be that the observation period of nine weeks was too short for relevant amounts of dirt to accumulate on the panels, given the comparatively low dust climate that these tests were conducted in. Therefore, further experiments in other locations with different climates should be conducted. Due to time constraints this was unfortunately not possible in the course of this thesis. The sensor box developed in this thesis can be built with relatively low costs by anyone with basic technical knowledge. Therefore, building multiple of these boxes and sending them to partners all over the world is feasible and will hopefully lead to a better understanding of the benefits that sandfish inspired coatings for solar panels can provide in the field.
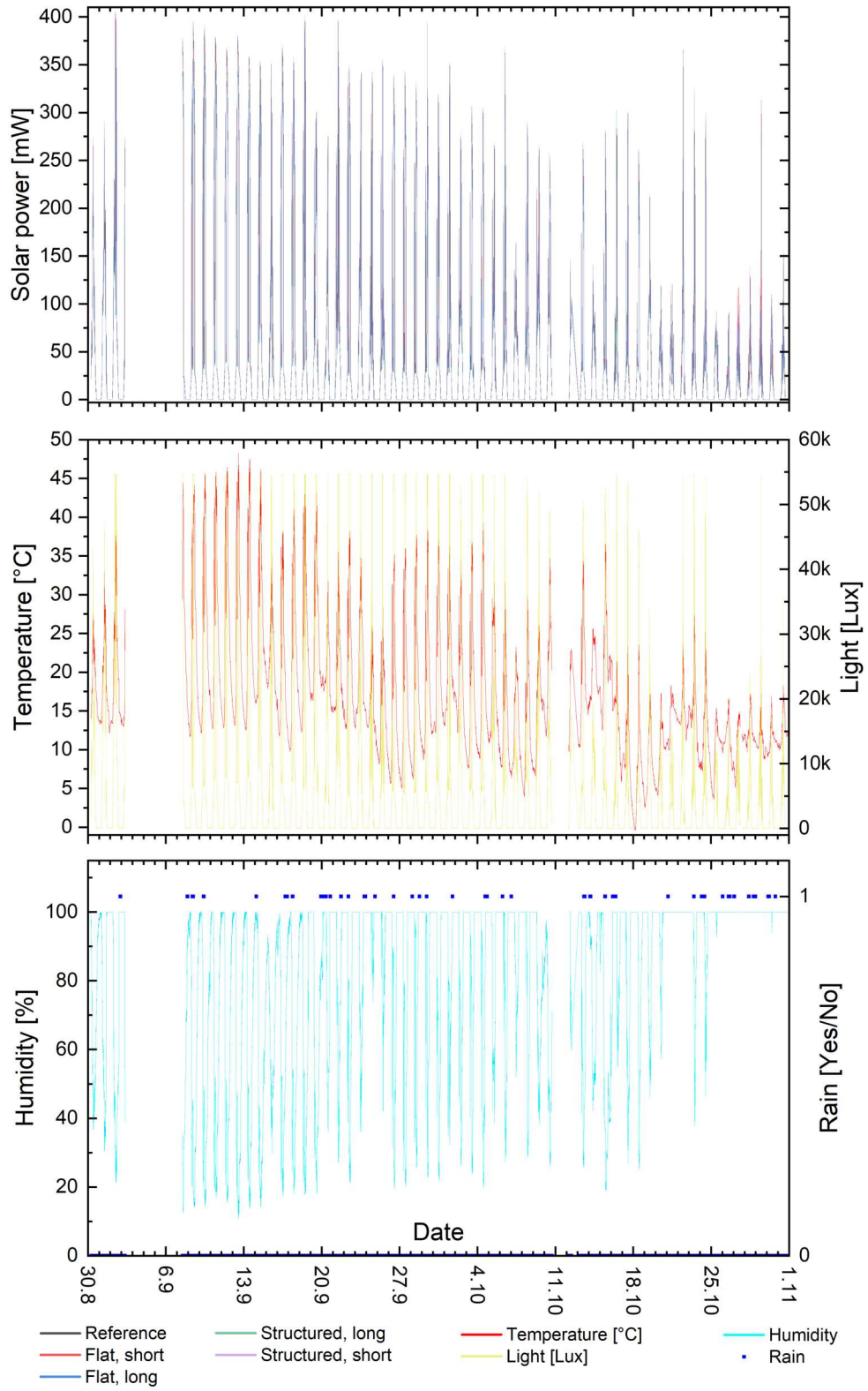
Figure 5.18: The solar power of the panels (non-vibrating reference, vibration sort interval, vibration long interval, structured and unstructured respectively) as well as illumination, temperature, humidity and rain over time.
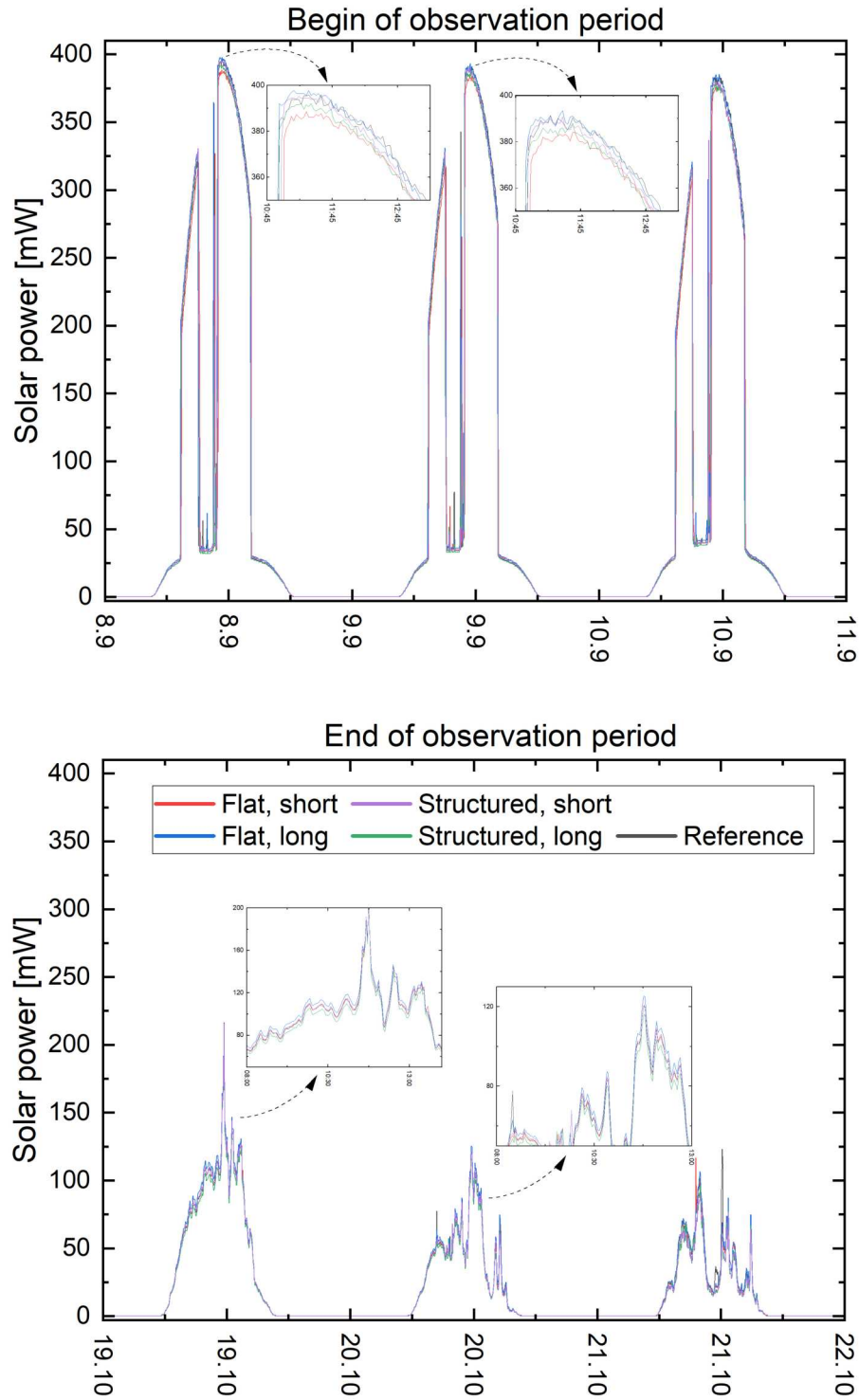
Figure 5.19: Detailed view of a section of the observation period at the beginning and of the end of the of the experiment. Throughout the entire observation period there is no significant difference between the coated and flat panels - not even between the vibrating panels and the stationary reference. This might be due to environmental influences like wind and rain or possibly the observation period being too short, given the relatively low dust local climate.

Chapter 6

Conclusion and Outlook

As outlined in the introduction in Chapter 1, this thesis targeted to answer the following three research questions:

1. Is roll-to-roll hot embossing useful for large scale production of biomimetic surfaces?

2. Can a combined extrusion and embossing roll-to-roll process yield precise microstructures and improve upon existing roller embossing processes?

3. Can this process be used to imprint large scale sandfish inspired surfaces and, if so, do these surfaces provide real world benefits to the solar industry?

In order to answer the first question, a superhydrophobic biomimetic surface - the so called nanofur - was produced in a roll-to-roll process. For that, the batch wise process previously used to produce nanofur, was transformed into a roller based process. A notable process parameter is the very low embossing force of only a few newtons, which leads to high contact angles of $> 150°$. The contact angle of the nanofur does not decrease significantly, even after more than 50 m of film had been structured. The roller process was then further adapted by the use of a coextruded support layer to produce thin (200 μm) polymeric nanofur. Thus, we were able to produce many square meters of polymer film covered with this interesting microstructure. By producing large area nanofur, we proved the scale-up potential of roll-to-roll hot embossing for the replication of biomimetic surfaces. To furthermore demonstrate the practical usefulness and possible of applications of nanofur, an exemplary product - the nanopads - were produced. These might serve for oil spill cleanup by separating oil and water using the hydrophobicity and oleopilicity of nanofur. Other applications of this surface are manifold and industry partners might take on the further development. To increase throughput wider rollers or faster roller speed can be used. Increases in roller speed are rather limited as the roller temperature must also increase in order to melt a sufficient quantity of material. Pre-heaters might mitigate this problem, but in general the use of wider rollers seems to be the more promising route. Wider rollers might make precise adjustment of the roller's gap, which is one of the most important parameters in nanofur production, more challenging. Further research should also be conducted on the old polymer residue left on the roller, since resurfacing the

roller each time the machinery stops is not feasible. These challenges seem to be solvable engineering problems. One has to consider though that the process used to manufacture nanofur - so-called hot pulling - is special as it can only be used to manufacture this specific structure. Arbitrary surface designs cannot be manufactured using this process.

In order to answer the second question, a more universal roll-to-roll hot embossing process that improves upon existing roll-to-roll hot embossing techniques was established. We call this new process "direct roll-to-roll embossing" since nano- and microstructures are embossed directly into newly extruded polymer melt as opposed to already existing polymer stock. This approach provides some benefits such as longer mold filling time, cold demolding and little sensitivity to variations in roller speed. To verify the theoretical benefits and optimize the direct embossing process, various test structures were fabricated and imprinted, varying the numerous process parameters using statistical design of experiments. This showed that the the screw speed of the extruder and the roller speed have negligible influence on structure quality, as long as both are set in an appropriate relation to one another, that is, there is sufficient material flowing out of the extruder nozzle to avoid macroscopic defects in the film. The melt temperature has a small influence on structure height and should be set as high as possible while still keeping the rheological characteristics of the melt in an appropriate range for extrusion and roller processing. An increase in embossing force leads to less rounded edges and less height loss from mold to imprint. It furthermore enables smaller structures ($< 4 \mu$m diameter) to be imprinted. The temperature of the rollers must be set as high as possible as this also enables imprinting smaller structures and reduces height loss. If the roller temperature is set above a certain point, sticking effects can occur that damage the structures as well as impair the macroscopic film quality. With the process parameters set in this way precise microstructures of 1.6 μm height and about 4 μm in diameter were imprinted.

In order to be able to imprint any structure using this process, molds have to be manufactured and attached to the rollers. Molds usually come in the form of thin flat nickel shims. Thus, two attachment mechanisms were developed. The clamping mechanism uses very thin shims and enables a swift change of the mold, which is ideal if multiple different structures on different shims are to be imprinted. The sleeve attachment mechanism enables the use of steel sleeves as rollers. This reduces manufacturing costs for rollers, as only a new sleeve has to be manufactured for each new structure as opposed to a whole new roller. The sleeves are either structured directly or have a thin nickel shim spot welded onto them. Spot welding is a simple and fast method of attaching shims to the sleeves and is sufficient for most lab applications or if a seam in the structures is acceptable. More advanced welding techniques exist if a seamless imprint is required.

Increasing throughput to industrial levels by increasing the roller and screw speed of the extruder seems feasible as the process proved to be robust against variations in roller speed. Using wider rollers should be possible as long as the rollers are sufficiently stiff. Since the rollers are pressed firmly into the polymer melt and cast films usually have some variation in film thickness anyways, minor bending of the rollers might be acceptable. Using larger diameter rollers makes them stiffer and also increases the distance between imprints of

the seam area, if there is a seam in the mold. This is acceptable for applications where the film is cut in pieces anyways, for applications that require continuously structured film, a seamless mold has to be fabricated. Mold fabrication in general is challenging in roller hot embossing, as the molds have to be very large, when compared to classic P2P embossing. Typical micro fabrication tools work with wafer sized substrates, larger molds usually require stitching. Depending on the structures, mold fabrication might be very costly, especially for large rollers. Lastly the film extrusion process itself is considered to be challenging and sensitive to parameter variations, even for flat film. When starting up an extrusion line, the process parameters have to be adjusted each time by the operators. For a large line a lot of material has to be processed until the ideal parameter combination has been found. Including a structuring step into this process introduces more variability into the process and might make the setup process even more complicated. This study adds to the understanding of direct extrusion embossing and the influence that different parameters have and might therefore be helpful for the implementation of this technique in an industrial setting.

Answering the third question required a deeper understanding of the underlying mechanism of sandfish inspired surfaces. In order to study the influence of structure geometry and vibration parameters, a customized vibration table and particle tracking system had to be built. Artificial sandfish inspired surfaces were tested with different particle sizes. Some general trends were observed. Higher frequencies and amplitudes lead to faster particle movement and also more thorough cleaning. In general larger particles are cleaned more easily than smaller particles. Interestingly the particle move in a more directional way for frequencies between 200 Hz and 300 Hz. Step height had little influence the speed or thoroughness of the cleaning. While not one single sample performed best under all circumstances it was revealed that samples that most closely resembled the sandfish seem to work well in almost all combinations of frequency and amplitude.

To imprint these sandfish inspired surfaces in polymer film, a mold had to be manufactured first. A stitching process was developed in order to use multiple replicas of a master structure to form a larger mold. This stitching process uses minimal tools available to almost every researcher. The gaps between the individual pieces were between 30 μm and 50 μm in width, while the vertical displacement between the parts is typically below 10 μm, which is remarkable considering the simplicity of the process. After a sandfish inspired mold had been produced, the structures were successfully be imprinted using the direct roll to roll embossing process. This also proves that the R2R embossing process can be used to imprint nano-structures, as the step height of the artificial sandfish surface was just 200 nm.

Finally, this structured polymer film was laminated onto solar panels that were subsequently tested both in a lab setting as well as outdoors using a custom build sensor setup. The lab experiment proved a benefit of using sandfish inspired surfaces on solar panels. After 24 h in an extremely dusty environment the "sandfish" panels delivered about 5 % more power than panels that did not have the sandfish coating. In the field the amount of dust used would correlate to the dust contamination of several weeks. One also has to

consider that, since solar panels work continuously as long as there is sun, even a small gain in overall efficiency provided by the sandfish coatings, will lead to a significant amount of additional energy produced over time. The outdoor, real world experiments unfortunately did not show the same result. This might be due to a multitude of factors, one of which is that the middle European climate in which the experiments were conducted is not comparable to the extremely arid climate of, e.g. the Atacama desert where the sandfish coatings are envisioned to be employed. Further research regarding the benefits of sandfish inspired surfaces in arid climates has to be conducted. As a first step this can be done using the sensor box presented in Chapter 5. Multiple of these inexpensive sensor boxes can be built and sent to partners all over the world in order to collect data from a variety of different climate zones. Other research might focus on the durability of the microstructures when subjected to abrasive sand and dust for multiple decades or combining these structures with, e.g., anti-reflective structures.

Since photovoltaic solar power is the fastest growing renewable energy source with over 400 GW of capacity added every year [4], sandfish inspired coatings have certainly have the potential to become a widespread technology and to make a difference in the fight against climate change.

Bibliography

[1]   Core Writing Team, H. Lee and J. Romero (eds.) 'IPCC, 2023: Climate Change 2023: Synthesis Report. Contribution of Working Groups I, II and III to the Sixth Assessment Report of the Intergovernmental Panel on Climate Change' (2023), pp. 1–34. DOI: 10.59327/IPCC/AR6-9789291691647.001.

[2]   W. F. Lamb et al. 'A review of trends and drivers of greenhouse gas emissions by sector from 1990 to 2018'. *Environmental Research Letters* 16.7 (2021). DOI: 10.1088/1748-9326/abee4e.

[3]   European Environment Agency. *Sectoral greenhouse gas emissions by IPCC sector.* URL: https://www.eea.europa.eu/data-and-maps/daviz/change-of-co2-eq-emissions-2#tab-dashboard-01 (visited on 06/09/2024).

[4]   International Energy Agency. *Renewables 2023.* 2024. URL: https://iea.blob.core.windows.net/assets/96d66a8b-d502-476b-ba94-54ffda84cf72/Renewables_2023.pdf (visited on 06/09/2024).

[5]   F. Mandys, M. Chitnis and S. R. P. Silva. 'Levelized cost estimates of solar photovoltaic electricity in the United Kingdom until 2035'. *Patterns* 4 (2023), p. 100735. DOI: 10.1016/j.patter.2023.100735.

[6]   M. R. Maghami et al. 'Power loss due to soiling on solar panel: A review'. *Renewable and Sustainable Energy Reviews* 59 (2016), pp. 1307–1316. DOI: 10.1016/j.rser.2016.01.044.

[7]   D. Araya-Osses et al. 'Climate change projections of temperature and precipitation in Chile based on statistical downscaling'. *Climate Dynamics* 54.9-10 (2020), pp. 4309–4330. DOI: 10.1007/s00382-020-05231-4.

[8]   S. Valdivielso et al. 'Characterization of precipitation and recharge in the peripheral aquifer of the Salar de Atacama'. *Science of The Total Environment* 806 (2022), p. 150271. DOI: 10.1016/j.scitotenv.2021.150271.

[9]   C. Schill, S. Brachmann and M. Koehl. 'Impact of soiling on IV-curves and efficiency of PV-modules'. *Solar Energy* 112 (2015), pp. 259–262. DOI: 10.1016/j.solener.2014.12.003.

[10] N. Najmi and A. Rachid. 'A Review on Solar Panel Cleaning Systems and Techniques'. *Energies* 16.24 (2023). DOI: 10.3390/en16247960.

[11] A. Alshehri et al. 'Dust mitigation in the desert: Cleaning mechanisms for solar panels in arid regions'. *2014 Saudi Arabia Smart Grid Conference* (2014). DOI: 10.1109/sasg.2014.7274289.

[12] M. Smith et al. 'Effects of Natural and Manual Cleaning on Photovoltaic Output'. *Journal of Solar Energy Engineering* 135 (2013), pp. 034505–034505. DOI: 10.1115/1.4023927.

[13] M. Grando et al. 'Robots for Cleaning Photovoltaic Panels: State of the Art and Future Prospects'. *IX Jornadas Argentinas de Robotica* (2017).

[14] C. Y. Chen et al. 'Dust removal from solar concentrators using an electrodynamic screen'. *Solar Energy* 187 (2019), pp. 341–351. DOI: 10.1016/j.solener.2019.05.044.

[15] A. S. Biris et al. 'Electrodynamic removal of contaminant particles and its applications'. 2 (2004), 1283–1286 vol.2. DOI: 10.1109/IAS.2004.1348578.

[16] W. Nachtigall. *Biological Mechanisms of Attachment.* Springer Berlin, 1974, pp. 68–73. ISBN: 978-3-642-85777-5. DOI: 10.1007/978-3-642-85775-1.

[17] G. Mestral. *Reissverschluss mit flaechenhaft verteilten Kuppelmitteln.* European patent office, Patent Nr.: DE1115201. 1961.

[18] Velcro IP Holdings LLC. *Company history.* URL: https://www.velcro.co.uk/original-thinking/our-story/ (visited on 07/11/2023).

[19] C. T. Foo, B. Omar and I. Taib. 'Shape Optimization of High-Speed Rail by Biomimetic'. *MATEC Web of Conferences* 135 (2017), p. 00019. DOI: 10.1051/matecconf/201713500019.

[20] M. Dorigo and L. M. Gambardella. 'Ant colony system: a cooperative learning approach to the traveling salesman problem'. *IEEE Transactions on Evolutionary Computation* 1 (1997), pp. 53–66. DOI: 10.1109/4235.585892.

[21] Lufthansa Group. *Aeroshark.* 2024. URL: https://www.lufthansa-technik.com/en/aeroshark.

[22] S. Martin and B. Bhushan. 'Modeling and optimization of shark-inspired riblet geometries for low drag applications'. *Journal of Colloid and Interface Science* 474 (2016), pp. 206–215. DOI: 10.1016/j.jcis.2016.04.019.

[23] W. Barthlott and C. Neinhuis. 'Purity of the sacred lotus, or escape from contamination in biological surfaces'. *Planta* 202.1 (1997), pp. 1–8. DOI: 10.1007/s004250050096.

[24] Sto SE und CoKg. *Lotusan Fassadenfarbe.* URL: www.sto.de/s/p/a1F2p00000NwG4JEAV/lotusan (visited on 07/11/2023).

[25] M. Nosonovsky and B. Bhushan. *Multiscale Dissipative Mechanisms and Hierarchical Surfaces.* Springer Berlin Heidelberg, 2008. DOI: 10.1007/978-3-540-78425-8.

[26] M. Montazer and T. Harifi. 'Nanofinishes for self-cleaning textiles'. *Nanofinishing of Textile Materials* (2018), pp. 127–143. DOI: 10.1016/b978-0-08-101214-7.00009-1.

[27] W. Barthlott, M. Mail and C. Neinhuis. 'Superhydrophobic hierarchically structured surfaces in biology: evolution, structural principles and biomimetic applications'. *Philosophical Transactions of the Royal Society A: Mathematical, Physical and Engineering Sciences* 374.2073 (2016), p. 20160191. DOI: 10.1098/rsta.2016.0191.

[28] W. Barthlott et al. 'The Salvinia Paradox: Superhydrophobic Surfaces with Hydrophilic Pins for Air Retention Under Water'. *Advanced Materials* 22 (2010), pp. 2325–2328. DOI: 10.1002/adma.200904411.

[29] C. Zeiger et al. 'Microstructures of superhydrophobic plant leaves - inspiration for efficient oil spill cleanup materials'. *Bioinspiration and Biomimetics* 11.5 (2016), p. 056003. DOI: 10.1088/1748-3190/11/5/056003.

[30] H. F. Bohn and W. Federle. 'Insect aquaplaning: Nepenthes pitcher plants capture prey with the peristome, a fully wettable water-lubricated anisotropic surface'. *Proceedings of the National Academy of Sciences* 101 (2004), pp. 14138–14143. DOI: 10.1073/pnas.0405885101.

[31] P. Wang, D. Zhang and Z. Lu. 'Slippery liquid-infused porous surface bio-inspired by pitcher plant for marine anti-biofouling application'. *Colloids and Surfaces B: Biointerfaces* 136 (2015), pp. 240–247. DOI: 10.1016/j.colsurfb.2015.09.019.

[32] C.G. J. Prakash and R. Prasanth. 'Recent trends in fabrication of nepenthes inspired SLIPs: Design strategies for self-healing efficient anti-icing surfaces'. *Surfaces and Interfaces* 21 (2020), p. 100678. DOI: 10.1016/j.surfin.2020.100678.

[33] J. Li et al. 'Designs and recent progress of "pitcher plant effect" inspired ultra-slippery surfaces: A review'. *Progress in Organic Coatings* 191 (2024), p. 108460. DOI: 10.1016/j.porgcoat.2024.108460.

[34] Q. Xu et al. 'Biomimetic self-cleaning surfaces: synthesis, mechanism and applications'. *Journal of The Royal Society Interface* 13 (2016), p. 20160300. DOI: 10.1098/rsif.2016.0300.

[35] W. Zhao and H. Lu. 'Self-Cleaning Performance of Super-Hydrophilic Coatings for Dust Deposition Reduction on Solar Photovoltaic Cells'. *MDPI AG Coatings* 11 (2021), p. 1059. DOI: 10.3390/coatings11091059.

[36] S. Nishimoto and B. Bhushan. 'Bioinspired self-cleaning surfaces with superhydrophobicity, superoleophobicity, and superhydrophilicity'. *RSC Adv.* 3 (2013), pp. 671–690. DOI: 10.1039/c2ra21260a.

[37] W. Barthlott et al. 'Plant Surfaces: Structures and Functions for Biomimetic Innovations'. *Nano-Micro Letters* 9 (2017). DOI: 10.1007/s40820-016-0125-1.

[38] J. F. Vincent. 'Biomimetics–a review'. *Proceedings of the Institution of Mechanical Engineers. Part H, Journal of engineering in medicine* 223 (2009), pp. 919–39. DOI: 10.1243/09544119JEIM561.

[39] B. Bhushan. 'Biomimetics: lessons from nature–an overview'. *Philosophical Transactions of the Royal Society A: Mathematical, Physical and Engineering Sciences* 367 (2009), pp. 1445–1486. DOI: 10.1098/rsta.2009.0011.

[40] B. Bhushan. 'Biomimetics - Bioinspired Hierarchical-Structured Surfaces for Green Science and Technology'. *Biological and Medical Physics, Biomedical Engineering* (2016). DOI: 10.1007/978-3-319-28284-8.

[41] U. G. K. Wegst et al. 'Bioinspired structural materials'. *Nature Materials* 14 (2014), pp. 23–36. DOI: 10.1038/nmat4089.

[42] O. Spaeker et al. 'Gradients of Orientation, Composition, and Hydration of Proteins for Efficient Light Collection by the Cornea of the Horseshoe Crab'. *Advanced Science* 9 (2022). DOI: 10.1002/advs.202203371.

[43] B. Bhushan. *Springer handbook of nanotechnology.* Springer, 2017, pp. 2–7. ISBN: 978-3-642-02525-9. DOI: 10.1007/978-3-642-02525-9.

[44] E. N. Arnold. 'Identifying the effects of history on adaptation: origins of different sand-diving techniques in lizards'. *Journal of Zoology* 235.3 (1995), pp. 351–388. DOI: 10.1111/j.1469-7998.1995.tb01758.x.

[45] W. Wu et al. 'Snake-Inspired, Nano-Stepped Surface with Tunable Frictional Anisotropy Made from a Shape-Memory Polymer for Unidirectional Transport of Microparticles'. *Advanced Functional Materials* 31.19 (2021), p. 2009611. DOI: 10.1002/adfm.202009611.

[46] W. Wu. 'Tribological characterization of reptile scales and their application as technical surfaces with tunable friction anisotropy'. PhD thesis. Karlsruhe Institute of Technology, 2020.

[47] W. Wu et al. 'Variation of the frictional anisotropy on ventral scales of snakes caused by nanoscale steps'. *Bioinspiration and Biomimetics* 15 (2020). DOI: 10.1088/1748-3190/ab9e51.

[48] J. S. Pettinato and D. Pillai. 'Technology decisions to minimize 450-mm wafer size transition risk'. *IEEE Transactions on Semiconductor Manufacturing* 18.4 (2005), pp. 501–509. DOI: 10.1109/TSM.2005.858471.

[49] S. S. Deshmukh and A. Goswami. 'Current innovations in roller embossing—a comprehensive review'. *Microsystem Technologies* 28 (2022), pp. 1077–1114. DOI: 10.1007/s00542-022-05265-0.

[50] H. Hua, A. Gilbertson and S. Y. Chou. 'Roller imprint lithography'. *Journal of Vacuum Science and Technology B: Microelectronics and Nanometer Structures Processing, Measurement, and Phenomena* (1998), p. 3926. DOI: 10.1116/1.590438.

[51] L. Peng et al. 'Micro hot embossing of thermoplastic polymers: a review'. *Journal of Micromechanics and Microengineering* 24.1 (2013), p. 013001. DOI: 10.1088/0960-1317/24/1/013001.

[52] S. S. Deshmukh and A. Goswami. 'Hot Embossing of polymers – A review'. *Materials Today: Proceedings* 26 (2020), pp. 405–414. DOI: https://doi.org/10.1016/j.matpr.2019.12.067.

[53] Y. Li et al. 'Scaling Up Nature: Large Area Flexible Biomimetic Surfaces'. *ACS Applied Materials; Interfaces* 7 (2015), pp. 23439–23444. DOI: 10.1021/acsami.5b04957.

[54] C. Huawei et al. 'Large-Scale Fabrication of Biomimetic Drag-Reduction Surface via Bio-Replication of Shark Skin'. *Bio-Inspired Surfaces and Applications* Not available (2016), pp. 229–269. DOI: 10.1142/9789814704496_0007.

[55] Fusion Bionic GmbH. *Fusion Bionic website*. URL: https://fusionbionic.com/dlip-technologie/ (visited on 06/09/2024).

[56] A. Lasagni et al. 'Biomimetic Surface Structuring Using Laser Based Interferometric Methods'. *Applied Sciences* 8 (2018), p. 1260. DOI: 10.3390/app8081260.

[57] A. I. Aguilar-Morales et al. 'Influence of processing parameters on surface texture homogeneity using Direct Laser Interference Patterning'. *Optics and Laser Technology* 107 (2018), pp. 216–227. DOI: 10.1016/j.optlastec.2018.05.044.

[58] B. E. Droguet et al. 'Large-scale fabrication of structurally coloured cellulose nanocrystal films and effect pigments'. *Nature Materials* 21 (2021), pp. 352–358. DOI: 10.1038/s41563-021-01135-8.

[59] Y. C. Lee, P. C. Chen and H. Y. Lin. 'Fabrication of seamless roller mold with excimer laser direct writing technology'. *4th IEEE International Conference on Nano/Micro Engineered and Molecular Systems* (2009). DOI: 10.1109/nems.2009.5068691.

[60] M. Röhrig et al. 'Hot pulling and embossing of hierarchical nano- and microstructures'. *Journal of Micromechanics and Microengineering* 23 (2013), p. 105014. DOI: 10.1088/0960-1317/23/10/105014.

[61] W. D. Callister and D. G. Rethwisch. *Callister's Materials Science and Engineering*. John Wiley and Sons, 2020. ISBN: 978-1-119-45391-8.

[62] A. L. Andrady and M. A. Neal. 'Applications and societal benefits of plastics'. *Philosophical Transactions of the Royal Society B: Biological Sciences* 364 (2009), pp. 1977–1984. DOI: 10.1098/rstb.2008.0304.

[63] D.W. Van Krevelen and K. Te Nijenhuis. 'Typology of Polymers'. *Properties of Polymers* (2009), pp. 7–47. DOI: 10.1016/b978-0-08-054819-7.00002-9.

[64] C. S. Brazel and S. L. Rosen. *Fundamental Principles of Polymeric Materials*. John Wiley and Sons Inc., 2012, pp. 1–44. ISBN: 9780470505427.

[65] T. G. Heggs. 'Polypropylene'. *Ullmann's Encyclopedia of Industrial Chemistry* (2011). DOI: 10.1002/14356007.o21_o04.

[66] M. Worgull. *Hot Embossing - Theory and Technology of Microreplication*. Elsevier, 2009. ISBN: 978-0-8155-1579-1. DOI: 10.1016/b978-0-8155-1579-1.50014-8.

[67] J. M. Hutchinson. 'Determination of the glass transition temperature: Methods correlation and structural heterogeneity'. *Journal of Thermal Analysis and Calorimetry* 98 (2009), pp. 579–589. DOI: 10.1007/s10973-009-0268-0.

[68] U. W. Gedde and M. S. Hedenqvist. *Fundamental Polymer Science.* Springer, 2019, pp. 1–35. ISBN: 978-3-030-29792-3. DOI: 10.1007/978-3-030-29794-7_1.

[69] Polyplastics TOPAS Advanced Polymers. *Topas Product Website.* URL: https://topas.com/products/topas-coc-polymers/ (visited on 26/01/2024).

[70] J. Y. Shin et al. 'Chemical structure and physical properties of cyclic olefin copolymers (IUPAC Technical Report)'. *Pure and Applied Chemistry* 77 (2005), pp. 801–814. DOI: 10.1351/pac200577050801.

[71] K. Albrecht, M. Stickler and T. Rhein. 'Polymethacrylates'. *Ullmann's Encyclopedia of Industrial Chemistry* (2013). DOI: 10.1002/14356007.a21_473.pub2.

[72] Roehm GmbH. *Plexiglas Product Website.* URL: https://www.plexiglas.de/en/service/product-info/what-is-plexiglas (visited on 26/01/2024).

[73] A. B. Khoshaim et al. 'Experimental investigation on laser cutting of PMMA sheets: Effects of process factors on kerf characteristics'. *Journal of Materials Research and Technology* 11 (2021), pp. 235–246. DOI: https://doi.org/10.1016/j.jmrt.2021.01.012.

[74] M. N'Diaye et al. 'Water Absorption of Polymethyl methacrylate Measured by Vertical Interference Microscopy'. *Langmuir : the ACS journal of surfaces and colloids* 28 (2012), pp. 11609–14. DOI: 10.1021/la302260a.

[75] D. Tripathi. *Practical Guide to Polypropylene.* Rapra Technology Limited, 2002. ISBN: 9781859573457.

[76] A. Kolew. 'Heißprägen von Verbundfolien für mikrofluidische Anwendungen'. PhD thesis. Karlsruhe Institute of Technology, 2012.

[77] J. A. Rogers and R. G. Nuzzo. 'Recent progress in soft lithography'. *Materials Today* 8 (2005), pp. 50–56. DOI: 10.1016/s1369-7021(05)00702-9.

[78] Wacker Chemie AG. *Solid and Liquid Silicone Rubber Material and Processing Guidelines.* URL: https://www.wacker.com/h/medias/6709-EN.pdf (visited on 27/01/2024).

[79] V. Chandrasekhar. *Inorganic and Organometallic Polymers, Polysiloxanes.* Springer, 2005, pp. 209–248. ISBN: 978-3-540-22574-4. DOI: 10.1007/3-540-26215-6_6.

[80] H. Becker and U. Heim. 'Hot embossing as a method for the fabrication of polymer high aspect ratio structures'. *Sensors and Actuators A: Physical* 83.1 (2000), pp. 130–135. DOI: https://doi.org/10.1016/S0924-4247(00)00296-X.

[81] T.-Y. Lin et al. '3D printed metal molds for hot embossing plastic microfluidic devices'. *Lab on a Chip* 17 (2017), pp. 241–247. DOI: 10.1039/c6lc01430e.

[82] Chris Rauwendaal. *Understanding Extrusion - Extrusion Machinery.* Ed. by Chris Rauwendaal. Hanser, 2019, pp. 1–18. ISBN: 978-1-56990-698-9. DOI: https://doi.org/10.3139/9781569906996.001.

[83] C. I. Chung. *Extrusion of Polymers - Theory and Practice.* Hanser, 2019. ISBN: 9781569906095.

[84] C. Rauwendaal. 'The ABC's of extruder screw design'. *Advances in Polymer Technology* 9 (1989), pp. 301–308. DOI: 10.1002/adv.1989.060090404.

[85] Chris Rauwendaal. *Understanding Extrusion - How an Extruder Works.* Ed. by Chris Rauwendaal. Hanser, 2019, pp. 77–121. ISBN: 9781569906989. DOI: https://doi.org/10.3139/9781569906996.005.

[86] S. Shiromoto. 'The Mechanism of Neck-in Phenomenon in Film Casting Process'. *International Polymer Processing* 29 (2014), pp. 197–206. DOI: 10.3139/217.2784.

[87] D. Dziadowiec et al. 'Overview of the Cast Polyolefin Film Extrusion Technology for Multi-Layer Packaging Applications'. *Materials* 16 (2023), p. 1071. DOI: 10.3390/ma16031071.

[88] LyondellBasell. *A Guide to Polyolefin Film Extrusion.* URL: https://www.lyondellbasell.com/globalassets/documents/polymers-technical-literature/A_Guide_to_Polyolefin_Film_Extrusion.pdf (visited on 28/01/2024).

[89] *Fundamentals of Electrochemical Deposition - Overview.* John Wiley and Sons, Ltd, 2006, pp. 1–6. ISBN: 9780470009406. DOI: https://doi.org/10.1002/0470009403.ch1.

[90] N. Kanani. *Galvanotechnik: Grundlagen, Verfahren und Praxis einer Schlüsseltechnologie.* Carl Hanser, 2020. ISBN: 978-3-446-46256-4.

[91] M. Wissmann et al. 'Alternative mould insert fabrication technology for micromoulding by galvanic replication'. *2010 Symposium on Design Test Integration and Packaging of MEMS/MOEMS* (2010), pp. 278–283.

[92] B. Voigtlaender. 'Atomic Force Microscopy'. Springer International Publishing, 2019, pp. 1–13. ISBN: 978-3-030-13654-3. DOI: 10.1007/978-3-030-13654-3_1.

[93] E. Mayer, H. J. Hug and R. Bennewitz. *Scanning Probe Microscopy - Force Microscopy.* Springer-Verlag Berlin Heidelberg, 2004, pp. 45–91. ISBN: 9783642077371. DOI: 10.1007/978-3-662-09801-1_3.

[94] Y. Wang and J. Wang. 'Friction Determination by Atomic Force Microscopy in Field of Biochemical Science'. *Micromachines* 9 (2018), p. 313. DOI: 10.3390/mi9070313.

[95] G. J. Simpson, D. L. Sedin and K. L. Rowlen. 'Surface Roughness by Contact versus Tapping Mode Atomic Force Microscopy'. *Langmuir* 15.4 (1999), pp. 1429–1434. DOI: 10.1021/la981024a.

[96] Mahr GmbH. *Optical metrology for surface analysis.* URL: https://3915918.fs1.hubspotusercontent-na1.net/hubfs/3915918/GER_%20LP%20diverse.pdf (visited on 24/12/2023).

[97]   S. Inoue and J. B. Pawley. *Handbook Of Biological Confocal Microscopy - Foundations of Confocal Scanned Imaging in Light Microscopy.* Springer US, 2006, pp. 1–19. ISBN: 9780387455242. DOI: 10.1007/978-0-387-45524-2_1.

[98]   F. Lawrence et al. *Confocal microscope.* United States Patent and Trademark Office, Patent Nr.: US5162941A. 1991.

[99]   J. Xiang, T. Zhen and L. Duo. *On-Machine Measurement System and Its Application in Ultra-Precision Manufacturing.* 2019, pp. 1–36. ISBN: 978-981-10-5192-0. DOI: 10.1007/978-981-10-5192-0_16-1.

[100] S. Legutko, G. Krolczyk and J. Krolczyk. 'Quality Evaluation of Surface Layer in Highly Accurate Manufacturing'. *Manufacturing Technology* 14 (2014), pp. 50–56. DOI: 10.21062/ujep/x.2014/a/1213-2489/mt/14/1/50.

[101] P. de Groot. *Optical Measurement of Surface Topography.* Springer Berlin, Heidelberg, 2011, pp. 167–208. DOI: https://doi.org/10.1007/978-3-642-12012-1.

[102] K. Y. Law. 'Definitions for Hydrophilicity, Hydrophobicity, and Superhydrophobicity: Getting the Basics Right'. *The Journal of Physical Chemistry Letters* 5 (2014), pp. 686–688. DOI: 10.1021/jz402762h.

[103] R. N. Wenzel. 'Resistance of solid surfaces to wetting by water'. *Industrial and Engineering Chemistry* 28.8 (1936), pp. 988–994. DOI: 10.1021/ie50320a024.

[104] A. W. Neumann, R. David and Y. Zuo. *Applied Surface Thermodynamics.* CRC Press, 2017. ISBN: 9781138116375.

[105] M. Vuckovac et al. 'Uncertainties in contact angle goniometry'. *Soft Matter* 15.35 (2019), pp. 7089–7096. DOI: 10.1039/c9sm01221d.

[106] M. N. Kavalenka et al. 'Adaptable bioinspired special wetting surface for multifunctional oil/water separation'. *Scientific Reports* 7.1 (2017). DOI: 10.1038/srep39970.

[107] Weiser P. 'M.Sc. thesis: Entwicklung eines kontinuierlichen Verfahrens zur Herstellung von superhydrophobem Nanopelz'. Karlsruhe Institute of Technologiy, 2020.

[108] M. Röhrig et al. 'Nanofur for Biomimetic Applications'. *Advanced Materials Interfaces* 1.4 (2014), p. 1300083. DOI: 10.1002/admi.201300083.

[109] A. Storz. 'M.Sc. thesis: Fabrication, Characterization and Application of Biomimetic Nanofur made of Polymers'. Karlsruhe Institute of Technology, 2016.

[110] C. Zeiger. 'Biomimetics for Efficient Oil Water Separation: From Natural Oil Sorbents to Bioinspired Micro- and Nanostructured Polymeric Sorbents and Membranes'. PhD thesis. Karlsruhe Institute of Technology, 2018.

[111] P. Weiser et al. 'Roll-to-roll fabrication of superhydrophobic pads covered with nanofur for the efficient clean-up of oil spills'. *Beilstein Journal of Nanotechnology* 13 (2022), pp. 1228–1239. DOI: 10.3762/bjnano.13.102.

[112] T. Velten et al. 'Roll-to-roll hot embossing of microstructures'. *Microsystem Technologies* 17.4 (2010), pp. 619–627. DOI: 10.1007/s00542-010-1158-x.

[113] Truworth-Homes. *NeverWet Superhydrophobic Coatings – It Does Exactly What Its Name Implies.* URL: https://truworthhomes.com/collections/super-hydrophobic-coatings-spray-buy (visited on 14/03/2022).

[114] M. Heinisch and D. Miricescu. 'Innovative Industrial Technologies for Preventive Anti-Graffiti Coating'. *MATEC Web of Conferences* 121 (2017), p. 03009. DOI: 10.1051/matecconf/201712103009.

[115] M. Montazer and T. Harifi. 'Nanofinishes for self-cleaning textiles'. *Nanofinishing of Textile Materials.* Elsevier, 2018, pp. 127–143. DOI: 10.1016/b978-0-08-101214-7.00009-1.

[116] Y. Y. Yan, N. Gao and W. Barthlott. 'Mimicking natural superhydrophobic surfaces and grasping the wetting process: A review on recent progress in preparing superhydrophobic surfaces'. *Advances in Colloid and Interface Science* 169.2 (2011), pp. 80–105. DOI: 10.1016/j.cis.2011.08.005.

[117] J. Feng, M. T. Tuominen and J. P. Rothstein. 'Hierarchical Superhydrophobic Surfaces Fabricated by Dual-Scale Electron-Beam-Lithography with Well-Ordered Secondary Nanostructures'. *Advanced Functional Materials* 21.19 (2011), pp. 3715–3722. DOI: 10.1002/adfm.201100665.

[118] H. E. Jeong et al. 'Wettability of nanoengineered dual-roughness surfaces fabricated by UV-assisted capillary force lithography'. *Journal of Colloid and Interface Science* 339.1 (2009), pp. 202–207. DOI: 10.1016/j.jcis.2009.07.020.

[119] M. Gharghi and S. Sivoththaman. 'Formation of nanoscale columnar structures in silicon by a maskless reactive ion etching process'. *Journal of Vacuum Science* 24.3 (2006), pp. 723–727. DOI: 10.1116/1.2167974.

[120] T. H. Her et al. 'Microstructuring of silicon with femtosecond laser pulses'. *Applied Physics Letters* 73.12 (1998), pp. 1673–1675. DOI: 10.1063/1.122241.

[121] X. Liu et al. 'Black silicon: fabrication methods, properties and solar energy applications'. *Energy Environ. Sci.* 7.10 (2014), pp. 3223–3263. DOI: 10.1039/c4ee01152j.

[122] J. E. Carey et al. 'Fabrication of micrometer-sized conical field emitters using femtosecond laser-assisted etching of silicon'. *2001. Proceedings of the 14th International Vacuum Microelectronics Conference.* IEEE, 2001. DOI: 10.1109/ivmc.2001.939660.

[123] H. M. Shang et al. 'Optically transparent superhydrophobic silica-based films'. *Thin Solid Films* 472.1-2 (2005), pp. 37–43. DOI: 10.1016/j.tsf.2004.06.087.

[124] T. Young. 'An essay on the cohesion of fluids'. *Philosophical Transactions of the Royal Society of London* 95 (1805), pp. 65–87. DOI: 10.1098/rstl.1805.0005.

[125] A. B. D. Cassie and S. Baxter. 'Wettability of porous surfaces'. *Transactions of the Faraday Society* 40 (1944), p. 546. DOI: 10.1039/tf9444000546.

[126] C. W. Extrand. 'Criteria for Ultralyophobic Surfaces'. *Langmuir* 20.12 (2004), pp. 5013–5018. DOI: 10.1021/la036481s.

[127] F. Vüllers et al. 'Bioinspired Superhydrophobic Highly Transmissive Films for Optical Applications'. *Small* 12.44 (2016), pp. 6144–6152. DOI: 10.1002/smll.201601443.

[128] S. H. Ahn and L. J. Guo. 'Large-Area Roll-to-Roll and Roll-to-Plate Nanoimprint Lithography: A Step toward High-Throughput Application of Continuous Nanoimprinting'. *ACS Nano* 3.8 (2009), pp. 2304–2310. DOI: 10.1021/nn9003633.

[129] A. Striegel et al. 'Seamless tool fabrication for Roll-to-Roll microreplication'. *Microelectronic Engineering* 194 (2018), pp. 8–14. DOI: 10.1016/j.mee.2018.02.022.

[130] H. Liang et al. 'Roll-to-roll fabrication of touch-responsive cellulose photonic laminates'. *Nature Communications* 9.1 (2018). DOI: 10.1038/s41467-018-07048-6.

[131] D. Rymuszka et al. 'Wettability and thermal analysis of hydrophobic poly(methyl methacrylate)/silica nanocomposites'. *Adsorption Science and Technology* 35.5-6 (2017), pp. 560–571. DOI: 10.1177/0263617417701922.

[132] P. S. Brown and B. Bhushan. 'Durable superoleophobic polypropylene surfaces'. *Philosophical Transactions of the Royal Society A: Mathematical, Physical and Engineering Sciences* 374.2073 (2016), p. 20160193. DOI: 10.1098/rsta.2016.0193.

[133] C. A. Fuentes et al. 'Predicting the adhesion strength of thermoplastic/glass interfaces from wetting measurements'. *Colloids and Surfaces A: Physicochemical and Engineering Aspects* 558 (2018), pp. 280–290. DOI: 10.1016/j.colsurfa.2018.08.052.

[134] B. Bhushan and M. Nosonovsky. *Encyclopedia of Nanotechnology*. Springer Netherlands, 2012. Chap. Rose Petal Effect, pp. 2265–2272. ISBN: 978-90-481-9751-4. DOI: 10.1007/978-90-481-9751-4_157.

[135] The Federal Interagency Solutions Group. *Oil budget Calculator*. 2010. URL: www.restorethegulf.gov/sites/default/files/documents/pdf/OilBudgetCalc_Full_HQ-Print_111110.pdf (visited on 01/07/2021).

[136] J. Idris et al. 'Oil Spills and Sustainable Cleanup Approach'. *Australian Journal of Basic and Applied Sciences* 7 (2014), pp. 272–280.

[137] Z. Xue et al. 'Special wettable materials for oil/water separation'. *J. Mater. Chem. A* 2.8 (2014), pp. 2445–2460. DOI: 10.1039/c3ta13397d.

[138] Deurex. *Deurex Pure website*. URL: https://shop.deurexpure.com/en/properties (visited on 29/07/2023).

[139] Castrol. *Castrol website*. URL: https://www.castrol.com/de_de/germany/home/car-engine-oil-and-fluids/engine-oils/engine-oil-viscosity-grades.html (visited on 01/08/2023).

[140] H. Becker and C. Gärtner. 'Polymer microfabrication methods for microfluidic analytical applications'. *Electrophoresis* 21.1 (2000), pp. 12–26.

[141] A. Uneputty et al. 'Strategies applied to modify structured and smooth surfaces: A step closer to reduce bacterial adhesion and biofilm formation'. *Colloid and Interface Science Communications* 46 (2022), p. 100560. DOI: 10.1016/j.colcom.2021.100560.

[142] R. Ahuja, T. Ahuja and D. Kumar. 'Recent progress in the development of nano-structured conducting polymers/nanocomposites for sensor applications'. *Sensors and Actuators B: Chemical* 136.1 (2009), pp. 275–286. DOI: https://doi.org/10.1016/j.snb.2008.09.014.

[143] B. Bläsi, A. Gombert and M. Niggemann. 'Microstructured Polymer Surfaces with Complex Optical Functions for Solar Applications'. *The Handbook of Environmental Chemistry - Polymers - Opportunities and Risks* (2010). DOI: 10.1007/698_2009_14.

[144] K. Maghsoudi et al. 'Micro-nanostructured polymer surfaces using injection molding: A review'. *Materials Today Communications* 13 (2017), pp. 126–143. DOI: 10.1016/j.mtcomm.2017.09.013.

[145] M. Heckele, W. Bacher and K. Müller. 'Hot embossing - The molding technique for plastic microstructures.' *Microsystem Technologies* 4 (1998), pp. 122–124. DOI: 10.1007/s005420050112.

[146] N. S. Ong, Y. H. Koh and Y. Q. Fu. 'Microlens array produced using hot embossing process'. *Microelectronic Engineering* 60.3 (2002), pp. 365–379. DOI: https://doi.org/10.1016/S0167-9317(01)00695-5.

[147] Y. Ma et al. 'Fabrication System for Large-Area Seamless Nanopatterned Cylinder Mold Using the Spiral Laser Interference Exposure Method'. *Int. J. of Precis. Eng. and Manuf.-Green Tech.* (2022). DOI: https://doi.org/10.1007/s40684-022-00423-1.

[148] K. Janggil, T. Nobuyuki and K. Beomjoon. 'Optical-Softlithographic technology for patterning on a curved surface'. *Journal of Micromechanics and Microengineering* 19 (2009), p. 055017. DOI: 10.1088/0960-1317/19/5/055017.

[149] Fraunhofer Institute for Applied Optics and Precision Engineering IOF. *Laserbeam lithography on plane and curved surfaces.* URL: https://www.iof.fraunhofer.de/en/competences/micro-and-nano-structuring/laser-beam-lithography/laser-beam-lithography-plane-curved-surfaces.html (visited on 27/01/2023).

[150] L. Wenjun et al. 'Surface texturing on stainless steel by direct laser interference lithography'. *2017 IEEE International Conference on Manipulation, Manufacturing and Measurement on the Nanoscale (3M-NANO)*. 2017, pp. 119–123. DOI: 10.1109/3M-NANO.2017.8286335.

[151] W. Bacher, W. Menz and J. Mohr. 'The LIGA technique and its potential for microsystems-a survey'. *IEEE Transactions on Industrial Electronics* 42 (1995), pp. 431–441. DOI: 10.1109/41.464604.

[152] M. Rossrucker. 'M.Sc. thesis: Entwicklung einer Fixierung von mikrostrukturierten Nickel-Shims auf gekrümmten Oberflächen'. Karlsruhe Institute of Technology, 2022.

[153] 3D AG. *3D AG High Accuracy Laser Cutting and Welding.* URL: https://3dag.ch/micro-and-nanotechnology/welding-and-cutting (visited on 27/01/2023).

[154] 3D AG. *Step and repeat process HUGO*. URL: https://3dag.ch/micro-nanotechnology/technologies/uv-imprinting/ (visited on 20/10/2023).

[155] EVG systmes. *UV Nanoimprint Lithography System*. URL: https://www.evgroup.com/products/nanoimprint-lithography/uv-nil-smartnil (visited on 30/10/2023).

[156] R. Bandorf et al. 'Haftfeste Direktmetallisierung von Kunststoffen durch Beschichtung mit Ionen'. *Vakuum in Forschung und Praxis* 27 (2015), pp. 18–23. DOI: 10.1002/vipr.201500587.

[157] R. Bandorf. *Direct metallization of plastics by means of HIPIMS*. URL: https://www.ist.fraunhofer.de/en/technologies/pvd/hipims/direct-metallization-hipims.html (visited on 15/01/2024).

[158] R. N. Kacker, E. S. Lagergren and J. J. Filliben. 'Taguchis orthogonal arrays are classical designs of experiments'. *Journal of Research of the National Institute of Standards and Technology* 96.5 (1991), p. 577. DOI: 10.6028/jres.096.034.

[159] University of York Department of Mathematics. *Orthogonal Arrays (Taguchi Designs)*. 2004. URL: https://www.york.ac.uk/depts/maths/tables/orthogonal.htm (visited on 14/10/2023).

[160] T. Schindelhauer. 'B.Sc. thesis: Prozessoptimerung eines Rolle-zu-Rolle Prozesses zur Nano- und Mikrostrukturierung von Polymerfolie'. Karlsruhe Institute of Technology, 2023.

[161] E. A. Coleman. 'Applied Plastics Engineering Handbook'. William Andrew Publishing, 2011. Chap. 23 - Plastic Additives, pp. 419–428. ISBN: 978-1-4377-3514-7. DOI: 10.1016/B978-1-4377-3514-7.10023-6.

[162] H. Thienpont et al. 'The NEMO educational kit'. *Tenth International Topical Meeting on Education and Training in Optics and Photonics* (2015), 96651S. DOI: 10.1117/12.2207476.

[163] I. Rechenberg et al. *Tribologie im DünensandSandfisch, Sandboa und Sandschleiche als Vorbild für die Reibungs-und Verschleißminderung*. 2009. URL: https://docplayer.org/14947105-Tribologie-im-duenensand.html (visited on 25/09/2023).

[164] W. Baumgartner et al. 'Investigating the Locomotion of the Sandfish in Desert Sand Using NMR-Imaging'. *Public Library of Science* 3.10 (2008), e3309. DOI: 10.1371/journal.pone.0003309.

[165] R. D. Maladen et al. 'Undulatory Swimming in Sand: Subsurface Locomotion of the Sandfish Lizard'. *Science* 325.5938 (2009), pp. 314–318. DOI: 10.1126/science.1172490.

[166] Yang Ding et al. 'Mechanics of Undulatory Swimming in a Frictional Fluid'. *PLoS Computational Biology* 8 (2012), e1002810. DOI: 10.1371/journal.pcbi.1002810.

[167] R. Maladen et al. 'Biophysically inspired development of a sand-swimming robot'. *Robotics: Science and Systems VI* (2010). DOI: 10.15607/rss.2010.vi.001.

[168] B. Vihar, F. G. Hanisch and W. Baumgartner. 'Neutral glycans from sandfish skin can reduce friction of polymers'. *Journal of The Royal Society Interface* 13.116 (2016), p. 20160103. DOI: 10.1098/rsif.2016.0103.

[169] K. Staudt, W. Böhme and W. Baumgartner. 'Comparative Investigations of the Sandfishs beta-Keratin. Part 2: Glycan-Based Friction Reduction'. *Journal of Biomimetics, Biomaterials and Tissue Engineering* 16 (2012), pp. 1–9. DOI: 10.4028/www.scientific.net/jbbte.16.1.

[170] W. Baumgartner et al. 'The sandfish's skin: Morphology, chemistry and reconstruction'. *Journal of Bionic Engineering* 4.1 (2007), pp. 1–9. DOI: 10.1016/s1672-6529(07)60006-7.

[171] I. Rechenberg and A. R. El Khyari. 'Reibung und Verschleiß am Sandfisch der Sahara'. *Bericht zum begleitenden Forschungsvorhaben im Rahmen des Festo-Stipendiums für Herrn Abdullah Regabi El Khyari* (2004).

[172] W. Baumgartner. 'Friction-Reducing Sandfish Skin'. *Encyclopedia of Nanotechnology* (2015), pp. 1–7. DOI: 10.1007/978-94-007-6178-0_258-2.

[173] W. Javed et al. 'Photovoltaic performance degradation due to soiling and characterization of the accumulated dust'. *2016 IEEE International Conference on Power and Renewable Energy.* IEEE, 2016. DOI: 10.1109/icpre.2016.7871142.

[174] M. Abu-Naser. 'Solar Panels Cleaning Frequency for Maximum Financial Profit'. *Open Journal of Energy Efficiency* 06.03 (2017), pp. 80–86. DOI: 10.4236/ojee.2017.63006.

[175] M. Ade. 'M.Sc. thesis: Entwicklung eines Vibrationstisch für kleine Massen'. Karlsruhe Institute of Technology, 2022.

[176] A. Rempel. 'B.Sc. thesis: Analyse der Bewegung von Mikropartikeln auf einer nanostrukturierten Oberfläche'. Karlsruhe Institute of Technology, 2022.

[177] C. E. Duchon. 'Lanczos Filtering in One and Two Dimensions'. *Journal of Applied Meteorology* 18.8 (1979), pp. 1016–1022. DOI: 10.1175/1520-0450(1979)018<1016:lfioat>2.0.co;2.

[178] R. Szeliski. *Computer Vision Algorithms and Applications.* Springer London, 2010, pp. 108–116. ISBN: 978-1-84882-935-0. DOI: 10.1007/978-3-030-34372-9.

[179] S. M. Cioab and M. R. Murty. *A First Course in Graph Theory and Combinatorics.* Springer Singapore, 2009. ISBN: 978-981-19-1362-4. DOI: 10.1007/978-981-19-0957-3.

[180] A. Hamm. 'M.Sc. thesis: Analyse und Optimierung der trockenen Selbstreinigung von Oberflächen inspiriert durch den Sandfisch (Scincus scincus)'. Karlsruhe Institute of Technology, 2023.

[181] A. Lasagni, C. Holzapfel and F. Mücklich. 'Periodic Pattern Formation of Intermetallic Phases with Long Range Order by Laser Interference Metallurgy'. *Advanced Engineering Materials* 7 (2005), pp. 487–492. DOI: 10.1002/adem.200400206.

[182] C. Palmer. *Diffraction Grating Handbook*. MKS Instruments, Inc., 2020.

[183] Q. Wang et al. 'Mechanical Ruling of Diffraction Grating: Part II Experimental Investigation and Numerical Simulation'. *Volume 2: Materials Biomanufacturing; Properties, Applications and Systems; Sustainable Manufacturing* (2016). DOI: 10.1115/msec2016-8715.

[184] B. Vihar. 'Mimicking the abrasion resistant sandfish epidermis'. PhD thesis. Technische Hochschule Aachen, 2015.

[185] T. S. Kuan and P. Sung-Yong. 'Dispersive Optical Systems for Highly-Concentrated Solar Spectrum Splitting: Concept, Design, and Performance Analyses'. *Energies* 12.24 (2019), p. 4719. DOI: 10.3390/en12244719.

[186] TRU Components. *TRU Components POLY-PVZ-8080 Datasheet*. URL: https://asset.conrad.com/media10/add/160267/c1/-/en/001569024DS01/datenblatt-1569024-tru-components-poly-pvz-8080-5v-polykristallines-solarmodul-06-w-5-v.pdf (visited on 22/08/2023).

[187] L. F. Nassier and M. H. Shinen. 'Study of the optical properties of poly (methyl methacrylate) (PMMA) by using spin coating method'. *Materials Today: Proceedings* 60 (2022), pp. 1660–1664. DOI: https://doi.org/10.1016/j.matpr.2021.12.213.

[188] Norland Products Incorporated. *Norland Optical Adhesive 68 datasheet*. URL: https://www.norlandprod.com/literature/68tds.pdf (visited on 22/09/2023).

[189] F.A. Mejia and J. Kleissl. 'Soiling Losses for Solar Photovoltaic Systems in California'. *Solar Energy* 95 (2013), pp. 357–363. DOI: 10.1016/j.solener.2013.06.028.

[190] M. Abu-Naser. 'Solar Panels Cleaning Frequency for Maximum Financial Profit'. *Open Journal of Energy Efficiency* 06 (2017), pp. 80–86. DOI: 10.4236/ojee.2017.63006.

Chapter 7

Appendix

7.1 List of Publications

- P. Weiser, R. Kietz, M. Schneider, M. Worgull, H. Hölscher. *Roll-to-roll fabrication of superhydrophobic pads covered with nanofur for the efficient clean-up of oil spills* in Beilstein J. Nanotechnol., 13, 1228–1239 (2022)

7.2 List of Conference Contributions

- Euspen Special Interest Group Meeting: "Structured and Freeform Surfaces" September 28-30, 2022, in Huddersfield, United Kingdom. Patrick Weiser, Marc Schneider, Markus Guttmann, Matthias Worgull, Hendrik Hölscher, *Roll-to-Roll Fabrication of Biomimetic Surfaces*

- Beilstein Nanotechnology Symposium "Functional Micro- and Nanostructured Surfaces: From Biology to Biomimetics", May 9-11, 2023, in Limburg an der Lahn, Germany. Patrick Weiser, Weibin Wu , Marc Schneider, Markus Guttmann, Guillaume Gomard, Matthias Worgull, Amelie Hamm, Hendrik Hölscher, *Dry self-cleaning of photovoltaic panels with nanostructures inspired by the sandfish (Scincus scincus)* (poster)

- Euspen Special Interest Group Meeting: "Micro/Nano Manufacturing", November 28-29, 2023, in Illmenau, Germany. Patrick Weiser, Matthias Worgull, Markus Guttmann, Marc Schneider, Hendrik Hölscher, *Combined extrusion and roller imprinting for large scale structuring of polymer films*

7.3   Tables

Parameter	Setting 1	Setting 2	Setting 3	Setting 4	Setting 5
Melt temp. [°C]	220	230	240	250	245
Screw speed [1/min]	100	125	150	175	200
Roller speed [m/min]	2	3	4	5	6
Roller temp. [°C]	25	35	45	50	40
Pressure [N]	2200	2650	3150	880	1750

Table 7.1: Parameter settings for the fractional factorial experiments of direct roll to roll imprinting.

Experiment Nr.	Melt temp.	Screw speed	Roller speed	Roller temp.	Embossing force
1	1	1	1	1	1
2	1	2	2	2	2
3	1	3	3	3	3
4	1	4	4	4	4
5	1	5	5	5	5
6	2	1	2	3	4
7	2	2	3	4	5
8	2	3	4	5	1
9	2	4	5	1	2
10	2	5	1	2	3
11	3	1	3	5	2
12	3	2	4	1	3
13	3	3	5	2	4
14	3	4	1	3	5
15	3	5	2	4	1
16	4	1	5	4	3
17	4	2	1	5	4
18	4	3	2	1	5
19	4	4	3	2	1
20	4	5	4	3	2
21	5	1	5	4	3
22	5	2	1	5	4
23	5	3	2	1	5
24	5	4	3	2	1
25	5	5	4	3	2

Table 7.2: Orthogonal array used for the fractional factorial experiments of direct roll to roll imprinting taken from [159]